

NATIONAL INSTITUTE FOR FUSION SCIENCE

Recent Progress of Pulsed Power Technology and its  
Application to High Energy Density Plasma

Edited by Hiroaki Ito and Tetsuo Ozaki

( Received - Aug. 31. 2017 )

NIFS-PROC-107

Nov. 27, 2017

This report was prepared as a preprint of work performed as a collaboration research of the National Institute for Fusion Science (NIFS) of Japan. The views presented here are solely those of the authors. This document is intended for information only and may be published in a journal after some rearrangement of its contents in the future.

Inquiries about copyright should be addressed to the NIFS Library, National Institute for Fusion Science, 322-6 Oroshi-cho, Toki-shi, Gifu-ken 509-5292 Japan.

E-mail: [gakujutsujoho@nifs.ac.jp](mailto:gakujutsujoho@nifs.ac.jp)

**<Notice about photocopying>**

In order to photocopy and work from this publication, you or your organization must obtain permission from the following organization which has been delegated for copyright for clearance by the copyright owner of this publication.

Except in the USA

Japan Academic Association for Copyright Clearance (JAACC)  
6-41 Akasaka 9-chome, Minato-ku, Tokyo 107-0052 Japan  
Phone: 81-3-3475-5618 FAX: 81-3-3475-5619 E-mail: [jaacc@mtd.biglobe.ne.jp](mailto:jaacc@mtd.biglobe.ne.jp)

In the USA

Copyright Clearance Center, Inc.  
222 Rosewood Drive, Danvers, MA 01923 USA  
Phone: 1-978-750-8400 FAX: 1-978-646-8600

# Recent Progress of Pulsed Power Technology and its Application to High Energy Density Plasma

Edited by Hiroaki Ito and Tetsuo Ozaki

January 7-8, 2016  
National Institute for Fusion Science  
Toki, Gifu, Japan

## Abstract

The papers presented at the symposium on “Recent Progress of Pulsed Power Technology and its Application to High Energy Density Plasma” held on January 7-8, 2016 at National Institute for Fusion Science are collected. The papers in this proceeding reflect the present status and recent progress in the experimental and theoretical works on high power particle beams and high energy density plasmas produced by pulsed power technology.

Keyword: high power particle beam, high energy density plasma, pulsed power technology, z-pinch, EUV, x-ray, pulsed discharge, high power electromagnetic wave, material processing, medical application

## Preface

The symposium entitled “Recent Progress of Pulsed Power Technology and its Application to High Energy Density Plasma” was organized as a part of the General Collaborative Research of National Institute for Fusion Science (NIFS) and held on January 7-8, 2016 at NIFS, Toki. During the 2 days of symposium, 33 papers were presented. The total number of participants was 61 including students and researchers from universities and a company.

As the field of high energy density plasma has multidisciplinary mature, the extensive discussion of related subjects is difficult in conventional scientific meeting. The purpose of the symposium has been to provide a forum to discuss important technical developments, important applications, increased understandings, new trends and the future in the field of high energy plasmas and pulsed power technologies. Therefore, the papers in this proceeding reflect the present status and progress in the research fields on high power particle beams and high energy density plasmas produced by pulsed power technology in Japan. It is my pleasure if the symposium was beneficial to the development of the pulsed power technology and could provide some kind of opportunity for all participants, especially for young scientists.

We would like to express our sincere thanks to all of the participants, authors and the staff of NIFS.

Hiroaki Ito  
Graduate School of Science and Engineering for Research  
University of Toyama

Tetsuo Ozaki  
National Institute for Fusion Science

## List of Participants

K. Takahashi	Iwate University
T. Okumura	Iwate University
T. Tomite	Iwate University
N. Yugami	Utsunomiya University
Y. Takada	Utsunomiya University
T. Fukuda	Utsunomiya University
K. Takayama	High Energy Accelerator Research Organization
S. Furuya	Saitama Institute of Technology
K. Horioka	Tokyo Institute of Technology
J. Hasegawa	Tokyo Institute of Technology
T. Kawamura	Tokyo Institute of Technology
T. Sonekoda	Tokyo Institute of Technology
K. Nakamura	Tokyo Institute of Technology
H. Matsuo	Tokyo Institute of Technology
H. Wakabayashi	Tokyo Institute of Technology
R. Chiba	Tokyo Institute of Technology
T. Momma	Tokyo Institute of Technology
M. Hirose	Tokyo City University
K. Takasugi	Nihon University
T. Shikone	Nihon University
T. Yoshimizu	Nihon University
G. Imada	Niigata Institute of Technology
S. Higuchi	Niigata Institute of Technology
W. Jiang	Nagaoka University of Technology
T. Kikuchi	Nagaoka University of Technology
T. Sasaki	Nagaoka University of Technology
T. Sugai	Nagaoka University of Technology
R. Hayashi	Nagaoka University of Technology
Md. S. Zaman	Nagaoka University of Technology
A. Inoue	Nagaoka University of Technology
K. Inagawa	Nagaoka University of Technology
T. Hanya	Nagaoka University of Technology
P. T. Nguyen	Nagaoka University of Technology

H. Ito	University of Toyama
H. Ohashi,	University of Toyama
K. Oyama	University of Toyama
K. Okajima	University of Toyama
T. Nakamura	University of Toyama
N. Aoki	University of Toyama
T. Honoki	University of Toyama
T. Mitani	University of Toyama
K. Kamada	Kanazawa University
R. Ando	Kanazawa University
Y. Soga	Kanazawa University
Y. Park	Kanazawa University
M. Takeda	Kanazawa University
R. Kiyomoto	Kanazawa University
D. Takagi	Kanazawa University
S. Nakada	Kanazawa University
T. N. Tan	Kanazawa University
T. Yoshino	Kanazawa University
Y. Komori	Kanazawa University
S. Katsuki	Kumamoto University
S. Lim	Kumamoto University
T. Kajiwara	Kumamoto University
Ryuta Andachi,	Kumamoto University
A. Tokuchi	Pulsed Power Japan laboratory Ltd.
T. Ozaki	National Institute for Fusion Science
T. Tazima	National Institute for Fusion Science
T. Tokuzawa	National Institute for Fusion Science
Y. Narushima	National Institute for Fusion Science

# Contents

1.	Decomposition of Dichloromethane by Discharge inside Bubble in Water Katsuyuki Takahashi, Wataru Hareyama, Koichi Takaki, Naoya Satta (Iwate University) .....	1
2.	Environmental Improvement of Hydroponics Solution Using Discharge Plasma under Water Takamasa Okumura, Kohei Takano, Yoshinori Saito, Katsuyuki Takahashi, Koichi Takaki, Naoya Satta (Iwate University), Takuya Fujio (Iwate Agricultural Research Center) .....	5
3.	Characterization of Atmospheric Pressure Plasma Jet using a Double Coaxial Glass Tube Kohei Oyama, Tetta Mitani, Hayato Ohashi, Hiroaki Ito (University of Toyama) .....	10
4.	DNA fragmentation and Caspase-3 Activation of HeLa Cells Induced by Intense Burst Sinusoidal Electric Fields Ryuta Andachi, Masahiko Yano, Keisuke Abe, Sunao Katsuki (Kumamoto University) .....	16
5.	Enhance the Efficiency of Pulsed Electric Fields Sterilization for Liquid Foods Taiga Kajiwara, Kazuma Baba and Sunao Katsuki (Kumamoto University) .....	26
6.	Dependence of Current Waveform on Laser-Triggered Discharge Plasma for EUV Radiation Soowon Lim, Takashi Kamohara, S. Hamid R. Hosseini, Sunao Katsuki (Kumamoto University) .....	34
7.	Control of Dense Laser-Produced Plasma Flow Using a Magnetic Nozzle Hiroto Wakabayashi, Koya Hiraide, Jun Hasegawa, Toru Kawamura, Kazuhiko Horioka (Tokyo Institute of Technology) .....	39
8.	Generating Chaos by Semiconductor Injection Laser System for Electric Power Demand Prediction Satoshi Higuchi, Satoshi Ebisawa, Go Imada (Niigata Institute of Technology).....	43
9.	Terahertz Radiation from Laser Created Plasma by Applying a Transverse Static Electric Field Takuya Fukuda, Koji Katahira, Noboru Yugami (Utsunomiya University).....	47
10.	Sub-THz electromagnetic wave generation from DARC Yoshihiro Takada, Yusuke Hyuga, Noboru Yugami (Utsunomiya University) .....	50
11.	Fundamental Properties of the Counter-facing Plasma Focus Device for Extreme Ultra-Violet Light Source Tatsuya Sonekoda (Tokyo Institute of Technology, IHI Corporation), Shintaro Kurata, Hajime Kuwabara (IHI Corporation), Kazuhiko Horioka (Tokyo Institute of Technology).....	53
12.	Repetitive X-Ray Source by Triboluminescence Seizo Furuya (Saitama Institute of Technology).....	58

13. Development of Measurement Method for Warm Dense Matter toward Material Selection for Fast Ignition  
 Toru Sasaki, Takumi Ohuchi, Arata Watabe, Satoshi Sugimoto, Yuki Sugimoto, Kazumasa Takahashi, Takashi Kikuchi, Nob. Harada (Nagaoka University of Technology), Mayuko Koga (University of Hyogo), Shinsuke Fujioka (Osaka University)..... 62
14. Investigation of Basic Properties of a Fullerene Ion Source Using Sublimation and Electron Attachment  
 Kohshiro Nakamura, Eisuke Baba, Jun Hasegawa, Toru. Kawamura, Kazuhiko Horioka (Tokyo Institute of Technology) ..... 67
15. Study of Laser Ablation Induced Shock Waves in a Low-Pressure Gas using a Probe-Beam-Deflection Technique  
 Rimpei Chiba, Yuta Ishikawa, Jun Hasegawa, Kazuhiko Horioka (Tokyo Institute of Technology)..... 71
16. Giant Cluster Ion Inertial Fusion Driver and Its Possible R&D using the KEK 12 GeV PS Facility  
 Ken Takayama (High Energy Accelerator Research Organization), Kazuhiko Horioka (Tokyo Institute of Technology) ..... 75
17. Study on Cost Evaluation and Social Cost in Heavy-Ion Inertial Fusion System  
 Akie Inoue, Kazumasa Takahashi, Toru Sasaki, Takashi Kikuchi, Nob. Harada(Nagaoka University of Technology), John J. Barnard (Lawrence Livermore National Laboratory) ..... 84
18. Characterization of High-Energy Ions in the Divergent Gas-Puff Z-Pinch  
 Takashi Shikone, Shun Hakamatsuka, Keiichi Takasugi (Nihon University) ..... 86
19. Numerical Analysis of Electron Behavior in Beam Diode Driven by Intense Pulsed Power Device  
 Md. Shahed-Uz-Zaman, Kazumasa Takahashi, Toru Sasaki, Takashi Kikuchi, Nob. Harada (Nagaoka University of Technology) ..... 90
20. Evaluation of Bipolar Pulse Generator for 2nd stage acceleration in Bipolar Pulse Accelerator  
 Keito Okajima, Tarou Honoki, Hiroaki Ito (University of Toyama) ..... 95

# Decomposition of Dichloromethane by Discharge inside Bubble in Water

Katsuyuki Takahashi\*, Wataru Hareyama, Koichi Takaki, Naoya Satta

*Iwate University*

## ABSTRACT

Decomposition of dichloromethane (DCM) by discharge inside bubble in water is investigated. A gas injected discharge reactor is employed to achieve degradation with high energy efficiency. The reactor consists of a glass tube and a tungsten wire inserted into the glass tube, which is immersed in the water. The nanosecond pulsed high voltage generated by an inductive energy storage system pulsed power generator is applied to the tungsten wire to generate streamer discharge. Argon gas is injected into the glass tube to generate bubbles in the water. The experimental result shows that total organic carbon (TOC) and pH value decrease and chloride ion concentration increases by the discharge treatment. DCM is volatilized into the bubble, which is decomposed by hydroxyl radical produced by the discharge.

## Keywords

Key Words (Water purification, discharge in bubble, dichloromethane, hydroxyl radical)

## 1. Introduction

Dichloromethane (DCM) is widely used as an industrial solvent and is one of hazardous chlorinated volatile organic compounds (VOCs). Owing to its chemical stability, it is difficult to decompose with conventional methods such as chemical oxidation and ozone treatment. A pulsed discharge plasma for treating pollutants in water has attracted a significant amount of attention. The pulsed discharge makes it possible to instantaneously produce a non-thermal plasma in which various chemical species, such as hydroxyl radicals, exist [1]~[3]. In this study, the decomposition of DCM by discharge inside bubble in water is investigated. Argon (Ar) and oxygen (O<sub>2</sub>) gases are injected to identify the dominant reactions of the degradation of organic contaminants. In order to investigate the process of DCM decomposition, the experiments are conducted with mixed solution of DCM and Indigo carmine (IC).

## 2. Experimental Setup

The DCM solution is prepared by adding 1~ 6  $\mu$ L of DCM into 15 mL of purified water in a 30 mL

glass vial (Nichiden-Rika Glass, LTD, SVG-30) with a micro-syringe (SGE Analytical Science, 1  $\mu$ L Syringe). The vial is sealed with a rubber cap coated with the Teflon, and is shaken for 2 hours. The concentration of DCM is ranged from 0.51 mM to 5.8 mM. The mixed solution of DCM and IC is prepared with dissolving IC into the DCM solution. The concentrations of DCM and IC in the mixed solution are adjusted at 0~5 mM and 0~1 mM, respectively.

Figure 1 shows a schematic diagram of the reactor [4]. Two glass tubes, in which the electrode of stainless steel wire (0.2 mm in diameter) or tungsten wire (0.2 mm in diameter) is inserted, are vertically immersed in the solution in the vial used for the preparation of the solutions. The inner diameter of both of the glass tubes is 0.8 mm. The electrode of the stainless steel wire is used as grounded electrode, and immersed the water. The length between the tip of the stainless steel wire and the tip of the glass tube is 20 mm. The electrode of the tungsten wire in the glass tube is placed above the water. The gap length between the tip of tungsten wire and the tip of glass

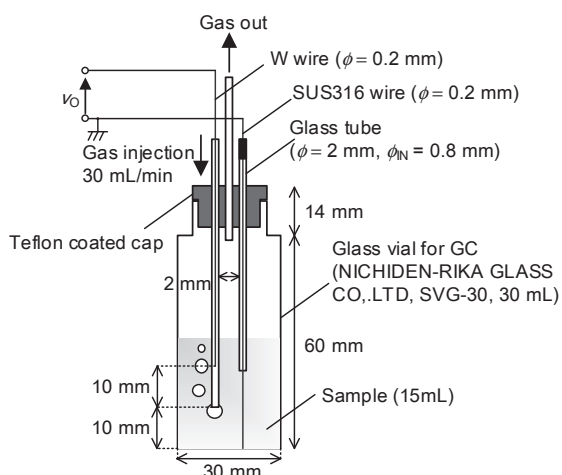


Fig. 1. Schematic diagram of the discharge reactor.

tube is 10 mm. Argon gas is injected into the reactor through the glass tube with the tungsten wire. The gas flow rate is fixed at 30 mL/min. The injected gas is ejected through another glass tube placed in the center of the reactor. The pulsed voltage generated by The inductive energy storage system pulsed power generator [4] is applied to the tungsten wire to generate the streamer discharge in the tube and the bubble. Figure 2 shows the typical waveforms of output voltage and current. The peak value of the output voltage is 16 kV. The pulse repetition rate is fixed at 100 pulses per second.

The concentration of total organic carbon (TOC) of in the DCM solution is measured by a TOC analyzer (Shimadzu, TOC-VCSH), and DCM removal rate is obtained from the following equation:

$$\begin{aligned} \text{Amount of removed DCM} = & \\ & \{ \text{TOC (initial)} - \text{TOC (treated)} \} \\ & \times \frac{\text{MW of DCM (85)}}{\text{MW of Carbon (12)}} \times \frac{15}{1000} [\text{mg}] \quad (1) \end{aligned}$$

The DCM removal rate is obtained by dividing the amount of removed DCM by the initial amount of DCM.

The concentration of chloride ion produced by decomposition of DCM [5] is determined using an ion chromatography (DIONEX, DX-320J). The DCM decomposition rate is obtained from the following equation:

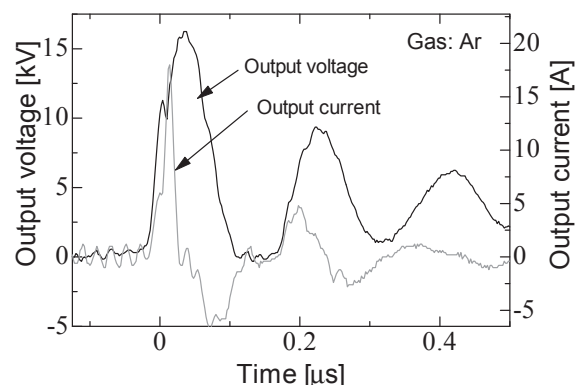


Fig. 2. Typical waveforms of output voltage and current.

Amount of decomposed DCM =

$$\begin{aligned} & \text{Concentration of Cl}^- \\ & \times \frac{\text{MW of DCM (85)}}{\text{MW of Cl}^- (35.5 \times 2)} \times \frac{15}{1000} [\text{mg}] \quad (2) \end{aligned}$$

The DCM decomposition rate is obtained by dividing the amount of decomposed DCM by the initial amount of DCM.

The absorbance of the DCM-IC mixed solutions is measured by a spectrometer (Hitachi high technologies, U-1800) at a wavelength of 610 nm, and the decolorization rate is obtained from the following equation:

$$\begin{aligned} \text{Decolorization rate} = & \\ & \frac{(\text{Absorbance (initial)} - \text{Absorbance (treated)})}{\text{Absorbance (initial)}} \\ & \times 100\% \quad (3) \end{aligned}$$

### 3. Results and Discussion

#### 3.1 Characteristics of DCM decomposition

Figure 3 shows DCM removal efficiency and DCM decomposition efficiency as a function of treatment time in the DCM solution in the case of Ar injection with and without discharges. The initial concentration of DCM is 0.87 mM. The DCM removal efficiency increases without discharges because of volatility of bubbling gas. The DCM removal efficiency and decomposition efficiency with discharges at treatment time of 25 min are 96% and 80%, respectively, which

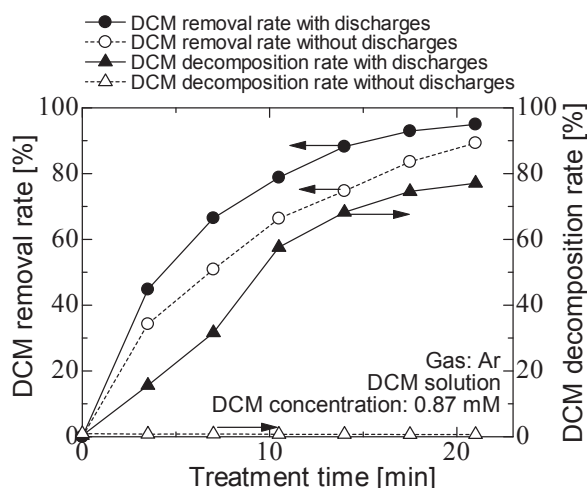


Fig. 3 DCM removal efficiency and decomposition efficiency as a function of treatment time with or without discharges.

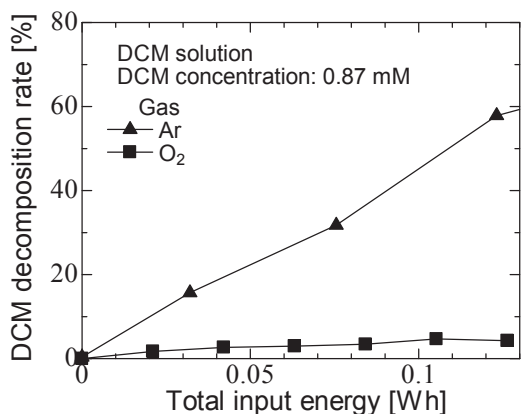


Fig. 4. DCM decomposition efficiency as function of total input energy into the reactor for Ar and O<sub>2</sub> injection.

indicates that approximately 83% of removed DCM is decomposed into hydrogen chloride (HCl) by discharges as following reactions [5]:

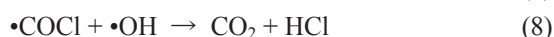


Figure 4 shows the DCM decomposition efficiency as a function of total input energy for Ar and O<sub>2</sub> injection. DCM decomposition efficiency in the case of Ar injection is much higher than that of O<sub>2</sub> injection with same input energy. Energy efficiency for hydroxyl radical production in the case of O<sub>2</sub>

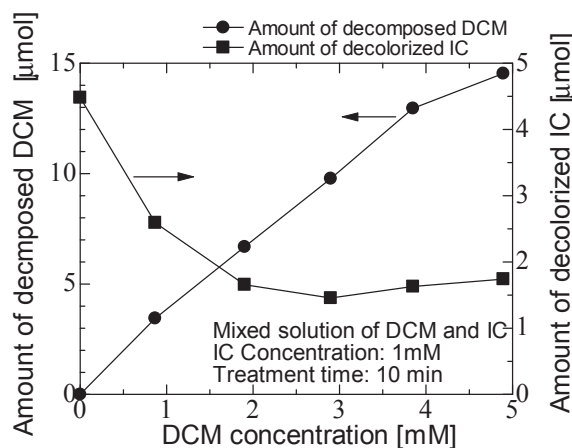


Fig.5 Amounts of decomposed DCM and decolorized IC as a function of IC concentration

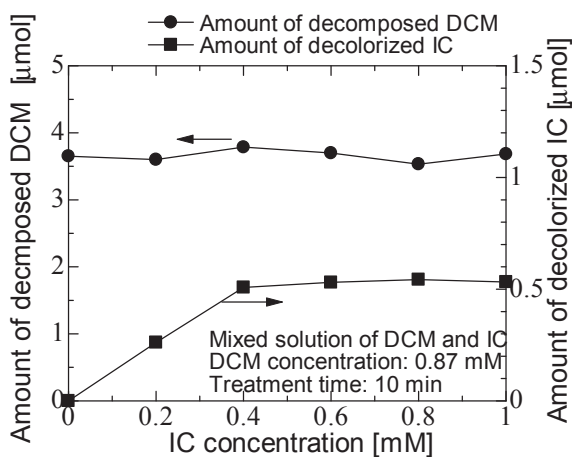


Fig.6. Amounts of decomposed DCM and decolorized IC as a function of DCM concentration

injection is lower than that of Ar injection, because ozone (O<sub>3</sub>) produced by discharges reduces hydroxyl radical (•OH) [6]. These results show chemical species such as •OH produced by discharges mainly contributes to the decomposition of DCM.

### 3.2 Decomposition process of DCM

Figure 5 shows the amounts of DCM decomposed DCM and decolorized IC as a function of DCM concentration in mixed solution of DCM and IC. Ar gas is injected. The initial concentration of IC is 1 mM. The amount of decolorized IC decreases with increasing the DCM concentration. Figure 6 shows the amount of decomposed DCM and decolorized IC as a function of IC concentration. The initial

concentration of DCM is 0.87 mM. The amount of decomposed DCM is almost independent with IC concentration.

Although the reaction rate of •OH with DCM ( $2.2 \times 10^7 \text{ M}^{-1}\text{S}^{-1}$  [7]) is much lower than that with IC ( $1.8 \times 10^{10} \text{ M}^{-1}\text{S}^{-1}$ ) [8]), the amount of decomposed DCM is about 6 times higher than that of decolorized IC when the concentration of DCM equals that of IC as shown in Fig. 5. The contradictory results suggest the DCM decomposition process as follows. The DCM is volatilized into the bubble quickly because of its high volatility when the bubble is generated in the solution by the gas injection. •OH produced by discharges reacts with DCM inside bubble. •OH that not consumed in the reaction with DCM dissolves into the solution, and then reacts with IC in the solution. Since HCl has a high solubility, almost HCl is dissolved into the solution.

#### 4. Conclusions

The decomposition of DCM by the discharge inside bubble is investigated experimentally. The DCM is only removed without discharges because of volatility of bubbling gas. The DCM is decomposed with discharges. DCM is volatilized into the bubble, which is decomposed by hydroxyl radical produced by the discharge.

#### Acknowledgment

The authors are grateful to Associate Professor S. Mukaigawa, Mr. Y. Shida, Dr. T. Okumura and Mr. R. Konno of Iwate University for their valuable comments and technical supports.

#### References

- [1] H. Akiyama, "Streamer Discharge in Liquids and their Applications", *IEEE Trans. Diel. Elect. Insul.*, **7**, 5, pp. 646-653 (2002)
- [2] M. Sato, "Environmental and biotechnological applications of high-voltage pulsed discharges in water", *Plasma Sources Sci. Technol.*, **17**, 024021, pp. 1-7 (2008)
- [3] K. Takahashi et al., "Water Remediation Using Pulsed Power Discharge under Water with an Advanced Oxidation Process", *Journal of Advanced Oxidation Technologies*, **15**, 2, pp. 365-373 (2012)
- [4] S. Kawano, et al., "Influence of pulse width on decolorization efficiency of organic dye by discharge inside bubble in water", *J. Phys.: Conf. Ser.*, 441, 012007 (2013)
- [5] Yonezawa, et al., "Decomposition characteristics of dichloromethane by plasma in water", *J. Inst. Electrostat. Jpn*, **35**, pp. 31-37 (2011)
- [6] Hibert, et al., "OH(X) measurements by resonant absorption spectroscopy in a pulsed dielectric barrier discharge", *J. App. Phys.*, **85**, pp. 7070-7075 (1999)
- [7] W. R. Haag, et al., "Rate constants for reaction of hydroxyl radicals with several drinking water contaminants", *Environ. Sci. Technol.*, **26**, pp. 1005-1013 (1992)
- [8] H. Liao, et al., "Study of indigo carmine as radical probe in photocatalysis", *J. Photoch. Photobio. A*, **202**, pp. 86-91 (2009)

# Environmental Improvement of Hydroponics Solution Using Discharge Plasma under Water

Takamasa Okumura, Kohei Takano, Yoshinori Saito, Katsuyuki Takahashi,  
Koichi Takaki, Naoya Satta, Takuya Fujio\*

*Iwate University*

*\*Iwate Agricultural Research Center*

## ABSTRACT

We developed a system using a discharge plasma under water for inactivating bacteria in hydroponics system, and carried out a pilot test of the developed discharge plasma system in a greenhouse for the period of 5 months using tomato plants in hydroponics system. The plasma reactor consisted of a wire electrode which was placed in an insulating circular cylinder, and a grounded electrode on cylinder outside. The reactor was sunk under the hydroponics solution and atmospheric air was injected into the cylinder using a gas pump. Repetitive nanosecond high-voltage pulses were applied to the wire electrode, using a magnetic pulse compression (MPC) pulsed power generator. Concentration of dissolved ozone into 100 L solution was approximately 0.3 ppm in the early 30 minutes. The developed system worked for 5 months in stable. The all plant bodies healthily grew and produced fruit bodies normally without infection of bacteria. This result suggested that the plants had no damage by the oxidative stress. The performance of the developed system was also evaluated using hydroponics solution contaminated with *Ralstonia solanacearum*, a plant pathogenic bacterium. The number of colony forming unit (CFU) of *R. solanacearum* in the solution was decreased from  $10^7$  to  $10^2$  CFU/mL by operating the discharge plasma system for 100 minutes. The bacterial wilt disease was significantly suppressed by the discharge plasma, in contrast, all seedlings in a positive control wilted and died by infection of *R. solanacearum*.

## Keywords

Discharge plasma under water, Plant, *Ralstonia solanacearum*, inactivation, hydroponics solution, pathogen.

## 1. Introduction

In recent years, soilless system such as hydroponics has been widely used in a field of agriculture [1]. There is two main system in hydroponics: i) recirculation system and ii) run-to-waste system. The former is more acceptable to reduce environmental load such as contamination of lakes and marshes, that results in contamination of well and ground water. Advantages of recirculation system are a higher production, energy conservation, better control of growth, and independence of soil quality [2].

In general, the strategy in hydroponics has been to

keep the cultivating systems as clean as possible. Due to the use of clean substrates, soil-borne pathogens such as *Fusarium oxysporum*, *Verticillium dahliae*, nematodes and many others that can survive in the deeper soil-layers, can be circumvented. However, during the entire period of plant growth, contamination with pathogens can never be excluded, since they can be brought in via the water supply, by air, insects, or inadvertently, by the grower directly. Zoospores actively swim to their hosts so that infection can occur within minutes. Multiplication of these pathogens is explosive under a favorable conditions. Once even one plant is infected, the entire

cultivation bed is subjected to significant risks. An overview was given on the *Fusarium* and *Pythium* species that spread through the cultivating system by recirculation of the irrigation water [3].

In conventional, hydroponic solution is usually treated with technologies using heat, ultraviolet, ozone (O<sub>3</sub>), and/or membrane filtration. However, these treatments are limited in practice owing to their high running cost including periodical cleaning. Thus a discharge plasma under water has attracted attention and is a promising technique to reduce infection risks [4,5]. The discharge plasma produces chemically active species such as atomic oxygen, ozone and hydroxyl radicals. These chemical species play an important role in inactivating various pathogenic bacteria in hydroponics solution [6-10]. A discharge plasma reactor has been developed for a use of laboratory-scale hydroponics system [11,12]. In this report, the reactor is extended for a large scale hydroponics system. And then, a pilot test of the reactor was carried out in a hydroponics system in a greenhouse. Moreover, the performance of the reactor was evaluated using a heavily contaminated hydroponics solution with a plant pathogenic bacterium.

## 2. Experimental

In order to extend the area where a discharge plasma occurs, a discharge plasma reactor [11,12] was developed as shown in Figure 1. The reactor consisted of a wire electrode which was placed in an insulating circular cylinder, and a grounded electrode on cylinder outside. The distance between wire electrode and water-air surface was around 10 mm. Holes of the cylinder were 0.5 mm in a diameter and 2.0 mm separation one another. Repetitive nanosecond pulses are applied to the wire electrode, using a magnetic pulse compression (MPC) pulsed power generator. The reactor was sunk under the hydroponics solution and atmospheric air was injected into the cylinder using a gas pump. Figure 2 shows a schematic of the discharge plasma system using the reactor. There are two treatment tanks. Ozone that remain undissolved in treatment tank 1

are effectively used in treatment tank 2. A pilot test of this system was carried out in greenhouse for 5 months. The system was operated for 8 h/day (5 days in a week). Plant was tomato (*Solanum lycopersicum* L., Momotaro Faito). Number of plant body was 15. Volume of hydroponics solution was around 100 L. We evaluated the dry weight of fruits, stem and leaf and the leaf area after 5 months cultivation to investigate an oxidative stress by ozone irradiation to plant roots.

The performance of the developed system on inactivation of bacteria was also evaluated using heavily contaminated hydroponics solution with *Ralstonia solanacearum*, a plant pathogenic bacterium. Plant was tomato (*Solanum lycopersicum* L., Rinka 409). Number of plant body was 15. Volume of hydroponics solution was around 10 L. *R. solanacearum* was added during operating the discharge plasma system for 100 minutes.

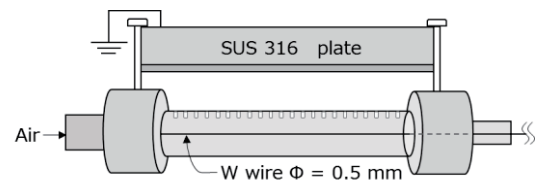


Fig. 1 Discharge plasma reactor

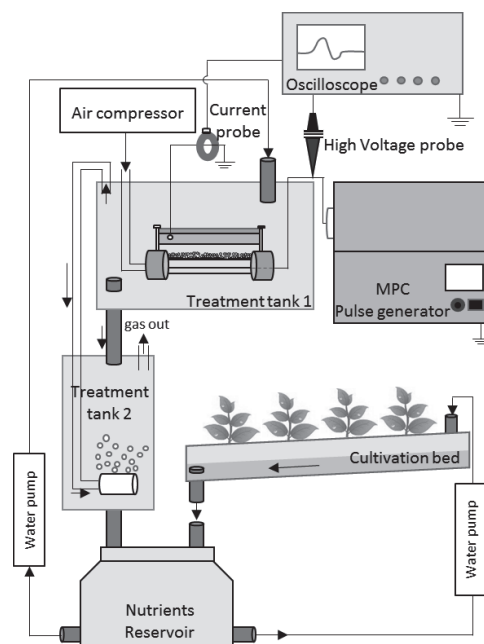


Fig. 2 A schematic of the discharge plasma system

### 3. Results and Discussion

#### 3.1 Characteristics of the developed discharge plasma reactor

Figure 3 shows wave forms of applied voltage to the wire electrode and flowed current to the ground through the plate electrode as shown in Figure 2. Peak voltage was around 10 kV. Pulse width and repetition rate was 150 ns and 2,000 pulse per second (pps), respectively. Since ozone is the most effective for inactivating bacteria, concentration of dissolved ozone into tap water of 100 L by operating the reactor was evaluated. Concentration of dissolved ozone was estimated by decolorization of indigo carmine dye that dissolved into the solution, based on two assumption: i) one ozone molecule decolorizes one indigocarmine molecule, and ii) only ozone decolorizes indigocarmine. Figure 4 shows the concentration of ozone produced by operating the discharge plasma system with time. In the early 30 minutes, concentration of dissolved ozone was approximately 0.3 ppm. *Rhizoctonia solani* causing root rot disease is generally sterilized in solution of ozone concentration at 0.3-0.5 ppm in 30-60 seconds.

#### 3.2 Pilot test of the discharge plasma system for 5 months in a green house

The developed system worked for 5 months in stable. Figures 5 and 6 show the dry weight of fruits, stem, leaf and the leaf area after 5 months. As shown in the figures, the all plant bodies healthily grew and produced fruit bodies normally without infection by bacteria. This result suggested the plants had no damage by the oxidative stress. On the other hand, discharge plasma also produces nitric acid in the solution, which acts as a fertilizer [13,14], however, significant increase of nitric acid was not observed in the hydroponics solution in the discharge plasma system. This is because nitric acid produced by discharge is much smaller than that originally included in the hydroponics solution.

#### 3.3 Performance of the developed system

*R. solanacearum* was added during operating the discharge plasma system for 100 minutes. We prepared two more experimental sections, one was a

negative control (no bacterium and no discharge plasma) and the other was a positive control (bacterial contamination and no discharge plasma). The number of colony forming unit (CFU) of *R. solanacearum* in the solution was obtained. Figure 7 shows photographs of the seedlings on the initial, 6 and 10 day. On the 6 day, almost all seedlings only in positive control developed symptoms of wilt disease and all of them wilted and died by infection of *R. solanacearum* on the 10 day. Other seedlings healthily grew. Figure 8 shows CFU of solution after the operation of the discharge plasma system for 100 minutes. The number of CFU of *R. solanacearum* in the solution was decreased from  $10^7$  to  $10^2$  CFU/mL by the discharge plasma. These results indicates that the bacterial wilt disease is significantly suppressed by the developed discharge plasma system.

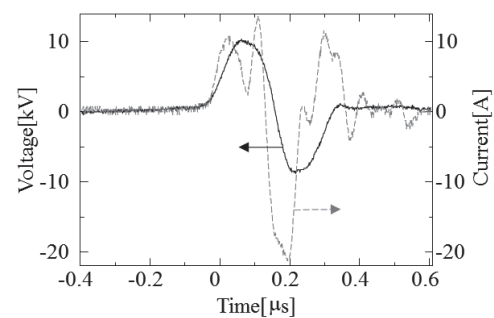


Fig. 3 Waveform of voltage that is applied to a wire electrode in the reactor and current that flows through a plate electrode to the ground

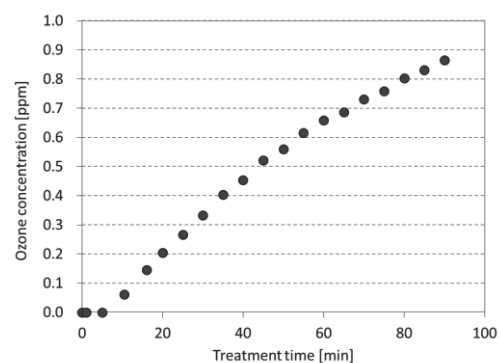


Fig. 4 the concentration of ozone produced by operating the discharge plasma system with time.

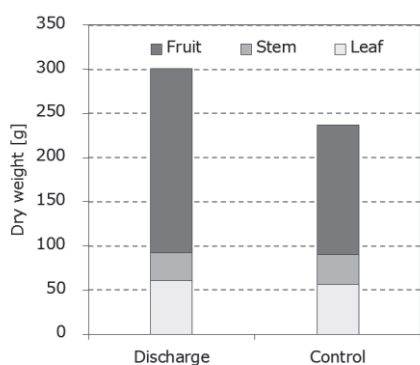


Fig. 5 The dry weight of fruits, stem, leaf

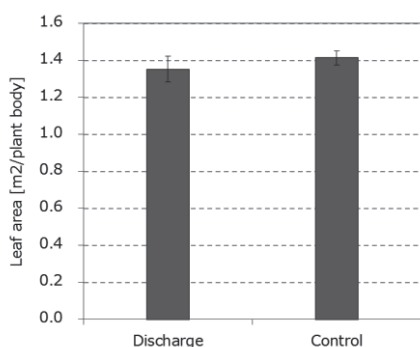


Fig. 6 The leaf area

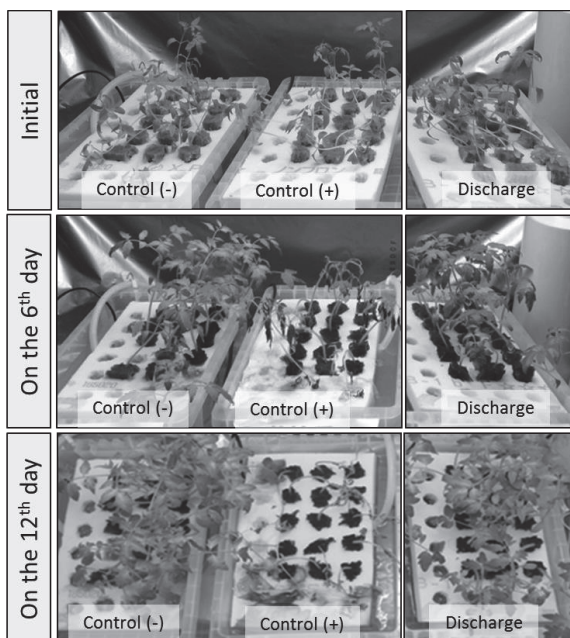


Fig. 7 Photographs of the seedlings on the initial, 6 and 10 day

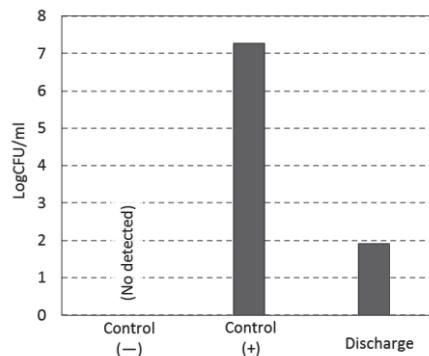


Fig. 8 CFU of the solution after the operation of the discharge plasma system for 100 minutes

#### 4. Conclusions

We developed a system using a discharge plasma under water for inactivating bacteria in hydroponic culture system, and evaluated the performance of the developed system in a greenhouse for 5 months using tomato plants in a hydroponics system. Moreover, the performance of the reactor was evaluated using a heavily contaminated hydroponics solution. Main conclusions are as follows:

- (i) Concentration of dissolved ozone into 100 L solution is approximately 0.3 ppm in the 30 minutes operation of the system.
- (ii) The developed discharge plasma system works in a greenhouse for 5 months in stable.
- (iii) All plant bodies healthily grow and produce fruit bodies normally without infection by bacterial disease and no damage by the oxidative stress.
- (iv) As for the 10 L hydroponics solution, the number of colony forming unit (CFU) of *R. solanacearum* in the solution can be decreased from  $10^7$  to  $10^2$  CFU/mL by operating the system for 100 minutes.
- (v) All seedlings in a positive control wilted and died by infection of *R. solanacearum*.

It can be concluded that the bacterial wilt disease is significantly suppressed by operating the discharge plasma system.

#### 5. Acknowledgements

We would like to thank Professor Y. Suzuki of Miyagi University for helpful suggestions. We also

thank Mr. H. Shida for his technical support. This research was supported by a Grant-in-Aid for Scientific Research (A) from the Japan Society for the Promotion of Science, Grant Number 15H02231 and the Collaborative Research Based on Industrial Demand of the Japan Science and Technology Agency.

## References

- [1] J. Woodward, "Some Thoughts and Experiments Concerning Vegetation By John Woodward, M. D. of the College of Physicians, et R.S. et Professor of Physick in Gresham College", *Philos. T.* **21**, pp.193-227 (1699)
- [2] Van Os EA, "Closed soilless growing systems: a sustainable solution for Dutch greenhouse horticulture", *Water Sci. Technol.* **39**, pp.105–112 (1999)
- [3] H. Rattink, "Root pathogens in modern cultural systems. Assessment of risks and suggestions for integrated control", *IOBC wprs Bullet* **19**, pp. 1-10 (1996)
- [4] M. Sato, K. Tokita, M. Sadakata, T. Sakata, and K. Nakanishi, "Sterilization of microorganisms by a high-voltage, pulsed discharge under water", *Int. Chem. Eng.* **30**, pp.695-698 (1990)
- [5] T. Ohshima, K. Sato, H. Terauchi, and M. Sato, "Physical and Chemical Modifications of High-voltage Pulse Sterilization", *J. Electrostatics* **42**, 159-166 (1997).
- [6] H. Akiyama, "Streamer discharges in liquids and their applications", *IEEE Trans. Dielectr. Electr. Insul.* **7**, pp.646-653 (2000).
- [7] M. Sato, "Environmental and biotechnological applications of high-voltage pulsed discharges in water", *Plasma Sources Sci. Technol.* **17**, 024021 (2008).
- [8] K. Takahashi, Y. Sasaki, S. Mukaigawa, K. Takaki, T. Fujiwara, and N. Satta, "Purification of High-Conductivity Water Using Gas-Liquid Phase Discharge Reactor", *IEEE Trans. Plasma Sci.* **38**, pp.2694-2700 (2010)
- [9] J. S. Chang, P. A. Lawless, and T. Yamamoto, "Corona discharge processes", *IEEE Trans. Plasma Sci.* **19**, pp.1152-1166 (1991)
- [10] K. Ebihara, M. Takayama, T. Ikegami, K. Ogata, H. D. Stryczewska, Y. Gyoutoku, and T. Sakai, "Development of agricultural soil sterilization using ozone generated by high frequency dielectric barrier discharge", *J. Adv. Oxid. Technol.* **9**, pp.170-173 (2006).
- [11] K. Takaki, J. Takahata, S. Watanabe, N. Satta, O. Yamada, Y. Sasaki, and T. Fujio, "Improvements in plant growth rate using underwater discharge" *J. Phys.: Conf. Ser.* **418**, 012140 (2013).
- [12] J. Takahata<sup>1</sup>, K. Takaki<sup>1</sup>, N. Satta, K. Takahashi, T. Fujio, Y. Sasaki, "Improvement of growth rate of plants by bubble discharge in water", *Jpn. J. Appl. Phys.* **54** (2015).
- [13] B. Wenjuan, Y. Xiangli, "Nitrogen Fixation into HNO<sub>3</sub> and HNO<sub>2</sub> by Pulsed High Voltage Discharge", *Plasma Sci. Technol.* **9**, pp.288-291 (2007)
- [14] B. Wenjuan, S. Junwen, Y. Xiangli, "Nitrogen Fixation Into Water by Pulsed High-Voltage Discharge", *IEEE Trans. Plasma Sci.* **37**, pp.211-218 (2009).

# Characterization of Surrounding Gas-Fed Atmospheric Pressure Plasma Jet using a Double Coaxial Glass Tube

Kohei Oyama, Tetta Mitani, Hayato Ohashi, Hiroaki Ito

*Department of Electrical and Electronic Engineering,  
University of Toyama, 3190 Gofuku, Toyama 930-8555, Japan*

## ABSTRACT

We report the characteristics of developed surrounding gas-fed plasma jet using a double coaxial glass tube. Two gas flows can introduce independently into the tube and the gas and plasma flows interact outside of the glass tube. With an outer nitrogen ( $N_2$ ) and an inner argon (Ar) gas flows, the plasma jet can be extended up to 44 mm while with both pure  $N_2$  and mixing gas of  $N_2$  and Ar, a conventional single glass tube cannot extend the jet to such length. In the case of helium (He) as an inner gas flow with an outer  $N_2$  gas flow, emission lines of nitric oxide, the first negative and second positive system bands of  $N_2$  were observed, while only the second positive system band was observed in the case of Ar as the inner one. Considering the Penning effects of each excited state, the metastable state of He has a higher energy than that of Ar, resulting in energetic nitrogenous productions in the former case. The excited state in the core plasma is one of the important conditions to determine the characteristics of the APPJ produced with a double coaxial glass tube.

## Keywords

Atmospheric pressure plasma jet, dielectric barrier discharge, optical emission spectroscopy

## 1. Introduction

In recent years, an atmospheric pressure plasma jet (APPJ) has been attracted attentions for surface processing and agricultural and biomedical applications. Investigative efforts then reveal that reactive oxygen species (ROS), e.g., hydroxyl radical (OH), and reactive nitrogen species (RNS) play important roles in the effects, such as surface treatment of  $TiO_2$  [1], gene transfection [2], promotion of plant growth [3], tooth bleaching [4], sterilization [5], blood coagulation [6], wound healing [7, 8] and even cancer treatment [9]. The ROS or RNS rich plasma jet, therefore, has a potential as an advanced versatile tool. Furthermore, the plasma jets have advantages: operation at room temperature, easy to miniaturize and inexpensive because they do not need any vacuum system and can be operated with various feeding gases under a wide range of driving frequencies [10].

In order to meet the requirements of research and industrial application, it is very important for the APPJ

to have a higher capability to control various operational conditions. The conventional APPJ with a single glass tube is operated with mixed gas to increase productions of reactive species. The mixing ratio, however, is below only a few percent due to the negative reactions for stable plasma discharge resulting in the limitation of productions of radical species [11, 12].

We have developed a surrounding gas-fed plasma jet with a double coaxial glass tube for the increase of radical productions. The double coaxial glass tube can make a laminar flow by introducing an additional gas flow in parallel to core gas flow. The laminar-flow APPJ can control the flow rates of two gases separately using independent injection ports. This mechanism is expected to extend the plasma jet length with a guiding effect by the surrounding gas flow. Therefore, the increase of the jet length leads to an improvement of the effective reaction area for Penning effect related to the production of radical species

leading to the increase of radical productions. In addition, the surrounding gas-fed APPJ has the electric field in direction transverse to the gas flow, while the conventional APPJ has in the parallel direction. Reaction processes strongly depend on the potential, excitation and ionization energies of particles in the APPJ. It is important for various applications to investigate the fundamental characterization of laminar flow APPJ. In this paper, we observed the emission spectra of the surrounding gas-fed plasma jet with a double coaxial glass tube and evaluated the dependence of the laminar flow APPJ on the core plasma and the electrode structure by comparing with the conventional APPJ.

## 2. Experimental Setup

Figure 1 shows a cross-sectional view of a double coaxial glass tube and the schematic diagram of an experimental setup. The glass tube consists of inner, intermediate and outer glass tubes and the size of each tube is shown in Table 1. An acrylic spacer and a grounded brass electrode were between the glass tubes, as shown in Fig. 1. There are two independent paths

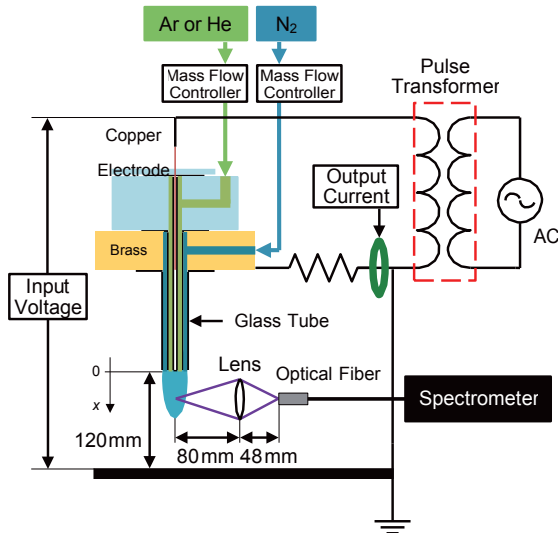


Fig. 1 A cross-sectional view of the double coaxial glass tube and experimental setup.

Table 1 Size of each glass tube of double coaxial glass tube.

Tube type	Inner dia.	Outer dia.	Length
Inner	2 mm	3 mm	120 mm
Intermediate	7 mm	9 mm	85 mm
Outer	13 mm	15 mm	60 mm

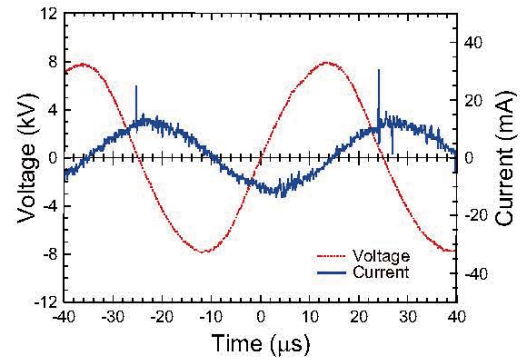


Fig. 2 Typical waveforms of applied voltage (dotted line) and an output current (solid line).

for central and surrounding gas flows. With this double coaxial structure, two different gases can introduce into the glass tube and can control each flow rate independently. The copper electrode was placed inside the inner tube to prevent sputtering by the plasma. The sinusoidal voltage generated by a step-up transformer of 8 kV with a frequency of 20 kHz was applied to the electrodes to induce the dielectric-barrier discharge. The resistor of 100 k $\Omega$  was used to limit the circuit current to below the transformer ampacity. Figure 2 shows the typical waveforms of the applied voltage and the output current measured by a high voltage probe (P6015A, Tektronix, Inc.) and a current transformer (4100, Pearson Electronics, Inc.), respectively. These waveforms were almost the same even if different gas species were used for the inner flow. As seen in Fig. 2, the characteristic of the dielectric-barrier discharge, i.e. nanosecond-order pulse discharges, was observed in the current waveform.

Argon (Ar) and helium (He) gases were used for an inner gas flow to produce the core plasma, and nitrogen ( $N_2$ ) gas was used for a surrounding gas flow. Each flow rate was controlled by a mass flow controller (8500MC-S3-1-2, KOFLOC Co., Ltd.). Argon or helium gas was passed through the inner path with a flow rate of 5 L/min and the plasma was produced by the dielectric-barrier discharge. On the other hand,  $N_2$  gas was passed through the outer path with 0–6 L/min. Emission spectra with an exposure time of 0.4 s were measured by using a spectrometer (EPP2000, StellarNet Inc.) in a wavelength range of 200–1000 nm with a typical full width at half

maximum of 2.5 nm. Emissions from a spot area with a diameter of 1 mm in the plasma jet, i.e., effective spatial resolution in the experiment, were focused into the optical fiber connecting to the spectrometer by using a double-convex lens of the focal length of 30 mm. The spectral distribution of the emission spectra of the APPJ was measured by moving the optical fiber from a tip of the glass tube toward the grounded aluminum board with the step of 2 mm.

### 3. Results and Discussion

Figure 3 shows the surrounding  $N_2$  flow rate dependence on the plasma jet length measured with photographs taken from the side view. The jet length extends obviously with the increase of the  $N_2$  flow rate and seems to be saturated at 44 mm over about 5 L/min. Figure 4 shows the schlieren images during discharge operation measured by using a schlieren system (SS100, KATO KOKEN Co., Ltd.) and a high-speed camera (Phantom v2011, Nobby Tech., Ltd.). Here, the flow rates of inner Ar gas and outer  $N_2$  gas are 5 L/min and 3 L/min, respectively. As seen in Fig. 4(a), the single Ar plasma jet seems to diffuse around a tip of the plasma jet. It turns from Fig. 4(b) that the surrounding  $N_2$  flow (the dark stream part) confines

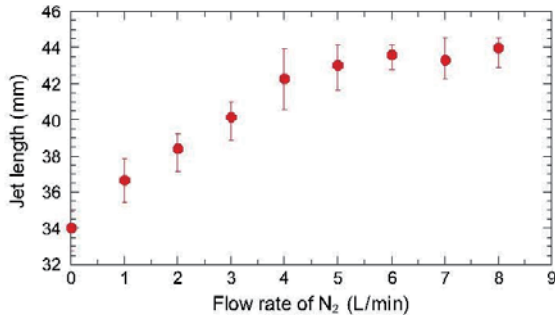


Fig. 3 Flow rate dependence of the jet length on outer  $N_2$  gas while inner Ar gas with 5 L/min.

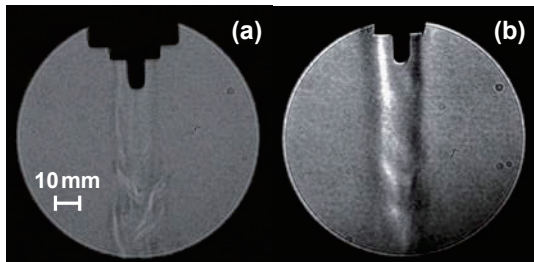


Fig. 4 Schlieren images of Ar plasma jets during discharge operations (a) without and (b) with outer  $N_2$  gas flow.

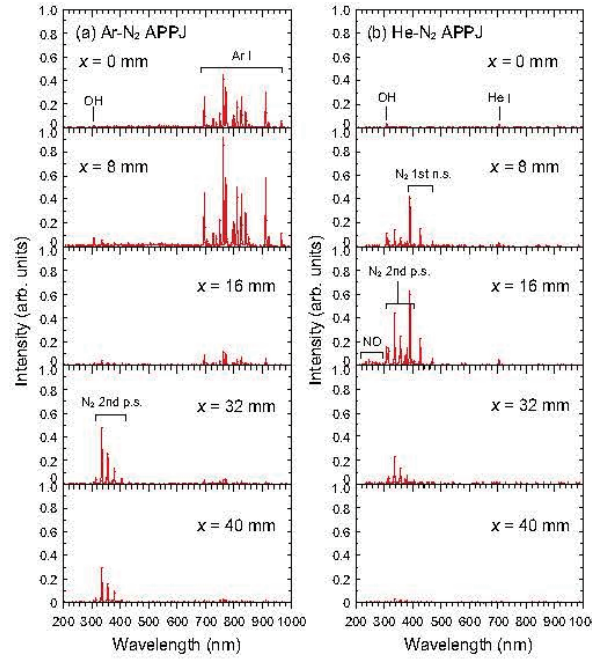


Fig. 5 Typical emission spectra of (a) Ar- $N_2$  and (b) He- $N_2$  APPJs observed at  $x = 0, 8, 16, 32$  and  $40$  mm, respectively.

and guides the inner Ar plasma flow. Thus, this effect leads to the extension of the region of the effective interaction to produce excited  $N_2$ .

Figure 5 shows the typical emission spectra observed at  $x = 0$ – $40$  mm with flow rates of 5 and 3 L/min for inner Ar or He and surrounding  $N_2$  gases, respectively. In the case of Ar- $N_2$  APPJs (see Fig. 5(a)), emission intensities of Ar I transitions in the range of 700–1000 nm have a maximum peak near the tip of the glass tube and then decrease with the increase in observing distance. On the other hand, the emissions from  $N_2$  corresponding to the second positive system ( $N_2$  2nd p.s.:  $C^3\Pi_u \rightarrow B^3\Pi_g$ ) transitions in the range of 310–410 nm become more intense with the increase in the distance from  $x = 16$  mm, then become weaker with a further increase in the distance. In the case of He- $N_2$  APPJs, (see Fig. 5(b)), emissions from not only  $N_2$  2nd p.s. but also  $N^+$  corresponding to the first negative system ( $N_2$  1st n.s.:  $B^3\Pi_g \rightarrow A^3\Sigma_u$ ) transitions and NO corresponding to  $\gamma$ -system ( $A^2\Sigma^+ \rightarrow X^2\Pi_{1/2}$ ) transitions were observed in the ranges of 390–470 nm and 200–300 nm, respectively.

We verified the shielding effect of the surrounding

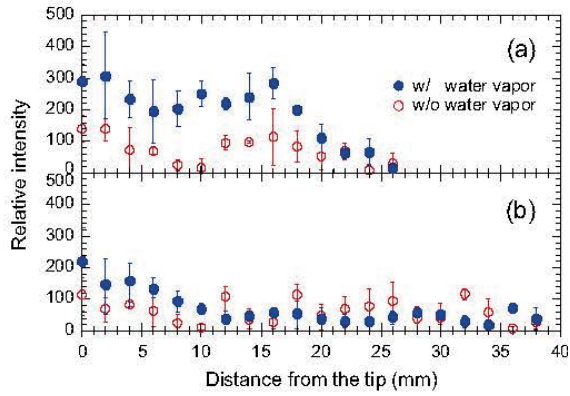


Fig. 6 Dependence of the OH radical emission intensity on both distance from the tip of glass tube and with (solid) or without (open) the water vapor of humidifier. The flow rate of inner Ar was 5 L/min for (a) pure Ar plasma jet and with surrounding N<sub>2</sub> gas flow was at 3 L/min for (b) Ar-N<sub>2</sub> laminar plasma jet.

gas by changing the environmental humidity using a humidifier for Ar plasma jet. Figure 6 shows the dependence of OH radical intensities on the presence of a humidifier. As shown in Fig. 6(a), emissions from OH radicals increase with the increase of the humidity in the case of pure Ar plasma jet. On the other hand, with surrounding N<sub>2</sub> gas flow, there is no significant increase of OH radical emissions in spite of purposely increase of humidity as shown in Fig. 6(b). Therefore, the surrounding N<sub>2</sub> gas flow, as seen in Fig. 4(b), has a shielding effect to prevent the interaction between inner Ar plasma jet and environmental H<sub>2</sub>O [15]. This effect is an advantage for the use in unstable environmental conditions.

Figure 7 shows the dependence of the emission intensity for each intense line on the distance from the tip, i.e., Ar I 4s–4p transition at 763 nm, He I 2p–3s transition at 707 nm, OH radical at 309 nm, NO radical at 245 nm, N<sub>2</sub> 1st n.s. at 391 nm and N<sub>2</sub> 2nd p.s. at 337 nm, respectively. Here, the flow rate of inner Ar or He was 5 L/min with surrounding N<sub>2</sub> gas flow rate of 3 L/min. Error bars indicate the highest and lowest values. The surrounding N<sub>2</sub> gas interacts with a central Ar or He plasma jet at the interface of them outside of the glass tube, and then excited N<sub>2</sub> species are produced. Energies of each lowest metastable state (Ar I 3s<sup>2</sup>3p<sup>5</sup>4s and He I 1s2s) are 11.5 eV and 19.8 eV, and are suitable to produce upper states of N<sub>2</sub> 2nd p.s. and

N<sub>2</sub> 1st n.s., respectively, by the energy transfer and Penning ionization. In the case of He–N<sub>2</sub> plasmas, the upper states of N<sub>2</sub> 2nd p.s. also could be produced by the decay of N<sub>2</sub><sup>+</sup>. On the other hand, the metastable of Ar does not have enough energy to ionize N<sub>2</sub>. Since N<sub>2</sub><sup>+</sup> has relation to the production process of NO [13], emissions from NO were observed only in the case of He–N<sub>2</sub> plasmas. The vibrational temperatures of N<sub>2</sub> in Ar–N<sub>2</sub> and He–N<sub>2</sub> plasma jets are estimated to be 1131 K and 2071 K, respectively, by using the ratio of emission intensities of N<sub>2</sub> 2nd p.s. ( $v=0,1 \rightarrow v''=0$ ) [14]. It is reasonable to suppose that the He–N<sub>2</sub> APPJ has higher temperature than Ar–N<sub>2</sub> because the production process of upper states of N<sub>2</sub> 2nd p.s. would be cascade decays from higher energy states. On the other hand, emission lines corresponding to rotational excitations were not observed clearly, while it was observed in other shielding gas APPJ [15]. As above-mentioned, components and conditions of APPJs strongly depend on feeding gas flow and species.

Figure 8 shows the gas flow rate and observing distance dependences of emission intensity for each intense line, where the flow rates of inner Ar or He and outer N<sub>2</sub> gases are 5 L/min and 0–6 L/min, respectively. Each emission intensity increases with the increase of N<sub>2</sub> flow rate up to 4 L/min except the cases of Ar and OH in the Ar–N<sub>2</sub> APPJ. The double coaxial glass tube can produce excited N<sub>2</sub> rich plasma jet, since the

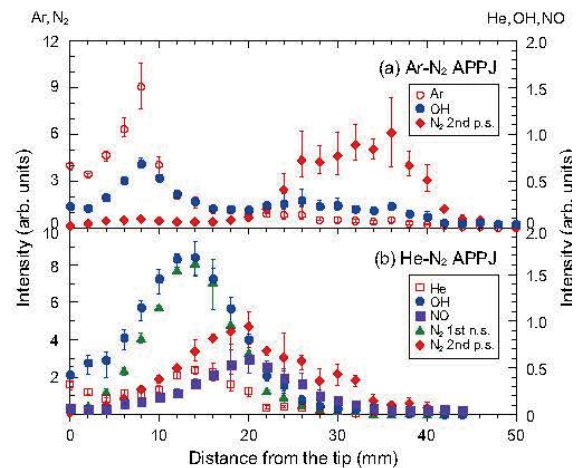


Fig. 7 Dependence of emission intensity for Ar (open circle), He (open square), OH (solid circle), NO (solid square), N<sub>2</sub> 1st n.s. (triangle) and N<sub>2</sub> 2nd p.s. (diamond) on distance from the tip.

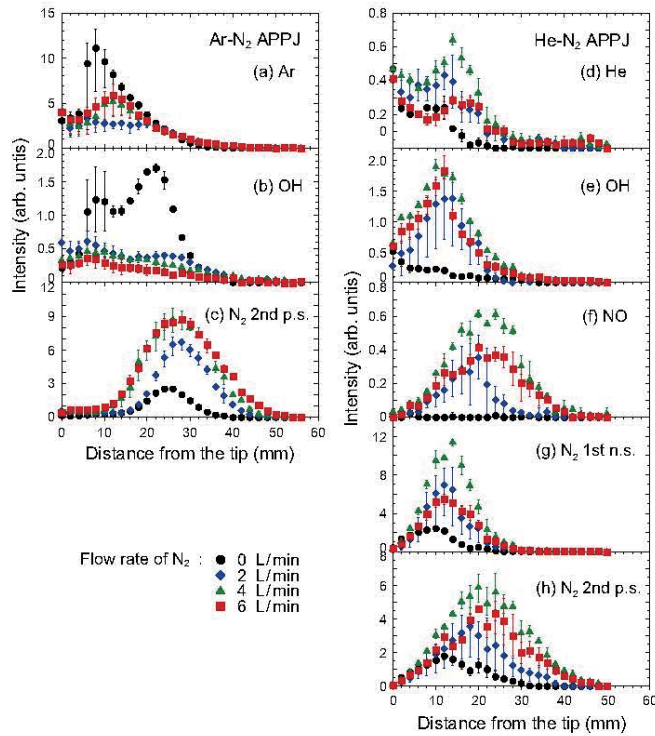


Fig. 8 Flow rate and distance dependences of emission intensity for each intense line;(a) Ar, (b) OH and (c) N<sub>2</sub> 2nd p.s. of He-N<sub>2</sub> APPJs, and (d) He, (e) OH, (f) NO, (g) N<sub>2</sub> 1st n.s. and (h) N<sub>2</sub> 2nd p.s. of Ar-N<sub>2</sub> APPJs.

effective reaction area and the time of excited Ar and He increase with the increase in the flow rate of N<sub>2</sub> gas. In the case of a conventional single jet structure with both pure and mixing gas of N<sub>2</sub>, nitrogen plasma jet is known to be difficult to produce and extend its length. Actually, the plasma jet could not extend over 20 mm and be produced with a ratio of N<sub>2</sub> more than 2% using the inner path with a mixing gas of Ar and N<sub>2</sub> (not shown). Therefore, the double coaxial glass tube can produce and expand excited N<sub>2</sub> rich plasma jet, since the effective reaction area and time of excited Ar increase with the increase in the flow rate of N<sub>2</sub> gas. This effect is the characteristics of the double coaxial glass tube and could be the same for using other gases. With further increase of the N<sub>2</sub> flow rate, each intensity decreases due to difference of adequate conditions, such as a velocity matching, for effective reactions. Since the production of OH radicals corresponds to the interaction of Ar species with H<sub>2</sub>O in the air, the shielding effect [15] of surrounding N<sub>2</sub> gas flow prevents the interaction between inner Ar plasma jet

and environmental H<sub>2</sub>O, resulting in the decrease of emission intensities of both Ar and OH. In contrast, in the case of the He-N<sub>2</sub> APPJ, it is possible to produce N<sub>2</sub><sup>+</sup> of which potential energy is higher with respect to neutral N<sub>2</sub>, since the metastable of He has a higher potential energy than that of Ar. As a result, the interaction of energetic N<sub>2</sub><sup>+</sup> with H<sub>2</sub>O in ambient air contributes to the production of OH radicals. Therefore, each emission intensity of He, OH and N<sub>2</sub> 1st n.s. (N<sub>2</sub><sup>+</sup>) has peak at same distance as shown in Figs. 8(d), 8(e) and 8(g). It is evident from Fig. 8(f) that NO is produced only when the N<sub>2</sub> gas flows with He plasma jet. Therefore, the effect of the laminar flow APPJ, i.e., the increase of the effective reaction area and time, could lead to enhance the formation rate of NO drastically.

#### 4. Conclusions

We have the fundamental characteristic evaluation of a laminar APPJ. The double coaxial glass tube makes a laminar flow and enhances the effective reaction area and the time of inner and surrounding flow components in the APPJ. The excited state in the core plasma is one of the important conditions to determine the characteristics of the APPJ. Therefore, the laminar flow APPJs have a wide controllability by the choice of gas species, its flow rate and the feeding path. Various other gases can be applied to the double coaxial glass tube to produce reactive APPJs for biomedical, agricultural and surface processing applications.

#### References

- [1] T. Yuji, et al., "Surface treatment of TiO<sub>2</sub> films for dye-sensitized solar cells using atmospheric-pressure non-equilibrium DC pulse discharge plasma jet", *Vacuum*, **83**, pp.124-127 (2008).
- [2] S. Sasaki, et al., "Highly efficient and minimally invasive transfection using time-controlled irradiation of atmospheric-pressure plasma", *Appl. Phys. Express*, **7**, p.026202 (2014).
- [3] D. P. Park, et al., "Reactive nitrogen species

- produced in water by non-equilibrium plasma increase plant growth rate and nutritional yield”, *Curr. Appl. Phys.*, **13**, pp.S19-S29 (2013).
- [4] S. H. Nam, et al., “High-efficiency tooth bleaching using non-thermal atmospheric pressure plasma with low concentration of hydrogen peroxide”, *J. Appl. Oral Sci.*, **21**, pp.265-270 (2013).
- [5] S. Ikawa, K. Kitano, and S. Hamaguchi, “Effects of pH on Bacterial Inactivation in Aqueous Solutions due to Low-Temperature Atmospheric Pressure Plasma Application”, *Plasma Process. Polym.*, **7**, pp.33-42 (2010).
- [6] U. Kalghatgi, et al., “Mechanism of Blood Coagulation by Nonthermal Atmospheric Pressure Dielectric Barrier Discharge Plasma”, *IEEE Trans. Plasma Sci.*, **35**, pp.1559-1566 (2007).
- [7] G. Lloyd, “Gas Plasma: Medical Uses and Developments in Wound Care”, *Plasma Process. Polym.*, **7**, pp.194-211, (2010).
- [8] S. Fathollah, et al., “Investigation on the effects of the atmospheric pressure plasma on wound healing in diabetic rats”, *Sci. Rep.*, **6**, p.19144, (2016).
- [9] Th. von Woedtke, et al., “Plasmas for medicine”, *Phys. Rep.*, **530**, pp.291-320, (2013).
- [10] D. B. Kim, et al., “The driving frequency effects on the atmospheric pressure corona jet plasmas from low frequency to radio frequency”, *Phys. Plasma*, **18**, p.043503, (2011).
- [11] T. Yuji, et al., “Experimental Study of Temperatures of Atmospheric-Pressure Nonequilibrium Ar/N<sub>2</sub> Plasma Jets and Poly(ethylene terephthalate) - Surface Processing”, *Jpn. J. Appl. Phys.*, **46**, pp.795-798, (2007).
- [12] A. V. Pipa and J. Röpcke., “Analysis of the Mid-Infrared Spectrum of the Exhaust Gas From an Atmospheric Pressure Plasma Jet (APPJ) Working With an Argon-Air Mixture”, *IEEE Trans. Plasma Sci.*, **37**, pp.1000-1003, (2012).
- [13] D. D. Cleary, “Daytime high-latitude rocket observations of the NO  $\gamma$ ,  $\delta$ , and  $\epsilon$  bands”, *J. Geophys. Res.: Space Phys.*, **91**, pp.11337-11344 (1986).
- [14] H. Akatsuka, “Progresses in Experimental Study of N<sub>2</sub> Plasma Diagnostics by Optical Emission Spectroscopy”, *Chemical Kinetics*, Ch.13, edited by Vivek Patel, InTech, (2012).
- [15] S. Reuter, et al., “Controlling the Ambient Air Affected Reactive Species Composition in the Effluent of an Argon Plasma Jet”, *IEEE Trans. Plasma Sci.*, **40**, pp.2788-2794, (2012).

# DNA fragmentation and Caspase-3 Activation of HeLa Cells Induced by Intense Burst Sinusoidal Electric Fields

Ryuta Andachi, Masahiko Yano, Keisuke Abe, Sunao Katsuki\*

*Graduate School of Science and Technology, Kumamoto University*

*\*Institute of Pulsed Power Science, Kumamoto University*

## ABSTRACT

This paper describes biological responses of cultured HeLa cells to non-thermal narrowband intense pulsed electric fields. 100-300 kV/m, 200  $\mu$ s-long intense burst sinusoidal electric fields (IBSEF) with a frequency between 0.3 and 100 MHz were repetitively applied to the cells. Morphology, viability, intracellular DNA fragmentation and gene expression of active caspase-3, which is an indicator of apoptotic activity, were investigated in the cells exposed to IBSEF. The viability and the DNA fragmentation were evaluated by means of propidium iodide staining and alkaline comet assay, respectively. The cell responses to the IBSEF depend on the frequency and electric fields strength, and varied with the incubation time after the exposure. The cell responses were obvious at lower frequency range less than 1 MHz and at larger electric field strength more than 200 kV/m. DNA fragmentation, active caspase-3 as well as bleb formation were observed immediately after the IBSEF exposure, and gradually advanced with time, whereas the cells were not stained with propidium iodide for 30 minutes. This frequency dependence indicating that intensity of electrical stress on membrane is important factor in cell death.

## Keywords

Pulsed electric field, DNA fragmentation, HeLa cells

## 1. Introduction

Recently biological effects of pulsed intense electric fields with broad and narrow frequency bands have been discussed frequently for the concern of an electromagnetic irradiation from advanced electronic devices, and for the interest in utilizing the effects of novel electrostatic biological stresses in medical, pharmacological and agricultural fields. The effect of nanosecond pulsed electric fields (nsPEF) has been intensively investigated by Schoenbach et al [1]. They reported that nsPEF enables us to bring an electromagnetic energy to the interior of the cell and to cause unique, intracellular effects [1, 2]; while pulsed electric fields (PEFs) with duration of microseconds or more increases the permeability of the plasma membrane, which is called electroporation

[3]. The intracellular effects of nsPEF are considered to be used for medical treatments, such as melanoma inactivation [4], and wound healing based on platelet activation [5]. It is known that the dielectric dispersion that electrical impedance of biological cells depends on the frequency component of the applied electric field since they're composed of various dielectric materials. Especially, the lipid bilayer bio-membrane, which is regarded as an insulating dielectric thin film, that influence the electric field distribution over the cell in the frequency range between 50 kHz and 50 MHz Also, a number of intracellular organelles such as the nucleus, mitochondria, endoplasmic reticulum, and so forth, make the field distribution complicated. NsPEFs, which are often used to give intracellular

effects to biological targets, produce high frequency components that are determined by their rise time and pulse duration, since their frequency components are broadly scattered, the electrical stresses are considered to be scattered over the cell. Based on this idea, a narrow band frequency spectrum is favorable to discuss physical effects of electric fields, in order to allow giving an electrical stress to a specific target of the cell. We have proposed the use of an intense burst sinusoidal electric field (IBSEF), one with narrow band frequency spectrum, which produces the well-defined parameters, including frequency, average field strength and burst duration. Previously, we have reported that the response of the Chinese hamster ovary (CHO) cells to the IBSEF depends on the frequency. The degradation of intracellular DNA occurs at the frequency of 2 MHz or more, while a membrane defect occurs at a frequency below 2 MHz [6, 7].

We have investigated the influence on intracellular DNA of HeLa cells subjected to non-thermal IBSEF, and the cell death by means of alkaline comet assay and the PI staining. The burst duration was fixed at 200  $\mu$ s-long in each experiment, in order to minimize the thermal effect. The frequency was varied in the range between 0.3 and 100 MHz since the electric field distribution over the cell is expected to alter drastically.

## 2. Materials and Methods

### 2.1 IBSEF application system

The IBSEF application system is described in detail in REF [6]. The IBSEF generator consists of a signal generator (E4400B, Agilent) to generate a sinusoidal wave with a certain frequency between 300 kHz and 100 MHz, a pulse generator (Type 555, Berkeley Nucleonics) to determine the burst duration and a radio frequency amplifier (2088 BBS1C3CRR, Empower RF Systems) as shown in Fig. 1. The 200  $\mu$ s-long burst AC voltage with amplitudes up to a maximum 300 V was repetitively delivered to a commercially available 1 mm-gap cuvette and 200  $\mu$ m gap electrodes on slide glass through a 50  $\Omega$  coaxial cable (RG213/U). The interval between the

pulses is 3 sec., which is sufficiently long to suppress the temperature increase of the cell suspending medium within 6  $^{\circ}$  C [7]. The resistance and capacitance of the cuvette are approximately 50  $\Omega$  at 100 MHz. The power density during the burst reaches 90 GW/kg. 200  $\mu$ m gap electrodes are produced by vapor-depositing gold on glass. The thickness of gold is approximately 20  $\mu$ m. The voltage between the electrodes was monitored by using a calibrated voltage divider every shot.

### 2.2 Preparation of cells

All experiments in this proposal were conducted using HeLa cells cultured in an incubator (5% CO<sub>2</sub>, 95% air, 37  $^{\circ}$  C) with  $\alpha$  minimum essential medium ( $\alpha$  MEM) including 10% fetal bovine serum (FBS). Cells were moderately passage through every 2 or 3 days, before getting 80% confluent. Cultured cells were washed by PBS (-) (phosphate buffered saline pH 7.4) twice, detached by PBS base 1mM EDTA (etylendiaminetetraacetic acid), suspended by  $\alpha$  MEM containing 10% FBS, and centrifuged at 1,000 rpm for 5 minutes. Then they were re-suspended to  $2 \times 10^6$  cells/ml with  $\alpha$  MEM before use, and in a 15 ml centrifuge tube. Finally, they were stored in the CO<sub>2</sub> incubator during the experiment.

### 2.3 Cell morphology

Cells exposed to the pulses were observed by using a phase contrast and fluorescent microscope. After IBSEF application, the cells were collected from cuvette and diluted with  $\alpha$  MEM to be the density of  $1 \times 10^6$  cells/ml. Then we observe them using a confocal laser microscope (DMI6000B, Leica).

### 2.4 Detection of DNA fragmentation

A number of techniques for detecting DNA damage, as opposed to the biological effects (e.g., micronuclei, mutations, structural chromosomal aberrations) that result from DNA damage, have been used to identify substances with genotoxic activity. A more useful approach for assessing DNA damage is the single-cell gel or comet assay [8-10]. In this paper, comet is used to identify the individual cell DNA migration patterns produced by this assay. Comet

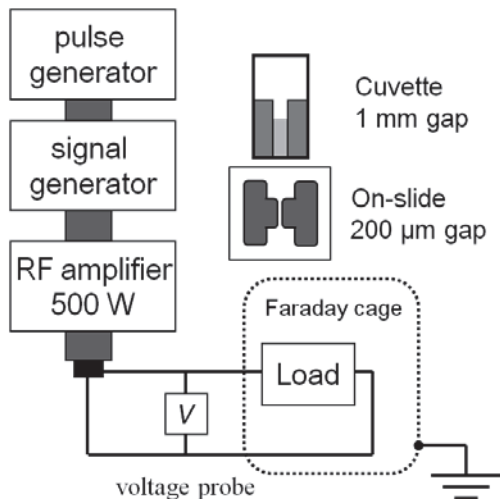


Figure 1. Schematic diagram of IBSEF applying system.

assay method was operated in a dim room with the constant temperature of 25°C. All experimental components which are in contact with the cells were pre-sterilized to avoid nuclease contamination. This procedure was operated for stabilizing the controlled cells. Coat a microscope slide with super pure water agar gel (1% agars in super pure water) in advance, and spread each PBS gel (1% agar in PBS, stored in 37°C) of 100  $\mu$ l mixed sample of 10  $\mu$ l. then the microscope slides are stored in 4°C to harden the gel and stop all biological processes. The above mentioned procedure was completed after IBSEF exposure at the time of 5 min (immediately after IBSEF), 30 min and 1 hour after voltage application precisely. The cooling time was strictly controlled for 20 minutes. The cells on the microscope slide were soaked for 2 hours in a lysing solution (5% sodium N-lauronyl sarcocinate, 2.5 M NaCl, 100 mM EDTA, 10 mM Tris, 1% Triton, containing 0.02% proteinase K, pH 10 by NaOH) at 4°C in the dark to dissolve the cell membranes and proteins [8]. Using this protocol, rather than overnight incubation with proteinase K, the total time taken for lysis and de-condensation of DNA could be reduced to 3 h and the baseline DNA damage could be reduced [9].

Electrophoresis was conducted with a voltage of 25 V for 20 min on ice after 20 min equilibration in the electrophoresis buffer (1 mM EDTA, 0.3 M NaOH). Then, the sample was equilibrated with 0.4

M tris buffer (pH 7.5) for 15 minutes. Finally, the sample was stained with 20  $\mu$ l SYBR® Green I diluted by 1/10000 with Tris-HCl (0.4 M, pH 7.5). SYBR® Green I is a fluorescent dye which is permeable to living cells and intercalates with the double-strand DNA (dsDNA), and fluoresces in green (519 nm). Each sample was observed by a fluorescent microscope (ECLIPSE E600, Nikon) in the dark.

### 2.5 Cell Viability

Propidium Iodide (PI) staining, as measured by flow cytometry 0 to 2 h incubation after IBSEF with the strength of 300 kV/m exposure, served as a principal index of cell death. PI was added to an aliquot of exposed cells 15 min prior to measurements to a final concentration of 10  $\mu$ g/ml. A total of 5,000 cells per sample were checked for propidium uptake using a PERFLOW Sort (PERFLOW Sort, Furukawa Electric co.). Cells that showed negative PI fluorescence intensity were defined as viable.

### 2.6 Expression of Caspase-3

The caspase family of cysteine proteases plays a key role in apoptosis. It is now well established that certain caspases (caspase-8, caspase-9, and caspase-10 in humans) play upstream “initiator” roles in apoptosis by coupling cell death stimuli to the downstream “effector” caspases (caspase-3, caspase-6, and caspase-7). Apoptotic death is generally distinguished from necrotic death by early nuclear compaction into densely defined masses at the nuclear periphery, cytoplasmic condensation, and nuclear fragmentation. Eventually, the cell progressively disintegrates into membrane bound apoptotic bodies with intact organelles and a possible nuclear component. It is an ongoing process involving both the replacement and deletion of damaged cells, which represents a regular function of cellular organisms. The most clearly defined biochemical event in apoptotic cells is nucleosomal fragmentation [10,11]. Caspase-3 is related to nucleosomal fragmentation. Caspase-3 induces decomposition of inhibitor of caspase activated deoxyribonuclease (DNase) and activation of caspase activated DNase.

In this paper, we investigated if caspase 3 is activated by applying IBSEF because it is the most extensively studied apoptotic protein among caspase family members. The cells were harvested at the time of 5min, 30min, 1 hour and 2 hours after starting exposure to 100 shots of IBSEF with field strength of 300 kV/m. Each samples was centrifuged 5 minutes at 1500 g, and added 500  $\mu$ l of 4% paraformaldehyde with PBS (Nacalai Tesque). Then, samples were incubated for 8 hours at 4 temperature degree. Each samples are immersion fixed in 4 % paraformaldehyde and added 1ml of D-PBS (WAKO co.). It is centrifuged at 1500 g for 5 min. They are removed the supernate and added to FACS permeabilizing solution 2 (BD Bioscience). After 10 min incubation at room temperature, 1 ml D-PBS is added to samples and centrifuged for 5 min. The centrifuged samples are added to active caspase 3 antibody (Abcam) with 0.5% Albumin from Bovine Serum Globulin Free (Wako) in PBS and kept in 4°C overnight. After incubation, the Anti-Rabbit IgG-FITC (Sigma) as secondary antibody is added to samples with active caspase-3 antibody and stored in 4°C for 8 hours. After that, antibodies treated cells are checked for fluorescence of active caspase 3-FITC using a PERFLOW Sort.

### 2.7 Detection of Intracellular $\text{Ca}^{2+}$

There is a  $\text{Ca}^{2+}$  release in upstream of caspase3-signaling in HeLa cell. The activation of endonucleases is well known to be mediated by cytoplasmic and nuclear  $\text{Ca}^{2+}$  concentration [18-20]. The  $\text{Ca}^{2+}$  concentration is possibly mediated by ER stress. It is reported that ER pathway is the one which

mediated rapid apoptosis of HeLa cells [21]. Furthermore, pulsed electromagnetic fields and pulsed electric fields exposure elevates cytoplasmic  $\text{Ca}^{2+}$  concentration [22, 23, 24]. This pulsed electric field includes the low frequency domain. Cellular  $\text{Ca}^{2+}$  ( $[\text{Ca}^{2+}]$ ) overload has been suggested to be the final common pathway of cell death [25, 26]. As distinctions between necrosis and apoptosis have become better appreciated, elevated  $[\text{Ca}^{2+}]$  has retained its status as a key factor in necrosis, whereas a more variegated relationship has emerged between  $[\text{Ca}^{2+}]$  and apoptosis. As extracellular  $\text{Ca}^{2+}$  concentrations typically exceed  $[\text{Ca}^{2+}]$  by four orders of magnitude, a large increase in  $\text{Ca}^{2+}$  influx and  $[\text{Ca}^{2+}]$  inevitably accompanies the collapse of the plasma membrane that occurs early in necrosis.

For visualization of intracellular calcium, HeLa cells were loaded with calcium-sensitive fluorochrome Fluo-8 ( $\lambda_{\text{ex}} = 490 \text{ nm}$ ,  $\lambda_{\text{em}} = 514 \text{ nm}$ , ABD Bioquest) in Hanks' Balanced Salt Solutions (HBSS 084-08965; Wako) for 1 h at room temperature. After 1 h, the cells were placed on the on-slide electrodes. The electrodes separation is approximately 200  $\mu\text{m}$ . The electrodes were connected to the IBSEF application system via coaxial cable. Both bright field and fluorescent image were taken at every exposure to IBSEF.

### 3. Results

Figure 2 shows the morphology of cells exposed to IBSEFs with different frequency between 0.3 and 100 MHz. The cells exposed to 30 and 100 of IBSEF with 300 kHz are caused membrane defect on both

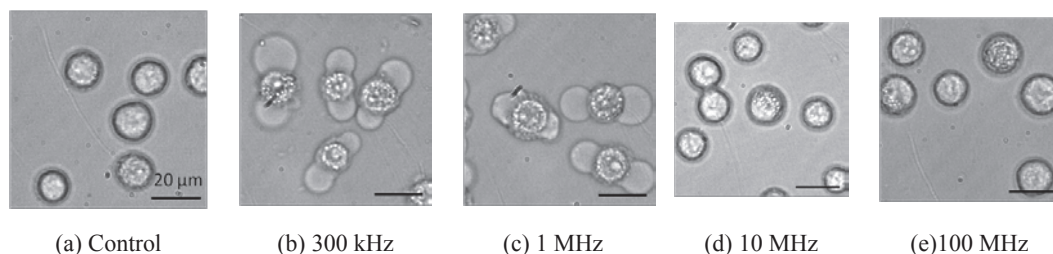


**Figure 2.** Morphology of HeLa cells exposed to repetitive 100 shots of IBSEF with 300 kV/m pulses. Scale bar is 20  $\mu\text{m}$  long. In more than 10 MHz, cell shape seems same as control. By contrast, in cases both of 300 kHz and 1 MHz IBSEF applied, we observed bubble-like blebs at both ends. Blebbing is initiated by extracellular triggers, causing localized destabilization or depolymerization of the cortical actin meshwork. Generally, Blebbing occurs scatteringly. So, it is reasonable that this phenomenon is directly caused by IBSEF.

sides and leaked cytoplasm. In case of 1 MHz, some cells exposed to 30 pulses does not cause membrane defect. Furthermore, the number of cells with leaks on the both sides somewhat decreases even 100 shots of IBSEFs. However, there is no effect on membrane appearance in cells exposed to IBSEF with frequency more than 10 MHz, even to 100 pulses.

Figure 3 shows the typical comet assay patterns for various values of the field strength and the frequency at 5 and 60 min after starting IBSEF application. Longer comet tail indicates more severe damage of the DNA. Experiments were repeated a minimum of 2, and 4 times on the conditions which DNA damage was observed. In Figures 3(a)-3(d), 100 kV/m, they have no tail and keep a shape of a cell. This means that the DNA is not damaged in all frequency range. Figures 3(e)-(h) shows results of 100 shots of IBSEF with the strength 200 kV/m and with various frequencies. In 300 kHz range, longer tail which fluoresces strongly can be observed. By contrast, in cases of more than 1 MHz, we cannot observe the long tail and DNA damage. On the conditions of the field strength of 300 kV/m, DNA damage is caused less than frequency of 1 MHz. However, the shape of comet differs a little. In condition of 300 kV/m, 1 MHz IBSEF (Fig 3(j)), some cell's DNA which has short tail are observed as well as condition of 200 kV/m, 300 kHz (Fig. 3(e)). In case of 300 kV/m IBSEF with frequency of 300 kHz, almost all tails are extended long. Furthermore, there are many cells which the back of the tail has swollen. DNA damage is not observed on the frequency of 10 MHz or more.

Figure 4 indicates comet patterns at 60 min after IBSEF exposure. In case of field strength of 100 kV/m, DNA damage was not observed. This result is the same as immediately after IBSEF exposure. The comet form of 200 kV/m, 300 kHz at 60 min after IBSEF exposure gathered comparatively. Tail length is also longer and clear than Fig. 3(e). In condition of 300 kV/m IBSEF with 300 kHz at 60 min after IBSEF application, the significant DNA damage is observed. Fragmented DNA hardly remains in a nuclear portion and moved to rightward. In 1 MHz,

the shape of comet looks being the same as that of 200 kV/m, 300 kHz. On the contrary, most influences are not seen on high frequency. This tendency is similar to the result of Fig. 3. The DNA damage is evaluated by the comet pattern using the following equation, which is known as reliable evaluation method, the Olive moment (OM) [12-15]. OM is given by the following equation;

$$OM = (C_{cell} - C_{nucleus}) \times \frac{DNA_{tail}}{DNA_{all}} \quad (1)$$

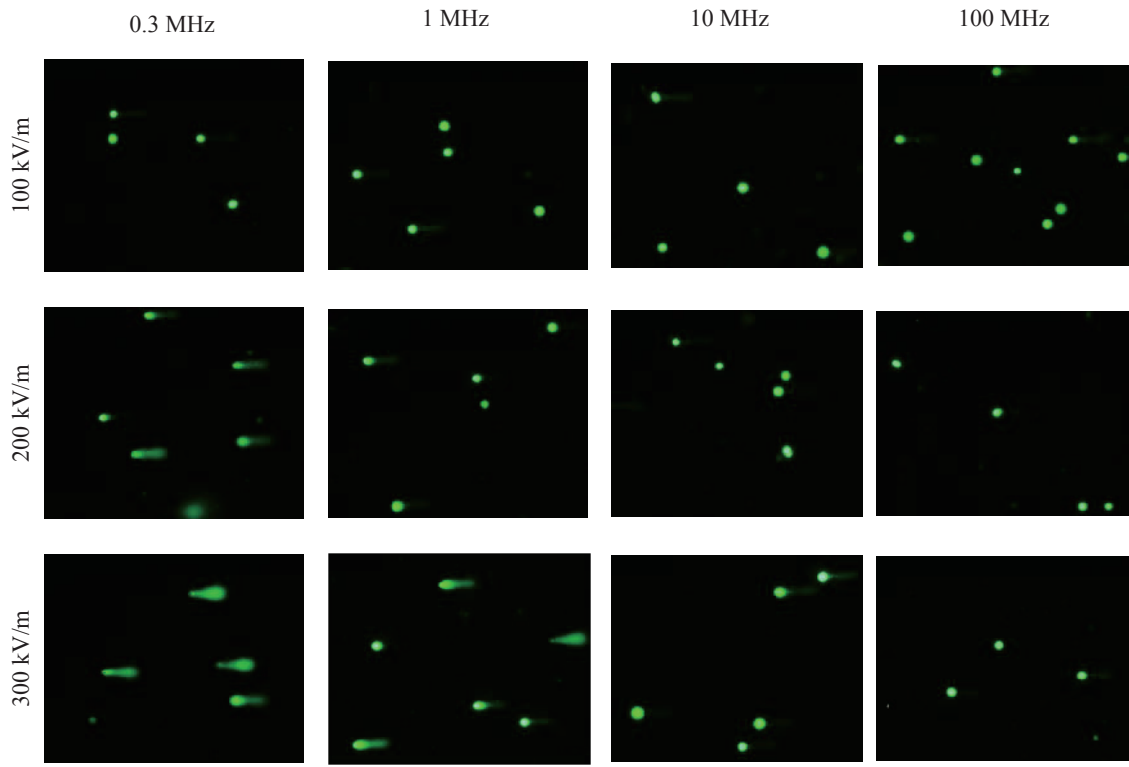
Where  $DNA_{tail}$  and  $DNA_{all}$  indicate the integrated values of fluorescence over the entire comet and over the tail, where  $C_{cell}$  and  $C_{nucleus}$  stand for the center positions of fluorescence in the entire comet and in the nucleus, respectively. The position and the fluorescent intensities were obtained using ImageJ, a public domain Java image processing program inspired from NIH Image. The OM value is expressed in pixels in this paper. Each bar represents the mean of normalized OM from 40-60 comets. OM which normalized the result in the condition of the field strength of 300 kV/m is shown in Fig. 5. The error bar on each data shows the standard deviation of the experimental scattering. There is a significant difference in the OM value between the negative control and the samples with 200 kV/m IBSEF of frequency of 300 kHz ( $P < 0.001$ ) as well as between the negative control and the samples with 300 kV/m IBSEF of frequency of 1 MHz ( $P < 0.001$ ). Furthermore, 300 kV/m IBSEF of 300 kHz does bigger damage to DNA ( $P < 0.0001$ ). These DNA damage is expanded with progress of time. The samples with the other conditions showed less effect, which failed the t test.

Figure 5 shows histograms of the cells against fluorescent intensity for PI. The PI after 100 IBSEF with strength of 300 kV/m application Sequentially from a left, the results of 5 minutes, 30 min and 60 minutes. The fluorescence is weak in the negative control. Uptake of PI did not occur in all frequency range for 30 minute of the beginning. After 60 min after IBSEF exposure, only in case of 300 kHz, more than half of the cells showed strong fluorescence, which were already dead or on the way of death. In

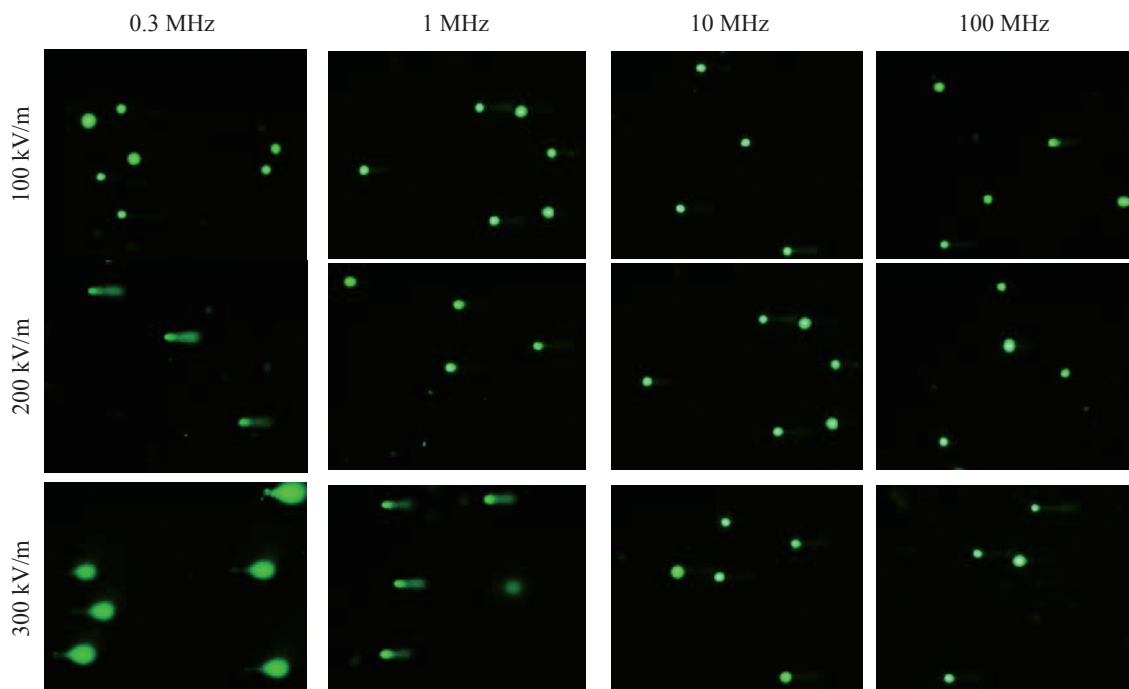
cases of 100 MHz, the cell applied IBSEF does not die.

Figure 6 indicates fluorescence of secondary

antibody-FITC meaning expression of active caspase-3. In negative control, there are many cells with low intensity indicating caspase-3 does not work. The



(a) 5 min after the exposure to IBSEF



(b) 60 min after the exposure to IBSEF

**Figure 3.** Comet patterns of HeLa cells at 5 min after the exposure to IBSEF with different field strength between 100 and 300 kV/m and with frequency between 0.3 and 100 MHz. The direction of the electric field in electrophoresis is leftward.

active caspase-3 does not appear also in frequency of 100 MHz. By contrast, in case of 300 kHz, the cells with high intensity slightly increase after IBSEF application. In addition, cells having high intensity of FITC gradually increase with progress of the time. Cells with the calcium-sensitive fluorochrome Fluo-8 in HBSS on the slides between 200  $\mu\text{m}$  gap electrodes. Figure 7 shows the cells before exposure to IBSEF, and immediately after exposure to IBSEF. After IBSEF application, green fluorescence increases in whole the cell at once in case of frequency less than 1 MHz. Number of cells with high fluorescence increases with increase of number of repetitive IBSEF. Moreover, the cell which carried out calcium burst once performs calcium burst continuously after that. However, this phenomenon

does not shift to calcium waves. In more than 10 MHz conditions, there are no increases of fluorescence for various field strength (maximum 300 kV/m) of multiple IBSEF.

#### 4. Discussion

We consider the electric field distribution over the cell with pore under an alternating external electric field to discuss the frequency dependence of the intracellular DNA damage. Figure 8 show the model for the numerical calculation of the electric field using a two dimensional finite element field analysis software (RFE2, TriComp, Field Precision). In Fig. 8, a 20  $\mu\text{m}$  diameter simplified spherical cell, which consists of plasma membrane ( $\epsilon_r = 54$ ,  $s = 6.0 \times 10^{-8}$  S/m) and nuclear membrane ( $\epsilon_r = 64$ ,  $s = 5.0 \times 10^{-5}$  S/m), cytoplasm ( $\epsilon_r = 70$ ,  $s = 1.6$  S/m) and nucleus ( $\epsilon_r = 120$ ,  $s = 0.95$  S/m), is suspended in a conductive solution between parallel electrodes [7,16,17]. The voltage of 12 V applied to the 40  $\mu\text{m}$  gap electrodes produces the average electric field of 300 kV/m that is equivalent to one used in the experiments. A pore diameter is 10 nm, which is large enough to be opened by IBSEF and should be affected by electric field distribution. The pore is in the position nearest to electrodes. Because of the limited spatial resolution, the plasma membrane thickness was set to be 30 nm, which is 6 times as thick as the actual value. Therefore, the permeability and conductivity were also set to be 6 times to compensate the capacitance and resistance of the plasma membrane. Finally, the calculated electric field for the plasma membrane was multiplied by 6. Figure 9 shows the equipotential line near the pore on the condition of 1 MHz, 300 kV/m. Although the strong electric fields are formed near the pore, the electric field does not permeate up to inside of cytoplasm, nuclear membrane and nucleus. It calculation indicates that 10 ns size pores does not influence the intracellular electric fields. From this reason, DNA damage can be caused by secondary effect of IBSEFs, not primary effect.

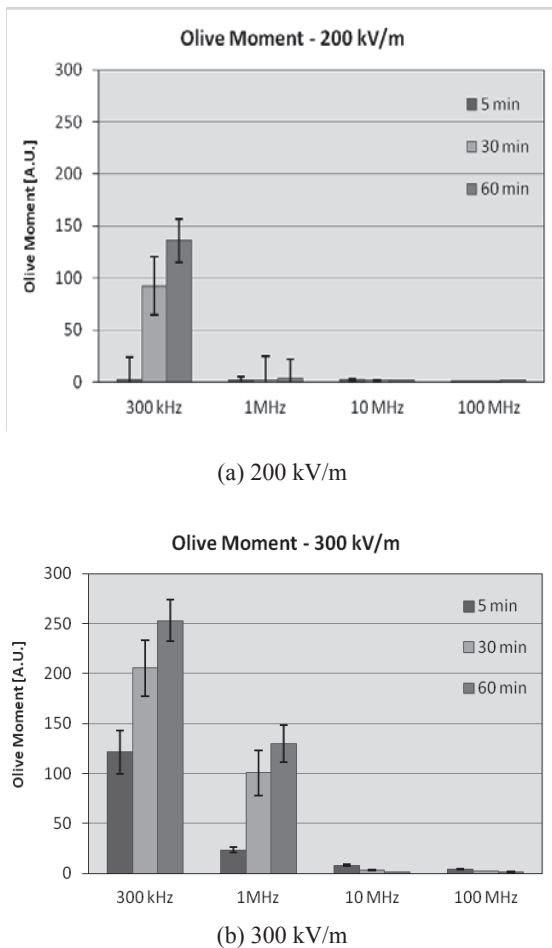


**Figure 4.** Evaluations of DNA fragment using Olive Moment method by the formula 1 (mean  $\pm$  S.D, n=3-4). DNA fragmentation is caused by 200 kV/m IBSEF with 300 kHz, and 300 kV/m IBSEF with frequency less than 1 MHz and expanded with progress of time.

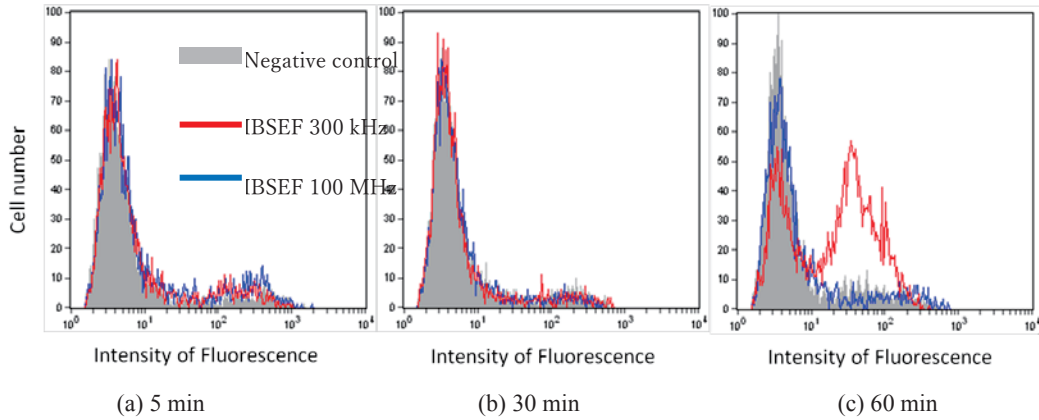


**Figure 5.** HeLa cells were stained PI at 5 min to 2 hours after the applying 300 kV/m, 100 shots of IBSEF with different frequencies. Vertical axis indicates the number of cell and horizontal axis indicates intensity of PI. The cell of 3000 per each parameter was used. Gray color indicates the negative control, red line and blue line are indicating the 300 kV/m IBSEF with 300 kHz, and 100 MHz, respectively. The cells are harvested and stained PI at (a) 5 minutes, (b) 30 minutes and (c) 60 minutes after IBSEF application.

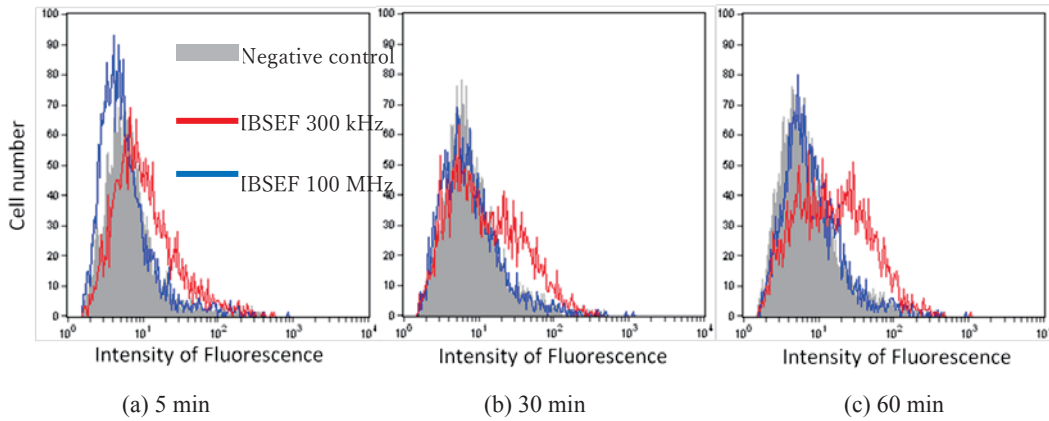


**Figure 6.** Activation of caspase 3 of the cell, which is applied IBSEF with different frequency. Gray color indicates the negative control, red line and blue line are indicating the 300 kV/m IBSEF with 300 kHz, and 100 MHz, respectively. Only in 300 kHz condition, the number of cells which fluorescence strongly are gradually increasing from 5min after IBSEF application.

Here we discuss about mechanism of this DNA fragmentation. Activation of caspase-3 cannot be observed in high frequency, and PI uptake can be observed as well in frequency of 300 kHz at 1 h after IBSEF application. Moreover, the number of cell with high fluorescence of Fluo-8, which indicates intracellular  $\text{Ca}^{2+}$  concentration, are also increasing with increasing frequency of IBSEF. This result means that IBSEF with low frequency is more effective for giving the stress which results to cell death to a HeLa cell. 300 kV/m IBSEF with low frequency might open the reversible pore which can close immediately at the end of IBSEF application.

$\text{Ca}^{2+}$  penetrate into the cytoplasm through the electroporated membrane, or ER stress by applying IBSEF caused releasing calcium stored in ER. In this stage, the cell was not stained by PI, however, DNA is damaged fatally from IBSEF. DNA fragmentation progresses with active caspase 3 as time passes for 1 h. As a result, the cell cause apoptosis-like death, then cell membrane cannot maintain a function and PI penetrates the inner cell and dyes the cell at 1 h after IBSEF application. According to electric fields calculation, DNA damage becomes large when the electric fields distributed on a cell membrane become strong. Furthermore, even if IBSEF is given in the

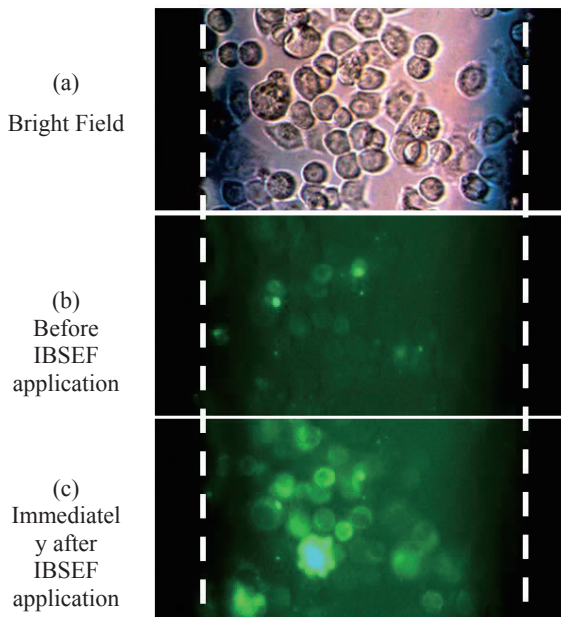


**Figure 7.** HeLa cells between 200  $\mu\text{m}$  gap electrodes on slide glass. Dash line indicates the edge of gold electrodes.

state where the pore is open, IBSEF does not permeate the inside of a cell. Judging from these experiments, it is reasonable to speculate that IBSEF with low frequency exposure of HeLa cells elevates the intracellular  $\text{Ca}^{2+}$  concentration through the membrane breakage and/or ER stress and increases endonuclease activity, resulting in the induction of DNA fragmentation and the subsequent apoptosis.

## 5. Conclusions

We discuss the proliferation activity of HeLa cells exposed to non-thermal, narrow band, intense burst AC electric fields. Our experiment shows that the DNA breakage depends on the field strength and the frequency band of the IBSEF. By application of IBSEF, Distribution the high electric field of cell membrane causes activation caspase-3 and fragmentation of DNA. At 1 h after IBSEF application, the cell cannot maintain the function of membrane and die. DNA fragmentation is larger on low frequency. This frequency band could affect to endoplasmic reticulum. ER stress results in DNA fragmentation though  $\text{Ca}^{2+}$  release from ER or  $\text{Ca}^{2+}$  influx from suspension medium, and activation of caspase-3.

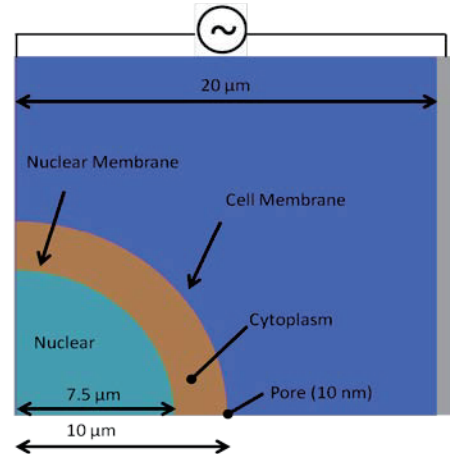


**Figure 8.** Calculation model. A simplified cell with 10 nm pore suspended in a conductive solution between parallel electrodes where an alternating current voltage of 12 V is applied.

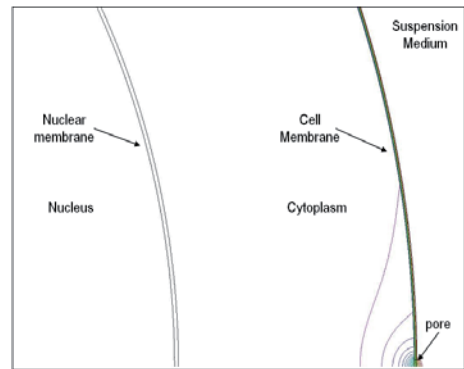


**Figure 9.** The equipotential line near the pore on the condition of 1 MHz, 300 kV/m. Although strong electric fields distributed on only near the pore, it does not arrive to the back inside of a cell.

## References

- [1] K.H. Schoenbach, B. Hargrave, R.P. Joshi, J.F. Kolb, R. Nuccitelli, C. Osgood, A. Pakhomov, M. Stacey, R.J. Swanson, J.A. White, S. Xiao, J. Zhang, "Bioelectric Effects of Intense Nanosecond Pulses", IEEE Trans. Dielectr.Electr. Insulat. Vol. 14, No. 5, pp. 1088-1109, 2007.
- [2] K.H. Schoenbach, S.J. Beebe, E.S. Buescher, "Intracellular Effect of Ultrashort Electrical Pulses", Bioelectromagnetics Vol. 22, 440-448, 2001.
- [3] E. Neumann, K. Rosenheck, "Permeability Changes Induced by Electrical Impulses in Vesicular Membranes", J. Membrane Biol. Vol. 10, pp. 279-290, 1972.
- [4] R. Nuccitelli, U. Pliquett, X. Chen, W. Ford, R.J. Swanson, S.J. Beebe, J.F. Kolb, K.H. Schoenbach, "Nanosecond Pulsed Electric Fields Cause Melanomas to Self-destruct", Biochem. Biophys. Res. Comm. Vol. 343, pp. 351-360, 2006.

- [5] J. Zhang, P.F. Blackmore, B.Y. Hargrave, S. Xiao, S.J. Beebe, K.H. Schoenbach, "Nanosecond pulse electric field (nanopulse): A novel non-ligand agonist for platelet activation", *Arch. Biochem. Biophys.* Vol. 471, pp. 240-248, 2008.
- [6] N. Nomura, M. Yano, S. Katsuki, H. Akiyama, K. Abe, S-I. Abe, "Intracellular DNA Damage Induced by Non-thermal, Intense Narrowband Electric Fields", *IEEE Trans. Dielectr. Electr. Insulat.* Vol. 16, No. 5, pp. 1288-1293, 2009
- [7] S. Katsuki, N. Nomura, H. Koga, H. Akiyama, I. Uchida, S-I. Abe, "Biological Effects of Narrow Band Pulsed Electric Fields", *IEEE Trans. Dielectr. Electr. Insulat.* Vol. 14 pp. 663-668, 2007.
- [8] J. Glamann, A.J. Hansen, "Dynamic detection of natural killer cell-mediated cytotoxicity and cell adhesion by electrical impedance measurements", *Assay and Drug Development Technologies* Vol. 4, No. 5, pp.555-563, 2006
- [9] D. Anderson, M.M. Dobrzynska, N. Basaran, A. Basaran, T.W. Yu, "Flavonoids modulate comet assay responses to food mutagens in human lymphocytes and sperm", *Mutat. Res.* Vol. 402, pp.269-277, 1998
- [10] E.T. Donnelly, N. McClure, S.E. Lewis, "The effect of ascorbate and alpha-tocopherol supplementation in vitro on DNA integrity and hydrogen peroxide-induced DNA damage in human spermatozoa", *Mutagenesis* Vol. 14, pp. 505-512, 1999
- [11] Reiner U. Jänicke, Michael L. Sprengart, Mas R. Wati and Alan G. Porter: "Caspase-3 Is Required for DNA Fragmentation and Morphological Changes Associated with Apoptosis", *J. Biological Chemistry*, Vol. 273, No. 16, pp. 9357-9360, 1998
- [12] S. Kothakota, T. Azuma, C. Reinhard, A. Klippel, J. Tang, K. Chu, T.J. McGarry, M.W. Kirschner, K. Koths, D.J. Kwiatkowski, L.T. Williams, "Caspase-3-Generated Fragment of Gelsolin: Effector of Morphological Change in Apoptosis", *Science* Vol. 278, No. 5336, pp. 294-298, 1997
- [13] T.S. Kumaravel, A.N. Jha, "Reliable Comet Assay measurements for detecting DNA Damage induced by ionizing radiation and chemicals", *Mutat. Res.* Vol. 605, pp 7-16, 2006
- [14] A.R. Collins, A.A. Oscoz, G. Brunborg, I. Gaivano, L. Giovannelli, M. Kruszewski, C.C. Smith, R. Stetina, "Review; The Comet assay: topical issues" *Mutagenesis* Vol. 23, No. 3, pp. 143-151, 2008
- [15] P.L. Olive, J.P. Banáth, R.E. Durand, "Heterogeneity in radiation-induced DNA damage and repair in tumor and normal cells measured using the comet assay", *Radiat. Res.* Vol. 122, pp.86-94, 1990
- [16] P.L. Olive, D. Wlodek, J.P. Banáth, "DNA double-strand breaks measured in individual cells subjected to gel electrophoresis", *Cancer Res.* Vol. 51, pp.4671-4676, 1991
- [17] I. Ermolina, Y. Polevaya, Y. Feldman, B. Z. Ginzburg, M. Schlesinger, "Study of normal and malignant white blood cells by time domain dielectric spectroscopy", *IEEE Trans. Dielectr. Electr. Insulat.* Vol. 8, No. 2, pp. 253-261, 2001.
- [18] D. Malleo, J.T. Nevill, L.P. Lee, H. Morgan, "Continuous differential impedance spectroscopy of single cells", *Microfluidics Nanofluidics* Vol. 9, pp.191-198, 2010
- [19] M.J. Arends, R.G. Morris, A.H. Wyllie, "Apoptosis: the role of the endonuclease", *Am. J Pathol.* Vol. 136, pp. 593-608, 1990
- [20] J.J. Cohen, R.C. Duke, "Glucocorticoid activation of a calcium-dependent endonuclease in thymocyte nuclei leads to cell death", *J. Immunol.* Vol. 132, pp. 38-42, 1984
- [21] F. Yanagisawa-Shiota, H. Sakagami, N. Kuribayashi, M. Iida, T. Sakagami, M. Takeda, "Endonuclease activity and induction of DNA fragmentation in human myelogenous leukemic cell lines", *Anticancer Res.* Vol. 15, pp. 259-265, 1995.
- [22] Q. Hu, J. Chang, L. Tao, G. Yan, M. Xie, Z. Wang "Endoplasmic Reticulum Mediated Necrosis-like Apoptosis of HeLa Cells Induced by Ca<sup>2+</sup> Oscillation", *J. Biochem. Molecul. Biol.* Vol. 38, No. 6, pp. 709-716, 2005
- [23] V.S. Shankar, B.I. Simon, C.M.R. Bax, M. Pazianas, B.S. Moonga, O.A. Adebajo, M. Zaidi, "Effect of electromagnetic stimulation on the functional responsiveness of isolated rat osteoclasts", *J. Cell Physiol.* Vol. 176, pp.537-544, 1998
- [24] P.T. Vernier, Y. Sun, L. Marcu, S. Salemi, C.M. Craft, M.A. Gundersen, "Calcium bursts induced by nanosecond electric pulses", *Biochem. Biophys. Res. Comm.* Vol. 310, pp. 286-295, 2003
- [25] F.A. Schanne, A.B. Kane, E.E. Young, J.L. Farber, "Calcium dependence of toxic cell death: a final common pathway", *Science*, Vol 206, pp.700-702, 1979
- [26] P. Nicotera, S. Orrenius, "The role of calcium in apoptosis", *Cell Calcium*, Vol. 23, pp.173-180, 1998

# Enhance the Efficiency of Pulsed Electric Fields Sterilization for Liquid Foods

Taiga Kajiwara, Kazuma Baba and Sunao Katsuki\*

*Graduate School of Science and Technology, Kumamoto University*

*\*Institute of Pulsed Power Science, Kumamoto University*

## ABSTRACT

This paper describes bacterial decontamination of liquid foods using intense pulsed electric fields (PEF) combined with a moderate thermal treatment (<55 °C), where most of ingredients remain unchanged. We have developed a one-way flow treatment system including a water-cooled parallel plane electrode and heat exchangers to control the liquid temperature. A 600 ns-long mono-polar rectangular pulse generated by a Blumlein type pulse-forming-network was delivered repetitively to the electrode. Saline solution including *Enterobacter Aerogenes* (*E. Aerogenes*) was exposed to tens of electrical pulses before the thermal treatment. Our experiment shows the additional thermal treatment strengthens the killing effect of the PEF treatment. The PEF treatment (50 kV/cm, 35 shots) at the room temperature reduced only 2-log cycles of bacterial. The additional thermal treatment enhances the killing effect, and the additional killing effect linearly depends on the thermal treatment temperature within the experimental range between 25 °C and 55 °C, whereas *E. Aerogenes* survives the thermal treatment at 55 °C. 7-log cycles of bacterial reduction was achieved in this experiment. The bacterial death is considered to be caused by the heat influx due to the PEF-induced membrane disintegration.

## Keywords

liquid sterilization, pulsed electric field, thermal energy, Blumlein generator.

## 1. Introduction

One third of those living in industrialized countries may be affected by food borne illnesses each year [1] occurring in liquid food products such as liquid whole eggs, fruit juice, and milk. Thermal treatment and chemical substances have been used for bacteriostasis, bacteria elimination, and sterilization treatment method for food [2]. Temperatures exceeding 60 °C are required for conventional thermal treatment, whereas most proteins are denatured at temperatures over 57 °C [3]; thus, a low-temperature sterilization method has long been sought. Thermal treatment combined with chemical additives are also utilized as a low-temperature treatment; however, the use of chemical compounds is unpopular with consumers.

Low-temperature sterilization technologies for liquids are desirable due to efficiency, efficacy, and lack of influence on taste. Several methods such as UV, electron beams, high pressure, and pulse electric fields have long been studied, with some implemented in the food industry. While UV sterilization technology is appropriate for surface sterilization of food or medical instruments and has been implemented in some countries, its liquid permeability is insufficiently deep for practical use on liquid foods [4]. Electron beam sterilization is appropriate for surface sterilization and can control penetration power by changing accelerating voltage such as the use of soft electrons, or electrons with energies of 300 keV or lower, which uses low energy for sterilization [5]. However, creating penetration

power sufficient to sterilize liquid requires a large amount of power with, for example, 10 MeV required to affect to a depth of 5 cm in liquid [6]; large-sized accelerators are required to provide such high energy to an electron beam. Most high pressure gas sterilization systems use pressures exceeding 300 MPa, vastly increasing equipment costs and scale. Also, high-pressure sterilization utilizes batch processing, leading to low efficiency [7]. To avoid these problems with efficiency and efficacy, PEF (pulsed electric field) sterilization has been proposed. PEF technology is simple and low-cost; however, its sterilization effects remain insufficient for practical use.

Hamilton and Sale reported the first experiment of liquid sterilization using PEF in 1967 [8-10], and many experiments have since been conducted. However, as energy requirements for PEF sterilization remain large, PEF sterilization technology has yet to be put into practical use in the food industry [11]. Attempts have been made to increase sterilization strength of PEF to lower its energy requirements, including combinations with additional technologies such as high pressure [12], chemical additives [13, 14], and thermal energy [15, 16]. For example, Pataro et al reported that PEF treatment under pressurized conditions reduced bacterial population by 2.4-log cycles [17], and use of an emulsifier and ethylenediaminetetraacetic acid (EDTA) as chelating agents of metal ions was found to significantly enhance the sterilization effect of PEF treatment [11]. Of significance to this study, in 2007, Amiali et al reported that the combination of thermal and PEF treatments killed bacteria synergistically [18]. Their study demonstrated that PEF treatment (210  $\mu$ s, 30 kV/cm) at 40 °C resulted in a reduction of 4.8-log cycles, whereas PEF that at 20 °C was only 0.8-log cycles. The greater efficacy of PEF combined with thermal treatment may be that a number of bacteria survive PEF exposure in a damaged condition and were thus vulnerable to subsequent, relatively low-level heat. Although their experiment did not result in sterilization strength sufficient for practical use in the food industry, their results

promise stronger sterilization effects by optimization of PEF and thermal treatments.

This paper describes sterilization effects of intense pulsed electric field (iPEF) combined with subsequent thermal treatment. Our study used a 530 ns-long, 50 kV/cm rectangular pulse to cause significant damage to the bacterial membrane. Thermal treatment temperature was ranged up to 55 °C, a level sufficient to expose bacteria to thermal stress but insufficient to denature the food ingredient proteins in the liquid food sterilized. We used *Enterobacter aerogenes* as target bacteria and Carboxymethyl cellulose solution as a bacterial suspension to simulate liquid whole egg. The bacterial suspension was treated in a single-pass continuous flow system including the iPEF exposure chamber and pre- and post-treatment heaters. Finally, we discuss mechanisms of the enhanced killing effect owing to exposure to moderate temperature after the iPEF treatment on the basis of investigation of iPEF-induced membrane damage and recovery from this damage.

## 2. Experimental Setup

### 2.1 Bacteria and suspending medium

*Enterobacter aerogenes* (ATCC 13048) were used as target bacteria to evaluate sterilization strength. This bacterium is a Gram-negative, rod-shaped microorganism of the Enterobacteriaceae family. Carboxymethyl cellulose (CMC) solution containing 0.25% sodium chloride and 1.5% CMC was used as bacterial suspension medium. Viscosity and electrical conductivity of the synthetic solution were 15.5 mPas and 6.7 mS/cm, respectively, both of which are comparable to those of liquid whole egg. Bacteria were suspended in a culture medium containing casein-peptone 5.0 g/L, yeast extract 2.5 g/L, glucose 1.0 g/L and agar 14.0 g/L and incubated at 32 °C for 24 hours before they were used in the test. The bacterium concentration of the CMC solution for the test was  $10^7$  CFU/mL.

### 2.2 IPEF exposure chamber and treatment system

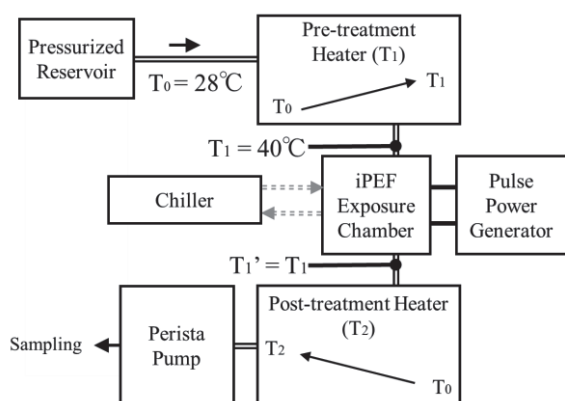


Fig. 1 Block diagram of flow sterilization system

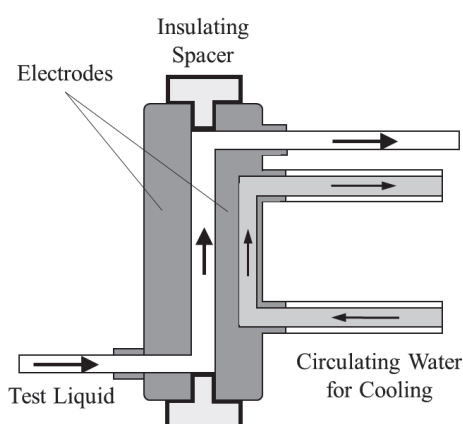


Fig. 2 Detail of the iPEF exposure chamber form cross sectional view.

Figure 1 shows a block diagram of the continuous flow single pass treatment system. The bacterial suspension medium flowed from the reservoir to the pre-treatment heater, where it was warmed up to 40 °C for 2 minutes. The medium was exposed to tens of iPEF pulses while passing through the iPEF exposure chamber before flowing into the post-treatment heater, where it was heated to a prescribed temperature within 2 minutes and maintained there for an additional 2 minutes. Subsequently, the suspension was rapidly cooled to 4 °C for sampling after passing through a Perista pump (AC2120, ATTO) to control the system flow rate. The system was pressurized at 0.3 MPa to prevent electrical breakdown at the iPEF exposure chamber. The pulse repetition frequency was fixed at 1 Hz; pulse number was controlled by varying the liquid flow rate between 1.37 and 3.20

mL/min. A laminar flow was expected in the experimental condition. The temperatures in the pre- and the post-treatment heaters defined as  $T_1$  and  $T_2$  were controlled independently with accuracy of 1 °C. In this study,  $T_1$  was fixed at 40 °C and  $T_2$  was variously set at 28, 45, 50 or 55 °C. Figure 2 shows a section view of the iPEF exposure chamber, consisting of 4 mm-spaced parallel stainless steel electrodes (SUS316) and a polyethersulfone spacer. Chamber dimensions were 6 mm in width and 35 mm in height, forming a capacity of 0.8 ml. Resistance of the exposure chamber with the flowing CMC solution was approximately 20  $\Omega$ . Temperatures of the suspension at the inlet ( $T_1$ ) and outlet ( $T_1'$ ) of the exposure chamber were monitored using fiber-optic thermometers (FL-2000, Anritsu). Electrodes were directly cooled by a circulating system for  $T_1'$  to be equal to  $T_1$  in all pulse conditions.

### 2.3 Pulse generator

Figure 3 shows our 6-staged Blumlein-type pulse-forming network (BPFN), which was designed and built to generate submicrosecond-long mono-polar pulse to the 20  $\Omega$  load. The inductor  $L$  and capacitor  $C$  were 300 nH and 2.6 nF, respectively, producing an output impedance of 21  $\Omega$  and pulse duration of 530 ns. Longer pulse duration is preferred to give a stronger stress to the bacterial membrane, while longer pulse tends to cause the liquid breakdown for strong fields in the level of 50 kV/cm. The duration of 530 ns is appropriate to apply the strong field to the bacterial suspension stably. The BPFN was powered by a pulse-charging unit through transformer TR. A pressurized spark gap switch SW closed automatically when the BPFN was fully charged. A saturable inductor SL with a toroidal FINEMET core (FT-3H, Hitachi Metals) functioned as a low impedance while the capacitors were charged, becoming high impedance when SW was closed. Figure 4 shows a waveform of the voltage pulse applied to the iPEF exposure chamber detected using a voltage probe (P6015, Tektronix). The current waveform, detected using a current monitor (Model 110, Pearson), was identical to the voltage. In this study, the voltage amplitude was fixed at 20 kV,

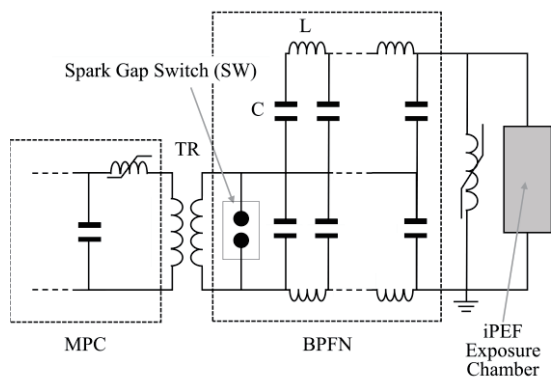


Fig. 3 Diagrams the circuit of pulsed power generator based on Blumlein-type pulse-forming network (BPFN).

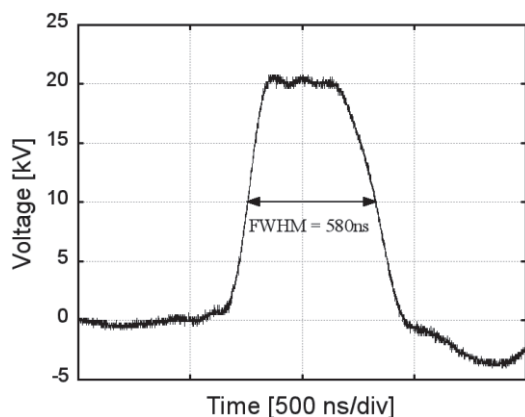


Fig. 4 Waveform of the pulse voltage applied to the iPEF exposure chamber.

corresponding to the field strength of 50 kV/cm. Voltage amplitude deviation for the repetitive operation was 3%. Rise and fall times were 130 and 200 ns, respectively. The dissipation energy per pulse was 11 J, 80% of which contributed to the effective electric field exceeding 90% of the maximum.

#### 2.4 Evaluation of sterilization effect

Treatment sterilization strength was evaluated by colony counting method. Bacterial suspension was appropriately diluted by phosphate buffered saline (PBS) before being smeared onto nutritious agar media to allow for surviving bacteria to form colonies. Two types of culture agar media were used: one standard, the other with basically the same content as standard but additionally containing 5% sodium chloride. After incubation at 32 °C for 24 hours,

colony forming units (CFU) on the agar were counted.

### 3. Results

Figure 5 shows sterilization effects as a function of pulse number and temperature of post-treatment heater  $T_2$ . All experiments were performed more than three times on different days. Error bars in the figures indicate standard deviation. The circle indicates the result of thermal treatment at  $T_1=55$  °C without iPEF exposure, indicating that sole thermal treatment only slightly reduced the bacterial population (0.1-log cycles); this compares with a reduction of 2.1-log cycles after exposure to 35 pulses of 50 kV/cm without thermal treatment. When thermal treatment was subsequently added to the iPEF exposure, sterilization strength increased significantly. The strength increased both with an increase in pulse number  $N$  and temperature in the subsequent thermal treatment  $T_2$ . At  $T_2=55$  °C, sterilization strength linearly increased with pulse number, whereas treatment without thermal treatment seems to saturate against pulse number under the same tendency most experiments have previously reported [15, 19, 20]. A sterilization strength of 6.6-log cycles was achieved at the condition of  $T_2=55$  and  $N=35$ . In this experiment, energy expenditure for the sterilization strength exceeding 6.6 was 340 kJ/L. If a 10 kW pulse generator were used for treatment, the processing rate would be approximately 100 L/hour, still insufficient by a factor of 10 for practical use in the food industry.

Figure 6 shows dependence of sterilization strength on post-treatment temperature,  $T_2$ , for pulse numbers of 15, 25 and 35. As an overall tendency, bacteria exposed to a larger number of pulses are seen to be more sensitive to temperature. The sterilization effect is strengthened by increasing temperature in the range over a certain value, which we define as threshold temperature for heat resistance  $T_{hr}$ , whereas it does not depend on the temperature in the range less than  $T_{hr}$ . Approximate respective values of  $T_{hr}$  for  $N=15, 25$  and  $35$ , which can be deduced

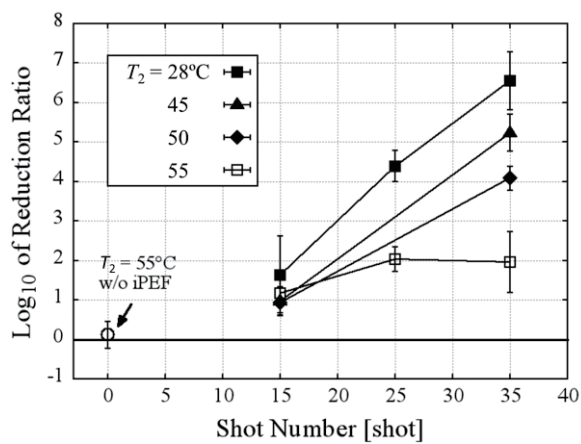


Fig. 5 Effect of shot number and temperature of post-treatment exchanger ( $T_2$ ) on inactivation of *Enterobacter aerogenes* by iPEF and thermal in CMC solution.

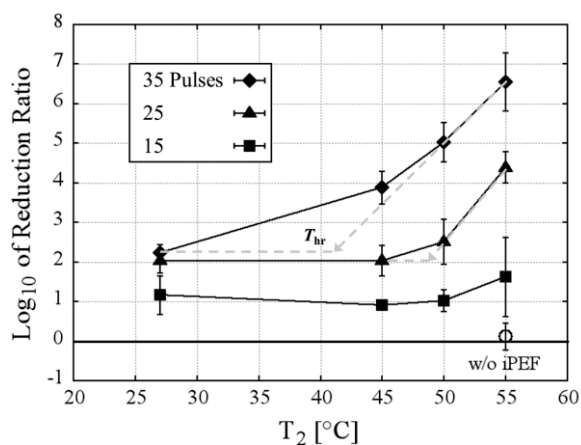


Fig. 6 Effect of temperature of post-treatment exchanger ( $T_2$ ) and shot number on inactivation of *Enterobacter aerogenes* by iPEF and thermal in CMC solution.

from extensions of the curve in Figure 6 (shown in gray), are 50, 48 and 40 °C. These values are presumably lowered by an increase in pulse number.

#### 4. Discussion

We discuss why iPEF treatment in the absence of thermal treatment is relatively ineffective and discuss how subsequent thermal treatment enhances the sterilization effect of iPEF exposure. Our experiment shows exposure to iPEF without thermal treatment killed 99% of bacteria, with 1% surviving. According

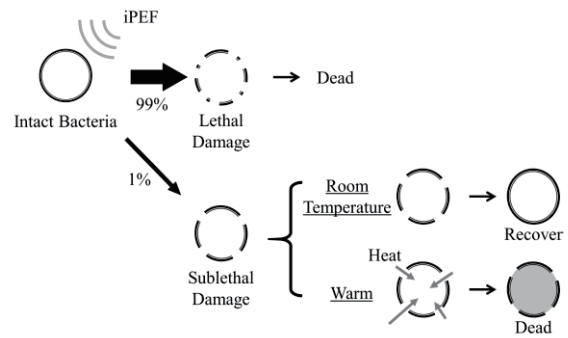


Fig. 7 Hypothesis of the mechanism of synergistic effect of the additional thermal energy to the iPEF exposure.

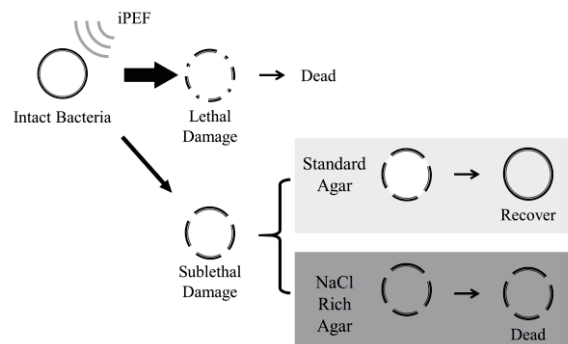


Fig. 8 Experimental scheme to investigate membrane injury caused by iPEF pulses and the self-recovery from the injury, by means of culturing iPEF exposed bacteria in two different agar media, standard and sodium chloride rich ones.

to previous studies [11, 21-24], exposure to an intense pulsed electric field causes defects in the function and structure of the cell membrane, leading to an increase in permeability. While this phenomenon is temporary when the damage is relatively small, when large, it is irreversibly fatal to the cell. Generally, a cell membrane works as a dielectric film by interrupting a current flow under an external electric field, leading to the enhancement of electric field on the membrane. Exposure of bacteria to a pulsed field of 50 kV/cm is expected to produce a voltage of 5 V across the cell membrane. The field strength on a membrane whose thickness is 6-8 nm exceeds 3 MV/cm, which is sufficiently large to damage the membrane structure due to electrical

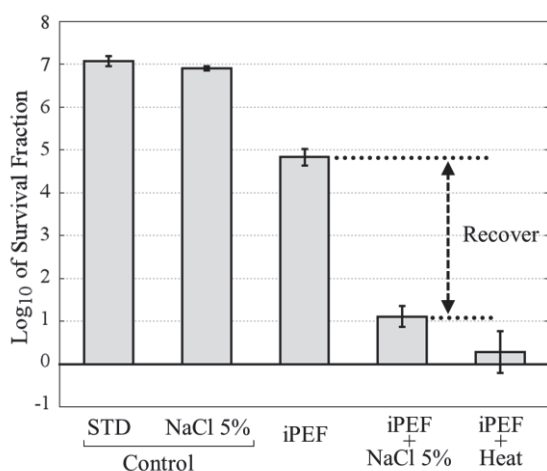


Fig. 9 The result of measuring the sublethal injury bacillus and comparing the number of CFU: sham (STD); iPEF treatment only and cultured on non-selective medium (iPEF); iPEF treatment only and cultured on selective medium (iPEF+NaCl 5%); iPEF treatment combined 55 °C of thermal effect (iPEF+Heat). All data show the average of more than three trials.

and/or mechanical breakdown [25]. These phenomena called electroporation. Electroporation caused by strong electric fields is well-known to physically damage the cell membrane, resulting in an increase in permeability for substances including ions. Bacterial cell membranes shield the interior from surrounding conditions to maintain appropriate conditions for optimal physiological activity. On the basis of our experimental a result as shown in Figure 5, we have reached the following hypothesis as illustrated in Figure 7. First, self-recovery of the damaged membrane suppresses the sterilization effect of iPEF. The exposure to tens of iPEF pulses is likely to injure all bacteria to some extent. Bacteria with relatively minor membrane damage were reorganized without thermal treatment to resume their physiological activity, whereas bacteria with severe membrane damage died. The recovery of these bacteria indicates that iPEF treatment in the absence of thermal treatment is relatively ineffective. Secondly, subsequent thermal energy interferes with reorganization of the damaged membrane and

penetrates into the interior to raise intracellular temperature, resulting in deactivation of physiological activity. Membranes physically damaged by iPEF exposure are likely to be permeable not only by ions but also by heat. In summary, ineffectiveness of iPEF treatment at the room temperature is caused by bacterial recovery, and the effectiveness of combined treatment is caused by bacteria whose damage due to exposure to iPEF made them vulnerable to subsequent thermal treatment.

In order to demonstrate our hypothesis, we carried out additional experiments as shown in Figure 8 using two kinds of nutrient agar media, a standard one and one including 5% sodium chloride which in this paper is called NaCl rich agar. It is known that sodium chloride hinders the repair of injured membranes, which is why injured bacteria do not form colonies in NaCl rich agar [18, 26]. Therefore, comparing colonies formed in the standard and in the NaCl rich agar media allowed us to obtain a portion of bacteria which had recovered from membrane injury caused by iPEF exposure without thermal treatment. According to our hypothesis, the number of colonies formed in the NaCl rich agar is expected to be the same as the result of the combination of iPEF and the subsequent thermal treatment. Figure 9 shows survival fractions of bacteria exposed to iPEF and subsequently cultured in a NaCl rich medium along with those exposed to iPEF and to both iPEF and subsequent thermal energy and then cultured in a standard medium. Toxicity of the culture medium including 5% NaCl on intact bacteria is negligible. For the bacteria exposed to iPEF without thermal treatment, the number of surviving bacteria cultured in a NaCl rich medium is much less than that in a standard medium and the same level as that for the combination of iPEF and the subsequent thermal treatments. This result indicates iPEF treatment without thermal treatment can damage almost all (approximately 9,999,990/10,000,000) bacterial membrane. However, most of the membrane damaged bacteria (approximately 99,990/9,999,990) can self-recover and survive. On the other hand, iPEF treatment followed by thermal treatment can kill

bacteria with membrane damage, indicated by the fact that the number of surviving bacteria cultured in a NaCl rich medium is the same level as iPEF treatment at high temperature. This result agrees with our hypothesis that most bacteria exposed to iPEF without thermal treatment recovered from membrane damage, and that effectiveness of combined treatment is caused by bacteria whose damage due to exposure to iPEF left them vulnerable to subsequent thermal treatment.

Regarding heat vulnerability of bacterial membranes exposed to pulses, a reasonable hypothesis is that a greater pulse number is likely to cause more severe damage to the membrane, resulting in vulnerability to subsequent thermal treatment. This hypothesis is supported by experimental results: as shown in Figure 6, a greater pulse number not only causes bacteria to be more sensitive to subsequent thermal treatment but also lowers the bacteria heat resistance capability threshold temperature.

## 5. Conclusions

This paper shows a synergistic effect of intense pulsed electric field and subsequent thermal exposure at moderate temperatures of up to 55 °C on sterilization of *Enterobacter aerogenes* in a synthetic suspending medium. The experiment demonstrated a sterilization strength of 6.6-log cycles achieved under conditions of 35 iPEF pulses and temperature of 55 °C. Our experiment results support our hypothesis that the relative ineffectiveness of iPEF treatment without thermal treatment is due to recovery of the bacterial membrane, while subsequent thermal treatment exploits this vulnerability.

## References

- [1] E. SCOTT, "Food safety and foodborne disease in 21st century homes", *Can J. Infect. Dis.*, **14**, pp.277-280 (2003).
- [2] L.W. DALTON, "Food Preservatives", *Chemical and Eng. News*, **80**, 45, p.40 (2002).
- [3] M.H. SAMIMI et al., "Flow behaviour of liquid whole egg during thermal treatments", *J. Food Sci.*, **49**, pp. 132-136 (1984).
- [6] T. BINTSIS et al., "Existing and potential applications of ultraviolet light in the food industry – a critical review", *J. Sci. Food Agric.*, **80**, pp. 637-645 (2000).
- [7] T. HAYASHI, et al., "Sterilization of foods with low-energy electrons ("soft-electrons")", *Radiat. Phys. Chem.*, **52**, pp. 73-76 (1998).
- [8] J.T. ALLEN et al., "A fully integrated 10 MeV electron beam sterilization system", *Radiat. Phys. Chem.*, **46**, 4-6, pp. 457-460 (1995).
- [9] J.P.P.M. SMELT, "Recent advances in the microbiology of high pressure processing", *Trends in Food Sci. Tech.*, **9**, pp. 152-158 (1998).
- [10] A.J.H. SALE et al., "Effects of high electric fields on microorganisms: I. Killing of bacteria and yeasts", *Biochim. Biophys. Acta*, **148**, 3, pp. 781-788 (1967).
- [11] W.A. HAMILTON et al., "Effects of high electric fields on microorganisms: II. Mechanism of action of the lethal effect", *Biochim. Biophys. Acta*, **148**, 3, pp. 789-800 (1967).
- [12] A.J.H. SALE et al., "Effects of high electric fields on micro-organisms: III. Lysis of erythrocytes and protoplasts", *Biochim. Biophys. Acta*, **163**, 1, pp. 37-43 (1968).
- [13] S. MONFORT et al., "Inactivation of *Salmonella* spp. in liquid whole egg using pulsed electric fields, heat, and additives", *Food Microbiol.*, **30**, pp. 393-399 (2012).
- [14] E. HUANG et al., "Inactivation of *Salmonella* enteritidis in Liquid Whole Egg using Combination Treatments of Pulsed Electric Field, High Pressure and Ultrasound", *Biosystems Eng.*, **94**, 3, pp. 403-413 (2006).
- [15] N. DUTREUX et al., "Effects of combined exposure of *Micrococcus luteus* to nisin and pulsed electric fields", *Int'l. J. Food Microbiol.*, **60**, pp. 147-152 (2000).
- [16] S. MONFORT et al., "Physicochemical and functional properties of liquid whole egg treated by the application of Pulsed Electric Fields followed by heat in the presence of triethyl

- citrate", *Food Res. Int'l.*, **48**, pp. 484-490 (2012).
- [17] M.I. BAZHAL et al., "Inactivation of Escherichia coli O157:H7 in liquid whole egg using combined pulsed electric field and thermal treatments", *LWT-Food Sci. Technol.*, **39**, pp. 419-425 (2006).
- [18] S. MONFORT et al., "Design of a combined process for the inactivation of Salmonella Enteritidis in liquid whole egg at 55°C", *Int'l. J. Food Microbiol.*, **145**, pp. 476-482 (2011).
- [19] G. PATARO et al., "Microbial inactivation of E. coli cells by a combined PEF-HPCD treatment in a continuous flow system", *Innovative Food Sci. Emerging Tech.*, **22**, pp. 102-109 (2014).
- [20] M. AMIALI et al., "Synergistic effect of temperature and pulsed electric field on inactivation of Escherichia coli O157:H7 and Salmonella enteritidis in liquid egg yolk", *J. Food Eng.*, **79**, pp. 689-694 (2007).
- [21] S. MONFORT et al., "Inactivation of Salmonella Typhimurium and Staphylococcus aureus by pulsed electric fields in liquid whole egg", *Innovative Food Sci. and Emerging Tech.*, **11**, pp. 306-313 (2010).
- [22] G. CEBRIAN et al., "Resistance to stresses of relevance to food preservation", *J. of Applied Microbio.*, **107**, pp. 187-196 (2009).
- [23] A. ANGERSBACH et al., "Effects of pulsed electric fields on cell membranes in real food systems", *Innovative Food Sci. Emerging Tech.*, **1**, pp. 135-149 (2000).
- [24] K.H. SCHOENBACH et al., "Bioelectrics - new applications for pulsed power technology", *IEEE Trans. Plasma Sci.*, **30**, 1, pp. 293-300 (2002).
- [25] U. ZIMMERMANN et al., "Dielectric Breakdown of Cell Membranes", *Biophys. J.*, **14**, 11, pp. 881-899 (1974).
- [26] U. ZIMMERMANN, "Electric field-mediated fusion and related electrical phenomena", *Biochim. Biophys. Acta.*, **694**, 3, pp. 227-277 (1982).

# Dependence of Current Waveform on Laser-Triggered Discharge Plasma for EUV Radiation

Soowon Lim, Takashi Kamohara\*, S. Hamid R. Hosseini\* and Sunao Katsuki

*Institute of Pulsed Power Science, Kumamoto University*

*\*Graduate School of Science and Technology, Kumamoto University*

## ABSTRACT

A powerful extreme ultraviolet (EUV) source is the most important component for EUV lithography and EUV mask inspection. We investigate characteristics of laser-triggered discharge (LTD) plasma at three different current waveforms. A height-adjustable coaxial birdcage was used to change circuit parameters. The rise time was varied between 30 ns to 55 ns with peak current of 10 kA. The time-integrated EUV (at 13.5 nm in 2% bandwidth) intensity for the 30 ns rise time was found to be 54.8% stronger than that of the 55 ns rise time despite its lower energy. Experiments using a high-speed camera were performed to observe the pinch plasma. The fast rise time was found to have advantages such as higher EUV intensity and possibility of plasma control in comparison with the slow rise time.

## Keywords

Extreme ultraviolet, Plasma Sources, High-current plasmas, Electric discharges, High-current technology

## 1. Introduction

Extreme ultraviolet radiation (EUV) spans photon energies of about 30 eV to about 250 eV, with corresponding wavelengths in vacuum extending from about 5 nm to 40 nm. Its short wavelengths enable visualization of structures at the atomic level in microscopy and printing of minute patterns in lithography, currently the two main uses of EUV [1].

Actinic mask inspection are required to support high volume manufacturing using EUV lithography [2]. Actinic mask inspection applications require an in-band (13.5 nm in 2% bandwidth) EUV beam of brightness exceeding 30 W after debris mitigation and spectral purifying filter. Requirements also include 10 ms integrated energy stability of 1% for 1 hour and 14 days of continuous operation sans maintenance. Three types of EUV sources exist for mask inspection application: Sn laser-produced plasma, Xe gas discharge-produced plasma, and Sn laser-triggered discharge (LTD) plasma. In 2015, an EUV source for mask inspection application was

developed at Ushio, Inc. using a Sn LTD plasma technology. Radiance was reported to be 145 W/mm<sup>2</sup>/sr (peak value) behind the debris shield as clean usable radiance. This sufficient radiance thus makes LTD plasma source a promising candidate for actinic mask inspection applications.

Our previous investigations into physical limitations of LTD plasma source under high-rep-rate conditions found that debris generated by previous discharge can be vaporized by a subsequent trigger laser during continuous discharge. However, this results in a large amount of tin vapor between electrodes and it discourages a strong Z-pinch [3].

Debris scattering near electrodes is an unavoidable consequence of using plasma to generate photons [4]. Bulgakova and Bulgakov give an excellent treatment of this subject [5], describing the mechanism of liquid droplet ejection by pulsed laser ablation of solids. Because radiation power relies on discharge current, its decrease can deplete EUV intensity ( $\propto I^4$ ) [6]. Thus, reducing discharge energy while

simultaneously maintaining discharge current peak is necessary in order to reduce debris yield and thermal load on electrodes. In other words, improving energy conversion efficiency is necessary.

In this paper, we investigate characteristics of LTD plasma at different current waveforms while simultaneously maintaining discharge current peak. Plasma dynamics were observed using both a Mach-Zehnder interferometer and a high-speed camera. Positions of the pinch region and compression processes are compared and discussed.

## 2. Experimental Methods

Figure 1 shows a schematic diagram of the LTD plasma source. The cathode and anode were tin rods with respective diameters of 8 mm and 3 mm. The distance between electrodes was 3 mm. A tungsten cylinder was used to connect the cathode to a 42 nF capacitor bank. A coaxial birdcage with 8 height-adjustable arms was used to adjust total circuit inductance. The birdcage held the anode and was grounded. The current rise time was variable from 30 ns to 55 ns (20~80% of the peak value). In order to maintain the peak current at 10 kA, the capacitor bank was charged to 11.8 kV and 22 kV for the fast and slow rise times, respectively. Once the capacitor bank was fully charged, a triggering laser beam (Nd:YAG, 532 nm, 12 mJ) focused on the cathode surface at a surface angle of 45 degree to create tin ablation plasma. The plasma then bridged both electrodes to ignite discharge. A pulsed current with

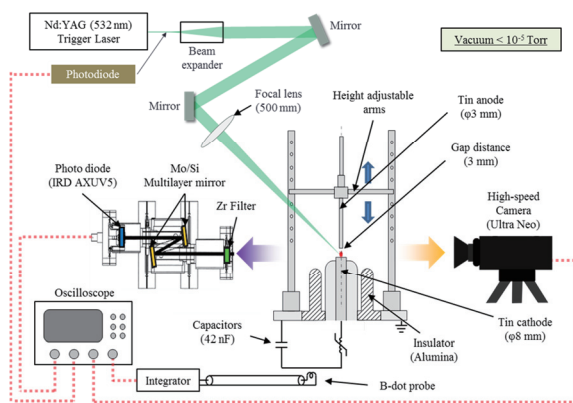


Fig. 1 Schematic diagram of the laser-triggered discharge plasma source

peak amplitude of 10 kA flowed into the plasma. Pulsed current flow was unidirectional due to a saturable inductor (Hitachi Metals FINEMET FT-3H) in the discharge circuit. The pulsed current increased plasma density and temperature, which then emitted EUV light.

EUV intensity was monitored by a EUV photo diode (IRD AXUV5) after passing through a spectrum bandpass filter (2% at 13.5 nm). The filter consisted of two silicone/molybdenum multilayer mirrors and a zirconium filter. The photo diode was reverse-biased at 30 V. EUV intensity was measured at an angle of 90 degree to the electrodes axis. Discharge current was measured by a calibrated B-dot probe. Parameters such as a length of cables and laser beam paths were adjusted in order to calculate signal timing. Time references of all measured signals were recalculated to the arrival time of the triggering laser beam at the cathode surface.

Visible light emission from the LTD plasma was monitored by a high-speed camera (NAC image Tech., ULTRA Neo), which has a maximum framing rate of  $200 \times 10^6$  frames per second. The camera enabled visualization of the series of changes in a single discharge plasma.

## 3. Results and Discussion

### 3.1 Effects of current pulse rise time on EUV intensity

Figure 2 show typical waveforms of the current and EUV intensity. Current flow began about 100 ns after trigger laser irradiation. The charged energies of the capacitor bank were 2.9, 6.2 and 10.2 J for fast, intermediate and slow rise times, respectively. The EUV intensity fluctuates around the peak. The signal might reflect the complicated magnetohydrodynamics (MHD) of the plasmas during the pinch process. EUV is emitted mainly from small hot spots that are caused by plasma instability and take place intermittently along the z axis as long as the plasma current is sufficiently large.

EUV intensities were time-integrated after subtracting offset voltages (Figure 2-(c)). The time-integrated EUV intensity for the fast rise time

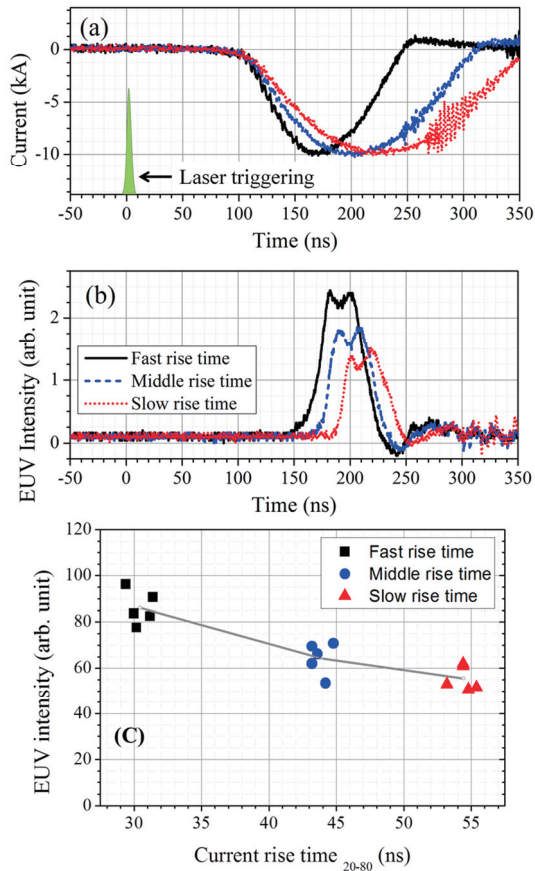


Fig. 2 Typical waveforms of laser-triggered discharge plasma source (a) Discharge current waveform (b) EUV intensity measured by photodiode (c) Integrated extreme ultraviolet intensity

was 55% stronger than that of the slow rise time despite its lower energy. In terms of energy efficiency, EUV intensity of the fast rise time was 5 times stronger per joule than that of the slow rise time.

### 3.2 Visible light emission from LTD plasma

Photographs of visible light emission from LTD plasma at different current waveforms are shown in Figure 3. EUV signals were measured at almost simultaneously with the appearance of bright regions in Figure 3. Therefore, it is reasonable to consider that the bright regions are hot dense plasma which emits EUV. The fast rise time first displayed light plasma in an hourglass shape, which subsequently lengthened, narrowed, and brightened. Eventually,

the plasma separated into multi-parts at around 65~75 ns. The light emission near the cathode was due to bombardment of the tin ion. The slow rise time initially displayed unclear light plasma; bright plasma then appeared at a relatively higher position than that of the fast rise time. The center of the bright plasma began to separate into two parts and finally disappeared.

These phenomena seem to be related to the tin vapor density distribution at the start of pinching (Figure 4), which is when magnetic field pressure exceeds plasma particle pressure [6]. Instability considerations allow Z pinch of the fast rise time to be classified as current pulse time shorter than magnetohydrodynamics (MHD) time (Fig. 4-(a)), and that of slow rise time as pulse time greater than the MHD time [7] (Fig. 4-(d)). The fast rise time displays less significant influence of MHD instability, resulting in more uniform compression of plasma. At this time, the uniform compression confines the tin fuel as well (Fig. 4-(a)). The compressed plasma then turns into  $m=0$  sausage-type instability (Fig. 4-(b)). In this case, due to its long thin structure, the growth rate is relatively high; therefore, the instabilities grow simultaneously, resulting in a multiple break points (Fig. 4-(c)).

The slow rise time displays difficulty in plasma compression near the cathode because of high-plasma particle pressure, resulting in neck instability rather than uniform compression (Fig. 4-(d)). The growth rate is relatively low in this case, but the initial pinching energy is concentrated into one instability. This instability creates a small localized region of high temperature (Fig. 4-(e)). The tin fuel is also pushed out, leaving only a small amount of tin fuel in the high-temperature region during the compression process. At last, the high-temperature plasma separates into two parts, with each moving respectively upward and downward (Fig. 4-(f)). This movement of the plasma can be explained by the 'zipper effect', which is a tapered radial constriction of the plasma column that propagates along the vertical pinch axis during the final stages of compression [8].

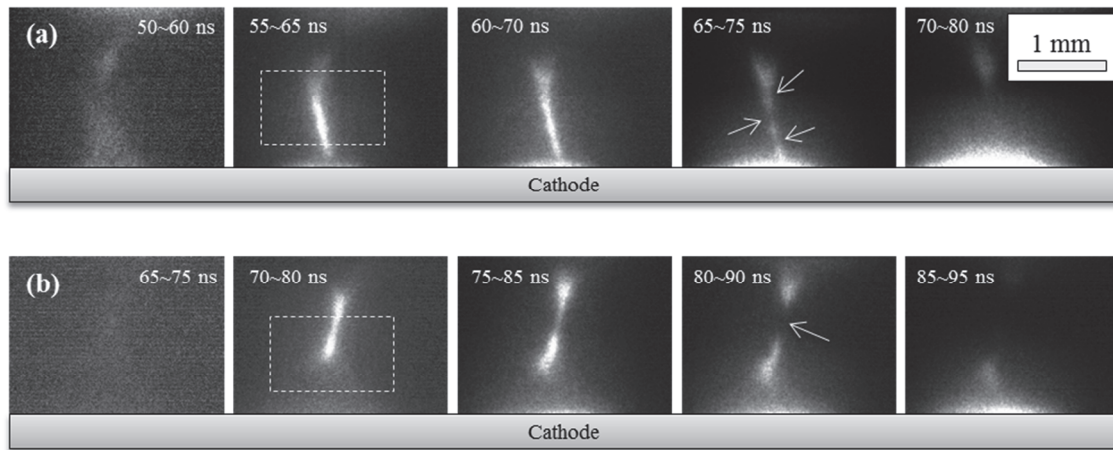


Fig. 3 Photographs of visible light emission from the laser-triggered discharge plasma  
 (a) Fast rise time (b) Slow rise time

The fast rise time displayed sufficient tin fuel density in the region of high-temperature plasma due to compression uniformity. Also, the pinch can be controlled because the compression process is less influenced by MHD instability. The slow rise time, however, displays lower tin fuel density than that of the fast rise time (Fig. 4-(d)). Moreover, the plasma temperature will tend to be too hot, exceeding the temperature for 13.5 nm emission, because the initial pinching energy is concentrated into the small localized region.

The current waveform for LTD plasma can be considered as two phases. During the first phase, current flows through the hollow cylindrical low density plasma and gathers the plasma together with the vapor to the center, which takes some time (~tens of ns). This time might be a limiting factor for

efficiency enhancement. Subsequently, the second phase of the current compresses the plasma to a high density and high temperature. Plasma uniformity along z-axis is mainly caused by the gas distribution and finally enhanced by the plasma instability. At this moment, plasma current needs to be sufficiently large before the growth of instability for high power EUV radiation.

#### 4. Conclusions

We have characterized laser triggered tin discharge plasmas driven by 10 kA pulsed currents with different current rise times of 30 to 55 ns. The time-integrated EUV intensity for the fast rise time was 55% stronger than that of the slow rise time despite its lower energy. EUV intensity of the fast rise time was 5 times stronger per unit energy than that of the slow rise time. Experiments using a high-speed camera were performed to observe the pinch plasma, enabling comparison and discussion of plasma compression processes. Results of the optical diagnostics indicate that a fast rise current enables more uniform compression resulting in higher tin fuel confinement in the high temperature region. The current waveform for LTD plasma had two phases. During the first phase, current flowed through the hollow cylindrical low density plasma and gathered the plasma together with the vapor to the center. Subsequently, the second phase of the current compressed the plasma to a high density and high

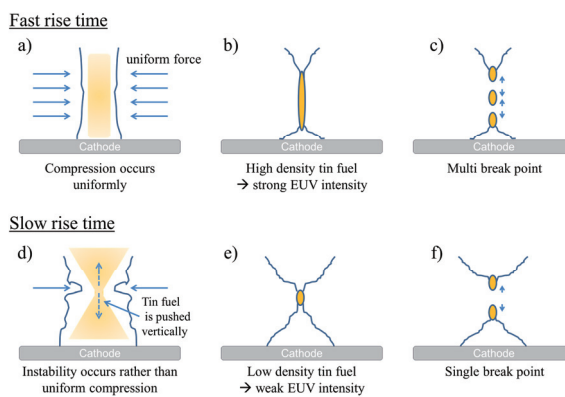


Fig. 4 Diagrams of laser-triggered discharge plasma

temperature. The time required for the first phase might be a limiting factor for efficiency enhancement as this time determines plasma uniformity and fuel gas distribution prior to the onset of plasma instability. Consequently, we found advantages offered by the fast rise time including higher EUV intensity and the possibility of plasma control.

## References

- [1] D. Attwood, *Soft X-Rays and Extreme Ultraviolet Radiation: Principles and Applications*, 1st ed. New York, NY, USA: Cambridge University Press, 2007.
- [2] Y. Teramoto *et al.*, “High-radiance LDP source for mask-inspection application,” presented at the SPIE Advanced Lithography, San Jose, California, United States, 2015, vol. 9422, p. 94220F–94220F–9.
- [3] S. Lim *et al.*, “Optical observations of post-discharge phenomena of laser-triggered discharge produced plasma for EUV lithography,” *Jpn. J. Appl. Phys.*, vol. 54, p. 01AA01, Jan. 2015.
- [4] Vivek Bakshi, Ed., “Chapter 36 Origin of debris in EUV sources and its mitigation,” in *EUV sources for lithography*, Bellingham, Washington: SPIE Publication, 2006.
- [5] N. M. Bulgakova and A. V. Bulgakov, “Pulsed laser ablation of solids: transition from normal vaporization to phase explosion,” *Appl. Phys. A*, vol. 73, no. 2, pp. 199–208, Aug. 2001.
- [6] Vivek Bakshi, Ed., “Chapter 6 Radiative collapse in Z pinches,” in *EUV sources for lithography*, Bellingham, Washington: SPIE Publication, 2006.
- [7] Vivek Bakshi, Ed., “Chapter 8 Z\*code for DPP and LPP source modeling,” in *EUV sources for lithography*, Bellingham, Washington: SPIE Publication, 2006.
- [8] F. S. Felber *et al.*, “Ultrahigh magnetic fields produced in a gas-puff Z pinch,” *J. Appl. Phys.*, vol. 64, no. 8, pp. 3831–3844, Oct. 1988.

# Control of Dense Laser-Produced Plasma Flow Using a Magnetic Nozzle

H. Wakabayashi, K. Hiraide, J. Hasegawa, T. Kawamura, K. Horioka

*Department of Energy Sciences, Tokyo Institute of Technology*

## ABSTRACT

The emission of laser plasma expanding along a magnetic nozzle has investigated by high temporal resolved spectroscopy in order to consider the possibility of control by a magnetic nozzle for laser ion source plasma. Changes in temporal distribution of plasma emission spectrum were observed in the various position, strength or shape of magnetic field.

## Keywords

heavy ion fusion, laser ion source, laser-ablation, high-density plasma flow, magnetic nozzle

## 1. Introduction

The driver accelerators for heavy ion fusion (HIF) reactors require ion sources that can provide high current, low emittance, *i.e.* high brightness ion beams. The laser ion source is considered one of the candidates because laser can produce dense plasma directly from solid and ions travel ballistically from a point source to an extraction gap, leading to high current, highly directed ion flow. On the other hand, the laser ion source has some disadvantages such as rapid reduction of ion flux during three-dimensional plasma expansion and ion flux variation during beam extraction. To resolve these problems, control of laser-produced plasma flow by magnetic fields has been recently proposed and demonstrated [1].

Plasma flow control by a magnetic nozzle has been attempted also in the studies of plasma thrusters,

where a current free plasma such as helicon plasma or inductively coupled plasma passes through a divergent magnetic field [2]. In contrast, Harilal *et al.* observed that a transverse magnetic field can suppress the expansion of a laser-produced plasma [3].

When a strong divergent magnetic field is applied to a laser-produced plasma expanding from the laser target, it is also expected that the plasma is transversely suppressed and longitudinally accelerated. Because the magnetic field cannot diffuse into the plasma in the early stage of interaction, ion trajectories in the plasma core are not disturbed by Larmor motions, which maintains the highly directive ion flow of the laser-produced plasma.

The purpose of this study is to examine the feasibility of laser-produced plasma control by a magnetic nozzle. We perform temporally and spatially

resolved observation of light emissions from a laser-produced plasma modulated by a magnetic field.

## 2. Experimental Setup

A schematic of the experimental setup is given in Fig. 1. The plasma production chamber was evacuated down to about  $10^{-5}$  Pa by a turbo molecular pump. To produce a plasma, a KrF excimer laser ( $\lambda=248$  nm, 200-300 mJ, 30 ns FWHM) was focused by a plano-convex lens through an optical window onto a plane copper target with an incident angle of  $45^\circ$ . The target was mounted on an automatic two-axis stage to change the laser irradiation position on the target without breaking vacuum. We changed the target position every 10-20 shots to prevent the degradation of plasma production reproducibility caused by target surface deformation.

A single turn coil was located near the laser target to apply a magnetic field. A pulse current of 550 A (peak) from a LCR circuit induced a magnetic field of 245 mT on the center axis of the coil at maximum. The coil was located 1 mm or 3 mm downstream from the target. Because of skin effect, the magnetic field cannot penetrate the Cu target in the early stage of magnetic field excitation. We calculated the shape of the field lines by COMSOL Multiphysics®. The

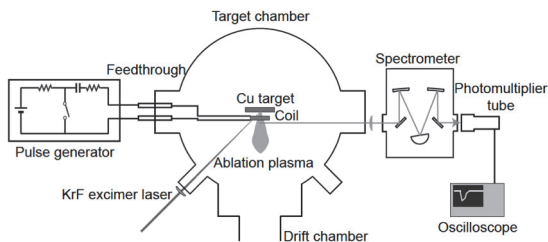
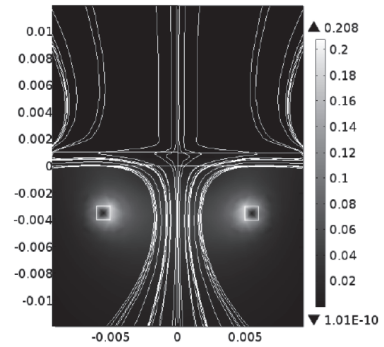


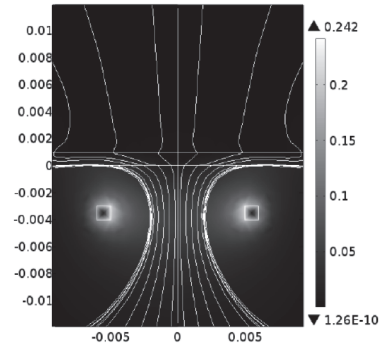
Fig. 1: A schematic of experimental setup.

calculated magnetic field distributions 10, 20, and 40  $\mu$ s after the triggering of the circuit are shown in Fig. 2.

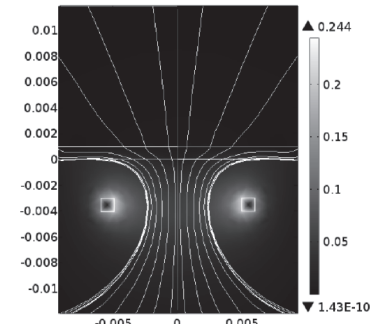
We evaluated magnetic field strength necessary to balance the magnetic pressure with the plasma pressure. Thermal pressure of laser-produced plasma was calculated as a function of the distance from the



(a) 10  $\mu$ s



(b) 20  $\mu$ s



(c) 40  $\mu$ s

Fig. 2: Time evolution of the magnetic field induced by a single turn coil near the target.

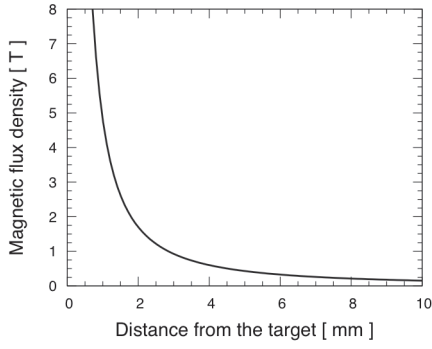


Fig. 3: Required magnetic flux density estimated from the balance between magnetic pressure and plasma pressure.

target along the plasma expansion axis with the following assumptions: plasma spherically and uniformly expands from the laser spot; plasma temperature is 1 eV; ten percent of laser pulse energy (250 mJ) is used for plasma production. Figure 3 plots the magnetic flux density as a function of the distance from the laser target, which is required to establish the balance between the plasma pressure and the magnetic pressure. Near the target ( $\sim 1$ -2 cm), a magnetic flux density of hundreds of mT to a few T is required.

For spatially resolved plasma spectroscopy, light from a laser-produced plasma was focused by a plano-convex lens onto the entrance slit of a monochromator. Certain spectral lines of from atoms or ions in the plasma are observed separately by the monochromator. The temporal transition of the light intensity was recorded by an oscilloscope after the signal magnification by a photomultiplier-tube.

### 3. Results and Discussion

Temporal evolutions of spectral line intensities ( $\lambda=521$  nm (Cu I) and  $\lambda=490$  nm (Cu II)) observed in two different magnetic field configurations; the gap

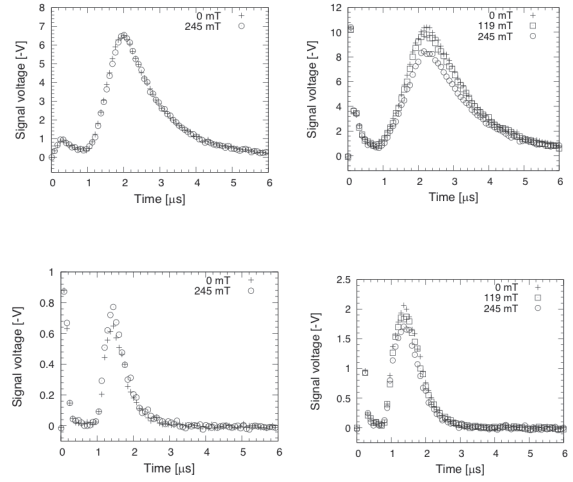


Fig. 4: Temporal change of spectral line intensities (upper row:  $\lambda=521$  nm from Cu I, lower row:  $\lambda=490$  nm from Cu II) observed at 20 mm downstream with two different target and coil gap lengths (left column: 1 mm, right column: 3 mm).

lengths between the target and the coil were 1 mm and 3 mm) are shown in Fig. 4. The observation point is 20 mm downstream from the target. The light intensity from Cu II was obviously enhanced by applying the magnetic field when the coil was located 1 mm from the target. In contrast, when the coil was located at 3 mm from the target, the signal was depressed. In both cases the plasma ions are modulated by the magnetic field. These results indicate that when the coil is located 1 mm from the target, the ions are transversely confined by the magnetic field, leading to the increase in the plasma density. In contrast, when the coil is located 3 mm from the target, some ions may be pushed back towards the target by the converging magnetic field in the gap between the target and the coil. Interestingly, when the coil is located 3 mm from the target, the light intensities from neutral atoms are also depressed. Since neutral atoms are not affected directly by the magnetic field, this

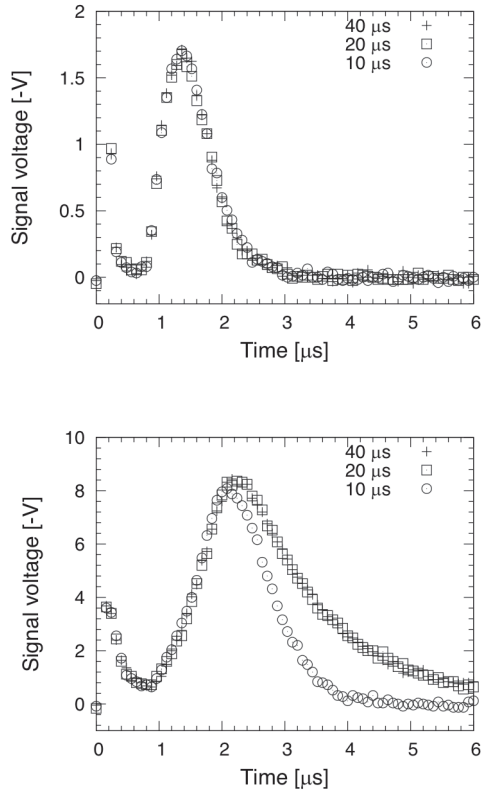


Fig. 5: Time evolutions of spectral line intensities (upper:  $\lambda=490$  nm from Cu II, lower:  $\lambda=521$  nm from Cu I) observed under various timing of laser irradiation.

result indicates that the flow of the neutral atoms are impeded by collisions between neutral atoms and ions.

To investigate the effect of the magnetic field shape on the behavior of the plasma, spectral line intensities were observed by changing the timing of laser irradiation with respect to the excitation current. As shown in Fig. 3, the shape of the magnetic field near the target changes depending on the delay times (10, 20, and 40  $\mu$ s). On the other hand, as for emissions from Cu<sup>+</sup> ions (Fig. 5, upper), there is no significant difference among the waveforms with different delay times. In contrast, light intensities from the neutral copper atoms attenuates rapidly with a delay time of 10  $\mu$ s (Fig. 5, lower), when the converging structure of

the magnetic field near the target was more remarkable.

#### 4. Conclusion

We investigated the behavior of a laser-produced plasma flow passing through a magnetic nozzle, which has converging and diverging field structure with a maximum magnetic flux density of 245 mT, using temporally and spatially resolved spectroscopy. When the position of the magnetic nozzle is relatively far from the target, the force pushing back the plasma seems to be remarkable. By inducing the magnetic nozzle more closely to the target, the directivity of the plasma ions seems to be improved. Surprisingly the flow of the neutral atoms was found to be affected by the magnetic nozzle even though they are not directly modulated by the magnetic field, which indicates collisional interactions between the ions and the atoms in the small space between the coil and the target. In the present study, the modulations observed in the waveforms of spectral line intensities were not so large probably because the applied magnetic pressure was not enough to overcome the thermal pressure of the laser-produced plasma particularly in the initial stage. Thus, stronger magnetic field is necessary to observe more significant effect of the magnetic nozzle on dense laser-produced plasma.

#### References

- [1] S. Ikeda *et al.*, Rev. Sci. Instrum. **87**, 02A912 (2016).
- [2] B.W. Longmier *et al.*, Plasma Sources Sci. Technol. **20**, 015007 (2011).
- [3] S.S. Harilal *et al.*, Phys. Rev. E **69**, 026413 (2004).

# Generating Chaos by Semiconductor Injection Laser System for Electric Power Demand Prediction

Satoshi Higuchi, Satoshi Ebisawa, and Go Imada

*Dept. Info. & Electron. Eng., Niigata Institute of Technology,  
1719 Fujihashi, Kashiwazaki, Niigata 945-1195, Japan*

## ABSTRACT

To improve the quality of electric power demand prediction, we have been applied the chaos into the prediction model. The chaos is generated by semiconductor injection laser system with external optical feedback. In the modeled single-mode, distributed-feedback semiconductor laser system, the chaos oscillation occurs at the feedback coefficient more than  $3.0 \times 10^9 \text{ s}^{-1}$  and the injection coefficient more than  $3.0 \times 10^9 \text{ s}^{-1}$ . The rate of orbit magnification of the chaos can be controlled by changing the feedback coefficient. The rate of orbit magnification reaches 0.8 at the feedback coefficient of  $3.0 \times 10^{11} \text{ s}^{-1}$ . In this condition, however, the chaos having the controlled difference of the rate of orbit magnification more than 0.5 cannot be obtained.

## Keywords

Electric power demand prediction, Chaos, Semiconductor laser

## 1. Introduction

In the electrical power technology, the followings are interested in the electric power demand: (1) electric power generation adapted in local properties, (2) storage of generated electrical power, and (3) efficient use of electric power such as pulsed power technology. Moreover, the electric power demand prediction is important to supply the electrical power in stable and safety. The prediction model specialized with electricity consumption in each apparatus is proposed. In this model, the time-resolved electrical power demand  $D(t)$  is estimated by following equation [1].

$$D(t) = \sum_i Q_i(t) \cdot K_i(t) \quad (1)$$

where  $Q_i(t)$  is the electricity consumption in each electrical apparatus,  $K_i(t)$  is the total number of the each apparatus,  $i$  is the assignment of each apparatus, and  $t$  is the time.

In this study, the chaos theory is applied to Eq. (1) and the chaos generating with semiconductor laser is evaluated to improve the prediction quality.

## 2. Electric Power Demand Prediction by using Chaos

The time history of electric power demand depends on the chaos theory. Figure 1 shows the two-dimensional reconstruction of the time history of electric power demand. The electric power demands in each day are different in the time domain. In the reconstruction domain, however, the orbits of electric power demand are same because the time history of electric power demand has a chaos characteristic (see Fig. 1(b)).

The electric power demand can be predicted from some pseudo electric-power demand data in the time domain by using similarity of these orbits in the reconstruction domain. In this scheme, the orbits and the pseudo data are produced by using the actual data and the chaos, respectively. Hence, there is no need to fix the weather condition in the prediction. To improve the prediction, we need many pseudo date separately. If the chaos having the controlled difference of the rate of orbit magnification more than 0.5 can be generated [2], the quality of electric power demand prediction will be improved.

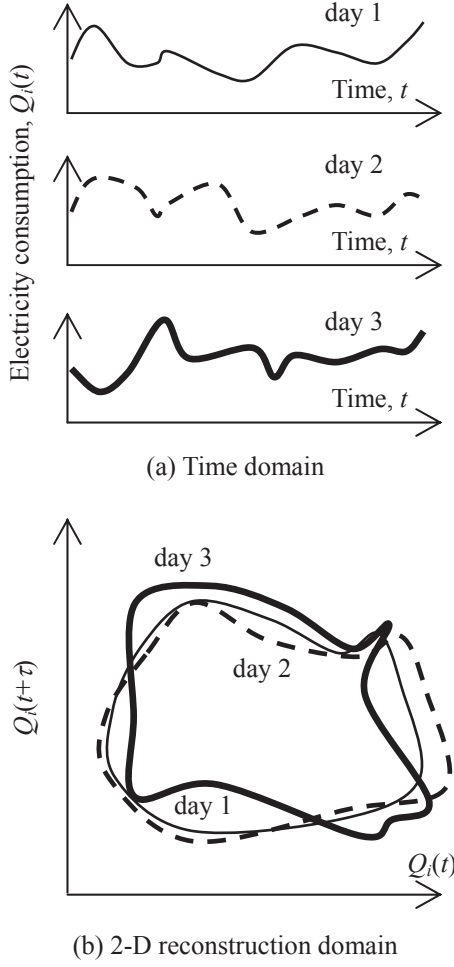


Fig. 1 Two-dimensional reconstruction of time history of electric power demand.

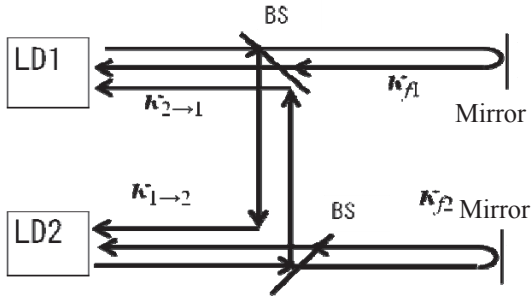


Fig. 2 Modeled laser system using single-mode, DFB semiconductor laser.

### 3. Numerical Simulation

In this study, the chaos is generated by semiconductor injection laser system with external optical feedback. Figure 2 shows the modeled laser

system using single-mode, distributed-feedback (DFB) semi-conductor laser. The laser light emitted from the laser diode LD1 is divided by the beam splitter into the beam traveling forward mirror 1 and the beam traveling forward LD2. The beam traveling forward mirror 1 is fed back to LD1 as a feedback light. The beam traveling forward LD2 is injected into LD2. This system is operated as the injection laser system with external optical feedback because of the symmetrical arrangement.

The amplitude  $A$  and phase  $\Phi$  of laser light, and the carrier density  $N$  of LD1 and LD2 are calculated with following rate equations [3].

$$\begin{aligned} \frac{dA_1(t)}{dt} = & \frac{1}{2} \left[ G_N(N_1(t) - N_0) - \frac{1}{\tau_p} \right] A_1(t) \\ & + \kappa_{f1} A_1(t - \tau) \cos \{ \Phi_1(t) - \Phi_1(t - \tau) + \omega \tau \} \\ & + \kappa_{2 \rightarrow 1} A_2(t - \tau_c) \cos \{ \Phi_1(t) - \Phi_2(t - \tau_c) + \omega \tau_c \} \end{aligned} \quad (2)$$

$$\begin{aligned} \frac{d\Phi_1(t)}{dt} = & \frac{1}{2} \alpha \left[ G_N(N_1(t) - N_0) - \frac{1}{\tau_p} \right] A_1(t) \\ & - \kappa_{f1} \frac{A_1(t - \tau)}{A_1(t)} \sin \{ \Phi_1(t) - \Phi_1(t - \tau) + \omega \tau \} \\ & - \kappa_{2 \rightarrow 1} \frac{A_2(t - \tau_c)}{A_1(t)} \sin \{ \Phi_1(t) - \Phi_2(t - \tau_c) + \omega \tau_c \} \end{aligned} \quad (3)$$

$$\frac{dN_1(t)}{dt} = J_1 - \frac{N_1(t)}{\tau_s} - G_N(N_1(t) - N_0) \{ E_1(t) \}^2 \quad (4)$$

$$\begin{aligned} \frac{dA_2(t)}{dt} = & \frac{1}{2} \left[ G_N(N_2(t) - N_0) - \frac{1}{\tau_p} \right] A_2(t) \\ & + \kappa_{f2} A_2(t - \tau) \cos \{ \Phi_2(t) - \Phi_2(t - \tau) + \omega \tau \} \\ & + \kappa_{1 \rightarrow 2} A_1(t - \tau_c) \cos \{ \Phi_2(t) - \Phi_1(t - \tau_c) + \omega \tau_c \} \end{aligned} \quad (5)$$

$$\begin{aligned} \frac{d\Phi_2(t)}{dt} = & \frac{1}{2} \alpha \left[ G_N(N_2(t) - N_0) - \frac{1}{\tau_p} \right] A_2(t) \\ & - \kappa_{f2} \frac{A_2(t - \tau)}{A_2(t)} \sin \{ \Phi_2(t) - \Phi_2(t - \tau) + \omega \tau \} \\ & - \kappa_{1 \rightarrow 2} \frac{A_1(t - \tau_c)}{A_2(t)} \sin \{ \Phi_2(t) - \Phi_1(t - \tau_c) + \omega \tau_c \} \end{aligned} \quad (6)$$

$$\frac{dN_2(t)}{dt} = J_2 - \frac{N_2(t)}{\tau_s} - G_N(N_2(t) - N_0) \{ E_2(t) \}^2 \quad (7)$$

where  $\tau$  is the feedback delay time,  $\alpha$  is the linewidth broadening factor,  $G$  is the liner gain coefficient of laser medium,  $\tau_p$  is the photon life time,  $\tau_s$  is the carrier life time,  $\tau_c$  is the passing time of light in laser medium,  $J$  is the current density of laser diode,  $\omega$  is the angular frequency of laser light,  $E$  is the complex electrical field of laser light,  $\kappa$  is the feedback and injection coefficient, and the subscripts 1 and 2 indicate LD1 and LD2, respectively. Here, the feedback coefficient can be obtained as

$$\kappa_f = \frac{1}{\tau_c} \frac{(1-r_2^2)r_3}{r_2} \quad (8)$$

where  $r_2$  and  $r_3$  are the reflectance of the beam splitter and the mirror, respectively [4].

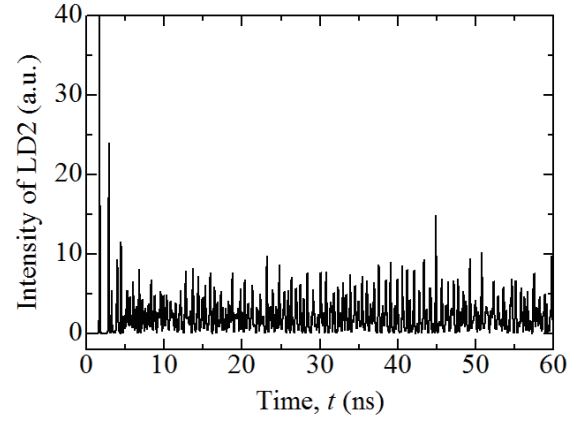
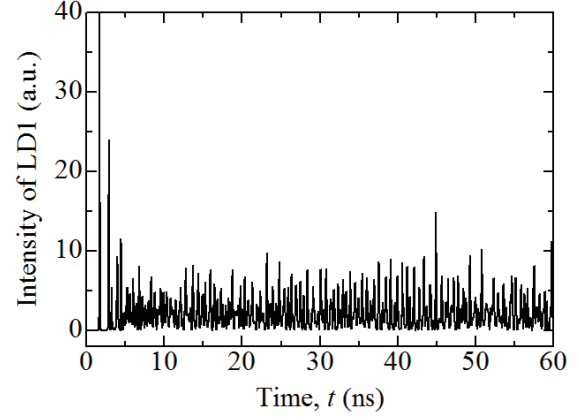
The parameter to solve Eqs. (2)–(7) are summarized in Table I [3].

## 4. Results and Discussion

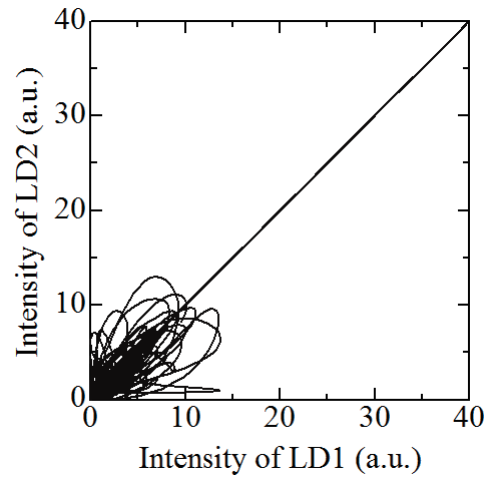
### 4.1 Chaos generation

Figure 3 shows the typical time history of intensity of laser light (a) and the intensity mapping of laser light (b). It is possible to generate the chaos, in this system, if the feedback coefficient increases. Here, we assume that the feedback coefficient is  $\kappa_{f1} = \kappa_{f2} = 3.0 \times 10^9 \text{ s}^{-1}$  and the injection coefficient is  $\kappa_{2 \rightarrow 1} = \kappa_{1 \rightarrow 2} = 3.0 \times 10^9 \text{ s}^{-1}$ . The laser light intensity of LD1

and LD2 are shown in Fig. 3(a). It seems that the light emitted from LD1 and LD2 oscillates like a chaos. The time history of intensity of laser light in



(a) Typical time history of intensity of laser light



(b) Intensity mapping of laser light

Fig. 3 Chaos oscillation in laser system.

Table I Parameter of laser system.

$G_N$	$8.4 \times 10^{-13} \text{ m}^3 \text{ s}^{-1}$
$N_0$	$1.4 \times 10^{24} \text{ m}^{-3}$
$\tau_p$	$1.927 \times 10^{-12} \text{ s}$
$\tau_s$	$2.04 \times 10^{-9} \text{ s}$
$\tau$	$1.5 \times 10^{-9} \text{ s}$
$\tau_c$	$1.5 \times 10^{-9} \text{ s}$
$\alpha$	3.0
$J$	$1.1 \times 10^{33} \text{ m}^{-3} \text{ s}^{-1}$
$\omega$	$1.226 \times 10^{15} \text{ s}^{-1}$

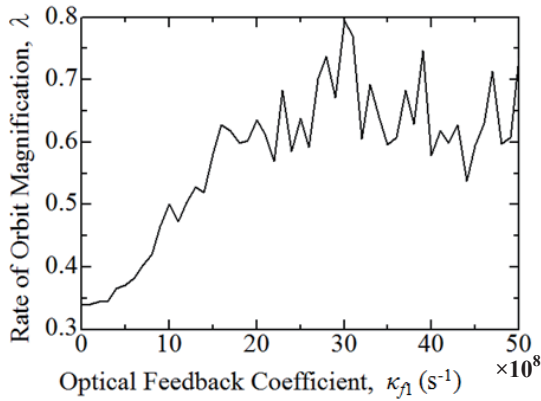


Fig. 4 Rate of orbit magnification as a function of feedback coefficient.

LD1 looks like that of LD2. Figure 3(b) shows the intensity mapping at the synchronized timing in Fig. 3(a). We can confirm that the intensity of LD2 depends on that of LD1 linearly. Hence, the chaos synchronization occurs in this system.

#### 4.2 Increase of rate of orbit magnification of chaos

To improve the quality of electric power demand prediction using chaos, it is necessary to generate the many complicated chaos. The complexity of chaos is indicated as the rate of orbit magnification. Figure 4 shows the rate of orbit magnification  $\lambda$  as a function of the feedback coefficient  $\kappa_1$ . Here, the feedback and injection coefficient is assumed as  $\kappa_2 = \kappa_{2 \rightarrow 1} = \kappa_{1 \rightarrow 2} = 3.0 \times 10^9 \text{ s}^{-1}$ . The rate of orbit magnification increases as the feedback coefficient increases. The rate of orbit magnification reaches 0.8 at the feedback coefficient of  $\kappa_1 = 3.0 \times 10^{11} \text{ s}^{-1}$ . In this condition, however, the chaos having the controlled difference of the rate of orbit magnification more than 0.5 cannot be obtained.

## 5. Conclusions

The chaos generated by semiconductor injection laser system with external optical feedback is numerically simulated to improve the quality of electric power demand prediction. In the modeled laser system using single-mode, DFB semi-conductor laser, the chaos oscillation occurs at the feedback coefficient more than  $3.0 \times 10^9 \text{ s}^{-1}$  and the injection coefficient more than  $3.0 \times 10^9 \text{ s}^{-1}$ . The rate of orbit magnification reaches 0.8 at the feedback coefficient of  $3.0 \times 10^{11} \text{ s}^{-1}$ . In this condition, however, the chaos having the controlled difference of the rate of orbit magnification more than 0.5 cannot be obtained.

The increase of rate of orbit magnification is the subject for a future study.

## References

- [1] H. Awata et al., "Chuuki Denryoku Juyou Yosoku Moderu", *Denryoku Keizai Kenkyu*, No. 19, pp. 125-139 (1994) (in Japanese).
- [2] S. Ebisawa and S. Komatsu, "Message Encoding and Decoding Using an Asynchronous Chaotic Laser Diode Transmitter-Receiver Array", *Appl. Opt.*, **46**(20), pp. 4386-4396 (2007).
- [3] K. Kusumoto and J. Ohtsubo, "Anticipating Synchronization Based on Optical Injection-Looking in Chaotic Semiconductor Lasers", *IEEE J. Quantum Electron.*, **39**(12), pp. 1531-1536 (2003).
- [4] R. Lang and K. Kobayashi, "External optical feedback effects on semiconductor injection laser properties", *IEEE J. Quantum Electron.*, **16**(3), pp. 347-355 (1980).

# Terahertz Radiation from Laser Created Plasma by Applying a Transverse Static Electric Field

Takuya Fukuda<sup>(1)</sup>, Koji Katahira<sup>(1)</sup> and Noboru Yugami<sup>(1)</sup>

<sup>(1)</sup>*Department of Advanced Optical Engineering, Utsunomiya University,  
7-1-2 Yoto, Utsunomiya, Tochigi, 321-8585, Japan  
e-mail: mt156721@cc.utsunomiya-u.ac.jp*

## ABSTRACT

We have been experimentally observed a terahertz (THz) radiation from laser created plasma by applying a transverse static electric field. Some theoretical models have been proposed, however, they are not enough to explain the phenomena of the plasma with the external electric field. We have developed new model to explain this phenomena and confirmed its validity by using 2D-PIC simulation.

## Keywords

terahertz, radiation, external electric field, plasma, laser

## 1. Introduction

Terahertz (THz) radiation with narrow cone structure in the forward direction from high intense femtosecond laser pulse created plasma has been observed [1-3]. This THz radiation is produced by the longitudinal oscillation currents induced by the laser ponderomotive force after the laser propagation.

Additionally, the significantly increased THz emission intensity in the forward direction has been observed when the transverse static electric field is applied to the plasma [4,5]. Aurélien Houard *et al.* have proposed that the radiation source is the transverse oscillation electron current due to shielding of the external electric field. This oscillation frequency is equal to the plasma frequency with decaying in a few electron collision time. However, we have been experimentaly measured the sub-THz radiation, whose frequency is much lower than the plasma frequency. This paper describes the derivation of the mechanism of the THz radiation from laser created plasma by applying the transverse static electric field.

The organization of the present paper is as follows. In Sec.2, the theory which we proposed is described or presented. To verify our theory, we conducted both experiments and 2D-PIC simulation. In Sec.3, we show, present or state experimental results. The simulation results are reported in Sec.4. A summary and discussion are given in Sec.5

## 2. Theory

In the following, we will clarify the electro magnetic field in the plasma when applied external electric field. We take the coordinates  $(x,y,z)$  in this article, where  $x$  is in the longitudinal direction of the laser propagation axis, and  $(y,z)$  plane is the transverse dimension of the laser propagation axis. The static electric field to laser created plasma is applied in the  $y$  direction. The wave equation with external static electric field is written as

$$\left(\frac{\partial^2}{\partial t^2} + \omega_p^2 - c^2 \nabla^2\right) E_y(x,t) = -\omega_p^2 E_{ex}, \quad (1)$$

where  $c$ ,  $\omega_p$  and  $E_{ex}$  are the speed of light, plasma frequency and external static electric field in the  $y$  direction, respectively. Plasma frequency is defined as  $\omega_p = \sqrt{e^2 n_e / m_e \epsilon_0}$ , where  $e$ ,  $n_e$ ,  $m_e$  and  $\epsilon_0$  are electron charge, electron density, mass of electron and permittivity of vacuum, respectively. By the use of the new coordinates  $(\xi = x - v_g t)$  moving with the laser group velocity  $v_g$ , we obtain

$$\left\{ (v_g^2 - c^2) \frac{\partial^2}{\partial \xi^2} + \omega_p^2 \right\} E_y(\xi) = -\omega_p^2 E_{ex}. \quad (2)$$

By applying the Laplace transformation to Eq. (2), we obtain

$$E_y(s) = -\frac{\omega_p}{\sqrt{v_g^2 - c^2}} \frac{\frac{\omega_p}{\sqrt{v_g^2 - c^2}}}{s^2 + \frac{\omega_p^2}{v_g^2 - c^2}} E_{ex}(s), \quad (3)$$

where  $s$  is a complex number frequency parameter. Inverse-Laplace transform of Eq. (3) becomes

$$E_y(\xi) = -\frac{\gamma\omega_p}{c} \int_0^{\xi'} \exp\left\{\frac{\gamma\omega_p}{c}(\xi - \xi')\right\} E_{ex}(\xi') d\xi',$$

where  $\gamma$  is the lorentz factor which is defined as  $\gamma = \frac{1}{\sqrt{1 - v_g^2/c^2}}$ . Then we have

$$E_y(\xi) = E_{ex} \exp\left(\frac{\gamma\omega_p}{c}\xi\right). \quad (4)$$

We use coordinates  $(x,t)$  rather than the coordinate  $\xi$ , electric field in the plasma with the external electric field is

$$E_y(x,t) = E_{ex} \exp\left(\gamma\frac{\omega_p}{c}x - \gamma\frac{v_g}{c}\omega_p t\right). \quad (5)$$

We calculate magnetic field and current density in the plasma with external electric field in the same way as electric field, we obtain

$$B_z(x,t) = -\frac{E_{ex}}{v_g} \left\{1 - \exp\left(\gamma\frac{\omega_p}{c}x - \gamma\frac{v_g}{c}\omega_p t\right)\right\} \quad (6)$$

$$J_y(x,t) = \frac{\varepsilon_0 c}{\gamma v_g} E_{ex} \left\{1 - \exp\left(\gamma\frac{\omega_p}{c}x - \gamma\frac{v_g}{c}\omega_p t\right)\right\} \quad (7)$$

From eq.(5), the electric field at the plasma-gas boundary  $x = 0$  is decayed with  $\gamma v_g \omega_p / c \approx \gamma \omega_p \gg \omega_p$  in time. This means the electric field decays very quickly. From eq.(7), the electron current is induced, however, it is also quickly decayed and does not oscillate, therefore it is different from the previous theory[5].

### 3. Experimental results

Ti:sapphire chirped pulse amplified laser, delivering 120 fs duration (FWHM) pulses at 800 nm, with a maximum energy of 30 mJ per pulse operating at a repetition rate of 10 Hz was used. As illustrated in Fig. 1, laser pulse is focused in air by lens whose focal length is 1000 mm to create plasma. Laser created plasma is applied the transverse static electric field which induced

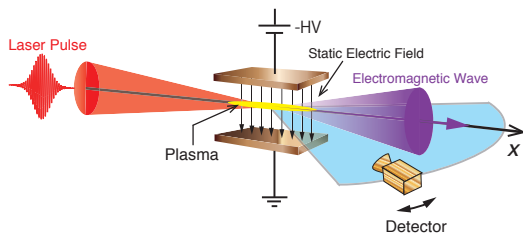


Fig.1 Experimental method for THz generation

by the two electrodes that located along the laser propagation axis. THz radiation intensity from laser created plasma by applied external electric field is detected by the use of crystal detector which is calibrated and has response at the F band (90 - 140 GHz). Fig. 2 shows the angular distribution of the THz emission generation. The conical forward radiation with no radiation on the propagation axis without the transverse static electric field was observed. As the external electric field is bigger, the radiation intensity is bigger on the propagation axis. Fig. 3 shows intensity of the radiated THz wave as a function of the external electric field. THz radiation intensity was proportional to square of the external electric field.

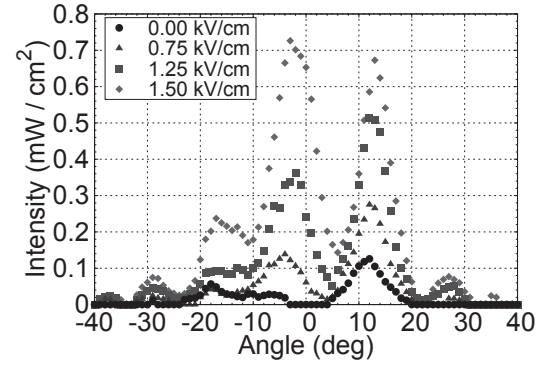


Fig.2 Measurement of the angular distribution of the THz radiation based on the wake current (without external electric field) and based on an applied external electric field (with external electric field)

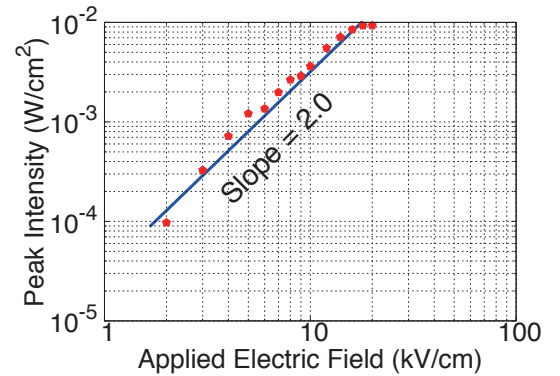


Fig.3 Intensity of the radiated THz wave as a function of the external electric field. THz radiation intensity is proportional to square of the external electric field.

## 4. Simulation results

We used two-dimensional particle-in-cell (2D-PIC) simulation code. The laser pulse whose parameters is same as experiment propagates in the  $x$  direction from left to right and is polarized along the  $z$  axis. We choose  $N_2$  gas with  $10^3$  Pa within  $x \in [0 \mu\text{m}, 300 \mu\text{m}]$ . After the laser propagates,  $N_2$  molecules are ionized, then the plasma whose electron density is  $10^{18} \text{cm}^{-3}$  which corresponds to the plasma frequency  $\omega_p = 9.0$  THz is generated; see Fig. 4. We apply the electric static field in the  $y$  direction to the plasma.

Figure 5 shows the temporal evolution of the laser electric field, electron density, electric field and magnetic field in the laser created plasma ( $x = 100 \mu\text{m}$ ,  $y = 0 \mu\text{m}$ ) with the external electric field. As it is shown in Fig. 5, electric field in the plasma is shielded rapidly, and goes to zero. On the other hand, static magnetic field which corresponding to  $B_z = E_{\text{ex}}/v_g$  is induced. The oscillation currents which is proposed by previous study dose not appear due to the shielding of electric field in the plasma. These results are agreement with our theory.

Intense half cycle THz pulse centered at 1.3 THz whose frequency is much lower than the plasma frequency is radiated from plasma by applied the static electric field. Fig. 6(a) shows intensity of the radiated THz wave as a function of the external electric field. THz radiation intensity was proportional to square of the external electric field. Fig. 6(b) shows angular distribution of the THz radiation. In the absence of static field, we observe the typical conical shape of the THz emission from the longitudinal current. With electric field, intensity of the THz wave increases and is radiated along laser propagation axis. These results is good agreement with experimental results.

## 5. Summary

We have constructed the model of the THz radiation from laser created plasma by applying the transverse static electric field. We confirmed a new theory by the comparison the experimental results and 2DPIC simulation. In the simulation, electric field in the plasma is shielded rapidly, and static magnetic field is induced of the plasma. These results are good agreement with our theory.

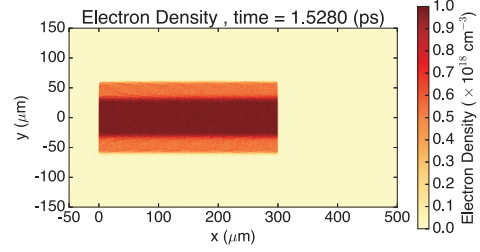


Fig.4 Spatial distribution of the electron density.

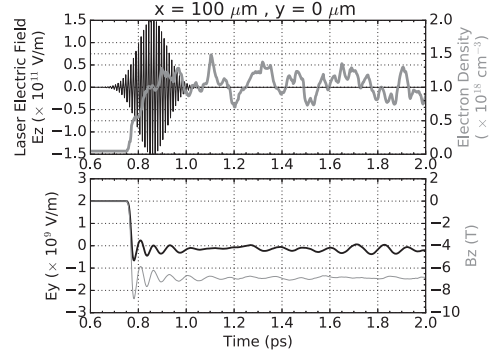


Fig.5 2D-PIC simulation result. Temporal evolution of the laser electric field, electron density, electric field and magnetic field in the laser created plasma ( $x = 100 \mu\text{m}$ ,  $y = 0 \mu\text{m}$ ).

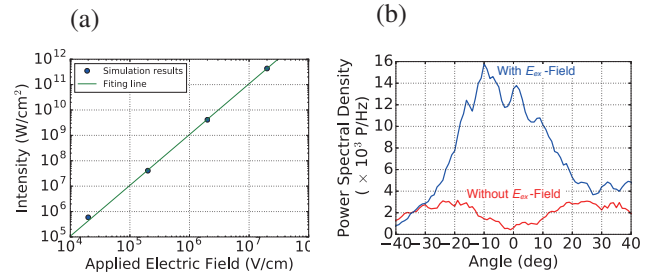


Fig.6 (a) Intensity of the radiated THz wave as a function of the external electric field. THz radiation intensity is proportional to square of the external electric field. (b) Simulation results of the angular distribution of the THz radiation based on the wake current (Without external electric field) and based on an applied external electric field.

## References

- [1] A. Proulx *et al.* Opt. Commun. **174**, 305 (2000).
- [2] N. Yugami *et al.* Jpn. J. Appl. phys. **45**, L1051 (2006).
- [3] C. D. Amico *et al.* New. J. Phys. **10**, 013015 (2008)
- [4] T. Loffler *et al.* Acta Physica Polonica A **107**, p99 (2005)
- [5] A. Houard *et al.* Phys. Rev. Lett. **100**, 255006 (2008)

# Sub-THz electromagnetic wave generation from DARC

Yoshihiro Takada<sup>1)</sup>, Yusuke Hyuga, Noboru Yugami

*Utsunomiya University Faculty of Engineering Department of optical engineering, Yugami Lab.*

*e-mail: mt156714@cc.utsunomiya-u.ac.jp*

## ABSTRACT

The theory of a DC to AC radiation convertor (DARC) was proposed by W. B. Mori *et al.*, in 1995 [1]. The DARC is a electric magnetic wave radiation source of variable frequency and high power and has potential as the terahertz(THz) radiation source. The observed frequency from the DARC was in the sub-THz region and increases with the plasma density. The radiation energy from DARC increased to 1.5 times by using waveguide and hone antenna combination.

## Keywords

DARC(DC to AC Radiation Converter), THz radiation

### 1. Introduction

Electromagnetic wave whose frequency ranged between 0.1 THz and 10 THz is called terahertz-wave. This is located between radio wave and light wave, terahertz-wave can penetrate materials such as paper and plastics, and can be treated with optical elements. In addition, terahertz region is frequency of rotation and vibration of moleculars. Because of these characteristics ,terahertz-wave are expected to various applications, for example, terahertz imaging, non destructive inspection of semiconductor and detecting dengerous material and illegal drug at airport.

The DC to AC Radiation Converter (DARC) is one of sources of terahertz-wave. The theory of the DARC has been proposed by W. B. Mori *et al.*, in 1995 [1]. The DARC has features such as (1) variable frequency (GHz ~ THz), (2) ultrashort pulse, (3) high power, and can be expected for good souce of terahertz-wave.

### 2. Theory of DARC

Figure 1 shows schematic of the DARC. The DARC has a structure that capacitors are arranged at equal interval. The alternately biased capacitors produces a static electric field of the form  $E_y \approx E_0 \sin k_0 x$ , where  $k_0 = d/\pi$ , and  $d$  is the spacing between adjacent capacitor plates. Capacitor array are filled by neutral gas and an ionization front created by laser pulse moves between

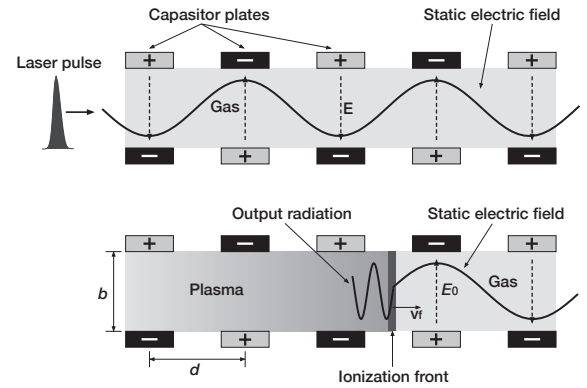


Fig.1 Schematic of dc to ac radiation converter

the plates with velocity  $v_f \approx c$ . In the front's frame, the static electric field becomes electromagnetic wave with almost the speed of light and propagates toward to a stationary plane boundary created by the ionization front. Since the group velocity of the electromagnetic wave incidented to plasma slower than the ionization front, it is observed that the transmitted wave propagates in the same direction as ionization front in laboratry frame. The radiation frequency from the DARC is given by,

$$\omega \approx \frac{k_0 v_f}{2} + \frac{\omega_p^2}{2k_0 v_f} \quad (1)$$

where  $\omega_p$  is the plasma frequency of the ionized gas. Eq.(1).represents that the radiation frequency depends on the wave number of the static electric field and the

electron plasma density of the ionization front. Spectral broadening is given by,

$$\Delta\omega \approx \frac{\omega}{N} \quad (2)$$

where  $N$  is the number of period of the static electric field. Output power is given by,

$$P_{\text{out}} \approx \frac{1}{2} \epsilon_0 E_0^2 v_g A \quad (3)$$

where  $v_g$  is the group velocity of radiation wave and  $A$  is the cross-section area of plasma.

### 3. Experimental Setup

#### 3.1. Terahertz-wave observation experiment

Figure 2 shows experimental setup. We set the DARC in a chamber filled with  $N_2$  gas and create ionization front by Ti:Sapphire laser. A Ti:sapphire laser system operated at 800 nm could deliver up to 35 mJ in a pulse with a duration of 120 fs (FWHM) at 10 Hz repetition rate. The capacitor array consist of 5 capacitors with a period  $d = 2$  mm. The capacitor plates are separated by  $b = 1$  mm. Pulsed high voltage (200 ns (FWHM), up to 2.5 kV) is applied alternatively to the top or bottom plate. The electron density was controlled by varying the gas pressure. In order to separate radiation wave and laser pulse, we used teflon plate (teflon has good transmittance in THz region). Transmitted wave is reflected by off-axis parabolic mirror and detected with 0.1THz-band (90 - 140 GHz), 0.2 THz-band (140 - 220 GHz), 0.3 THz-band (220 - 320 GHz) and 0.4 THz-band (325 - 500 GHz) detectors.

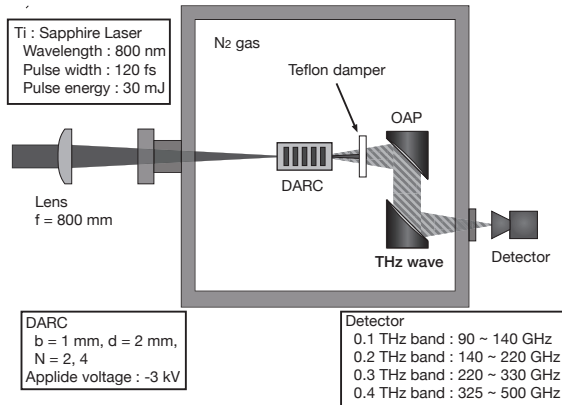


Fig.2 Experimental setup

### 3.2 Power augmentation by waveguide structure

The radiation wave has angler ditribution, so we consider to use waveguide construction to reduce leakage in the side direction. Figure 3 shows the DARC with waveguide structure. Copper plates are arranged at the side and upper side and lower side of the capacitor array. The dimation is  $a = 10$  mm,  $b = 4$  mm. For impedance matching, a hone antenna was attached to waveguide in the radiation direction.

### 4. Result and Discussion

#### 4.1 Terahertz-wave observation experiment

Figure 4 shows spectral intensity of the radiation in gas pressure at 40, 50, 65 and 95 Pa. Applied voltage to capacitor plates is 3 kV. Horizontal errorbar corresponds to frequency range of detectors and Vertical errorbar shows difference of responsivity for each frequency. Radiation central frequency can be find by

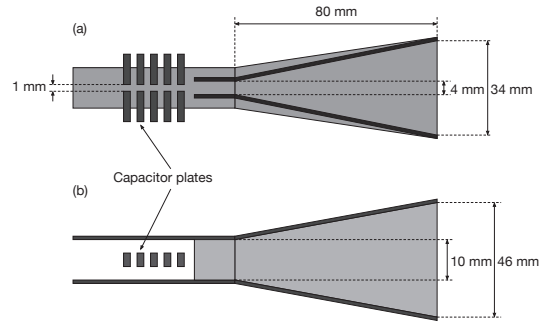


Fig.3 DARC with waveguide structure.(a) is figure looked from the side, and (b) is looked from the upper side.

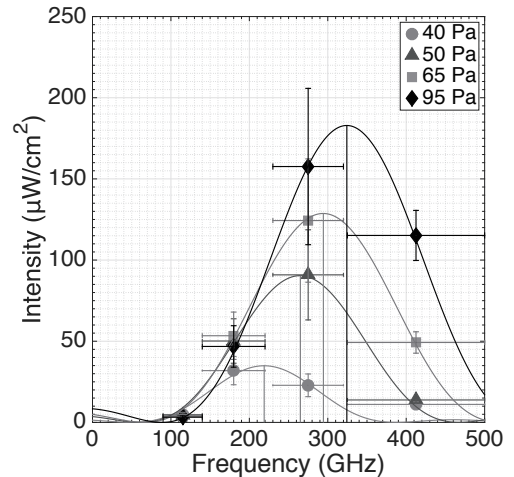


Fig.4 Spectral intensity of the radiation.

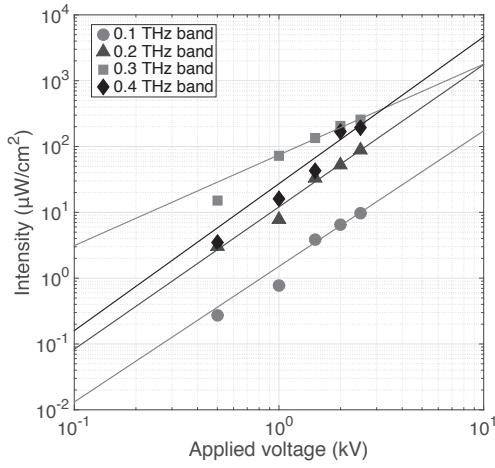


Fig.5 Radiation intensity vs applied voltage.

approximate curve. As gas pressure increases, central frequency increases to 219, 265, 294, 324 GHz. The frequency of output radiation increases with the plasma density increase as the theory predicted.

Figure 5 shows applied voltage dependence of radiation wave. Applied voltage changes from 0.5 to 2.5 kV. Dependences of each detector were almost the square of applied voltage as the theory predicted. This is also evidence of the DARC. However, the maximum intensity of output wave which observed in the experiment was about  $100 \mu\text{W}/\text{cm}^2$ , this is ten digits lower than the intensity predicted by theoretical formula.

Figure 6 shows spectrum intensity of radiation wave when periodic number changes 2 and 4. Gas pressure is 20 Pa and applied voltage is 3 kV. Gas pressure and applied voltage were kept constant during experiment. Radiation intensity increases by two times at each frequency when the periodic number changes from 2 to 4. This result shows output energy increased by extension of static electric field due to change periodic number. The central frequency was 300 GHz at any periodic number, and the spectrum width did not change at 210 GHz.

#### 4.2 Power augmentation by waveguide structure

Figure 7 shows radiation intensity vs gas pressure. Radiation intensity from the DARC with waveguide structure was 1.5 times larger than without waveguide structure. As a result, waveguide structure is effective to augment power of the DARC.

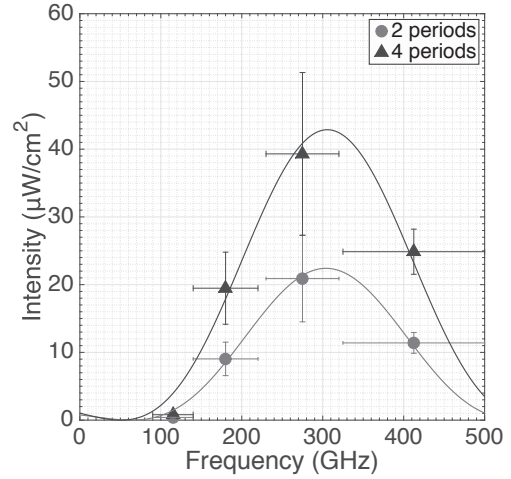


Fig.6 Spectrum of DARC (number of periods is 2 and 4)

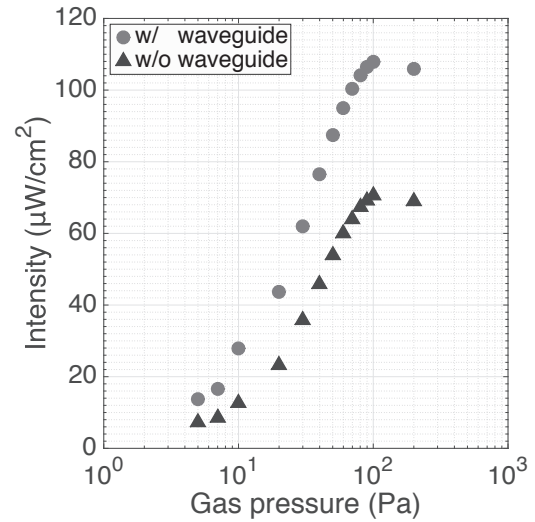


Fig.7 Signal intensity. One is with waveguide structure, and the other is without waveguide.

## 5. Conclusions

Sub-THz radiation was observed in frequency range between 90 to 500 GHz using the DARC. The frequency increases with the plasma density. Observed energy from the DARC structure with the waveguide and the horn antenna combination was 1.5 times larger than without these addition.

## • References

- [1] W. B. Mori, T. Katsulas, J. M. Dawson and C. H. Lai, Phys. Rev. Lett.(1995)

# Fundamental Properties of the Counter-facing Plasma Focus Device for Extreme Ultra-Violet Light Source

Tatsuya Sodekoda<sup>\*1,\*2</sup>, Shintaro Kurata<sup>\*2</sup>, Hajime Kuwabara<sup>\*2</sup>, Kazuhiko Horioka<sup>\*1</sup>

*\*1) Department of Energy Sciences, Tokyo Institute of Technology, Japan*

*\*2) Research Laboratory, IHI Corporation, Japan*

## ABSTRACT

Fundamental properties of a counter-facing plasma focus device were characterized. The plasma dynamics in the device, the out-put energy, the spectra from plasma, images of the plasma radiation, and the recovery rate of electrical insulation, were investigated using a proof-of-principle experimental device. All of the results indicated that the device has potentiality as a high average power extreme ultraviolet light source for the next generation lithography system.

## Keywords

Extreme ultraviolet (EUV), light source, high energy density plasma, plasma focus, counter-facing

## 1. Introduction

An intense radiation in extreme ultraviolet (EUV) region is expected for the next generation lithography system in semiconductor manufacturing. It is the light from a plasma with wavelength of  $13.5\text{nm} \pm 1\%$  (so called “in-band”) considered now for the realization of lithography process using the EUV light. However, the EUV light source device has various problems and is not yet applied for the mass-production process. A practical EUV light source would be essential for development of the future semiconductor industry.

The plasmas made by laser irradiation (LPP: Laser-produced plasma) and energized by electric discharge (DPP: Discharging-produced plasma) are the influential candidate as the EUV light source [1-4]. Important specifications required as the practical lithography light source include high average power of a kW level, smallness of the emission size, low scattering particles (low debris). The EUV output power provided from conventional light sources cannot yet reach for the requirement. Among the issues, increase of average power is the

most serious [2]. That is, when we increase the input power to accommodate the high average power, it leads shortening of the life time of the electrodes and the optical components by the heat load and debris after the operation. Therefore, the increase of the output power and the improvement of the energy conversion efficiency are necessary at the same time to develop a practical EUV source. We have proposed to extend the EUV emission time per pulse, both to increase the output power and to improve the conversion efficiency [5].

In this paper, we show proof of concept experiments and recent results of our research and development for the practical EUV source.

## 2. Concept and Characteristic

It is well-known that the spectrum property of lithium ions is promising. However, output intensity is low compared with Sn plasma, because only few lines contribute the in-band EUV emission. In addition, an effective time duration of  $\mu$  second order is necessary to get the in-band emission from doubly ionized (hydrogen like) lithium ions [6]. This

means we can make use of spectrum property of lithium by maintaining the plasma for more than  $\mu$  second. In other words it becomes a challenge of the EUV research and development to hold the lithium plasma at a high temperature and high density state for a long time in a minute area.

We have developed a new configuration for the EUV light source using “counter-facing plasma focus method” for the next generation lithography system. The device consists of two counter-facing plasma focus electrodes which is expected to produce a high energy density lithium plasma by the collision of the focus plasmas. Also it is expected to be able to confine the plasma by the counter-facing current sheets and can emit the EUV light during the discharge period.

By prolonging the plasma confinement, we can extract higher EUV energy per pulse with high spectrum efficiency. In addition, we can also expect to reduce the debris because, in the configuration, the lithium supply point is far from the location of high energy density plasma.

As the plasma impedance is usually much lower than that of the pulse power generator, we also developed a recyclable power generator for the plasma device. We could recover almost 80% of electric energy during a quasi-continuous operation by the recyclable pulse power driver.

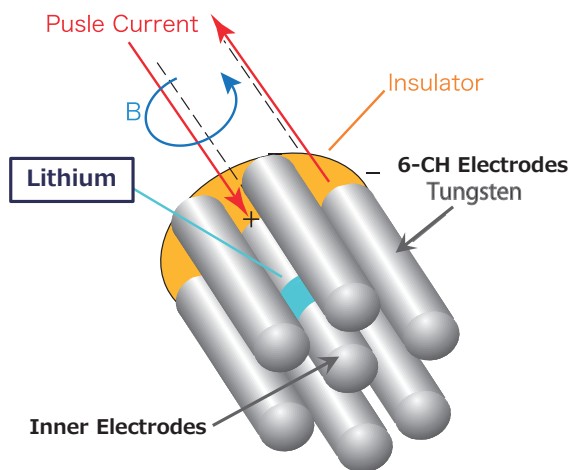


Fig. 1. Plasma focus device composed of 6-channel electrodes (one side).

### 3. Experimental Setup

Fig. 1 shows a schematic illustration of our plasma focus electrodes in EUV light source [7,8]. It is composed of an inner electrode and six outer electrodes which are placed on the circumference. Solid lithium was filled in grooves at the inner electrodes as the plasma source. Two sets of the focus electrodes were placed face to face in the counter facing plasma focus device.

Operational principle of the device is shown in Fig. 2. After the installation of the lithium filled electrodes, a high voltage is applied between the inner and the outer electrodes through 2x6-channel inductively isolated pulse power circuits. When a pulsed laser irradiates the lithium surface, the ablation lithium plasma triggers 2x6-channel discharges which produce two counter-facing initial plasmas around the inner electrodes. The two ring-shaped lithium plasmas are accelerated toward the tops of electrodes by the Lorentz force induced by the discharge current and the self-magnetic field.

The two ring plasmas are collided and heated at the center of inner electrodes. The converged plasma is radially compressed to a small sphere. Finally the plasma becomes a high temperature and high density state. When the discharge parameters are appropriate, an EUV light can be obtained from hydrogen like lithium ions in the high energy density plasma.

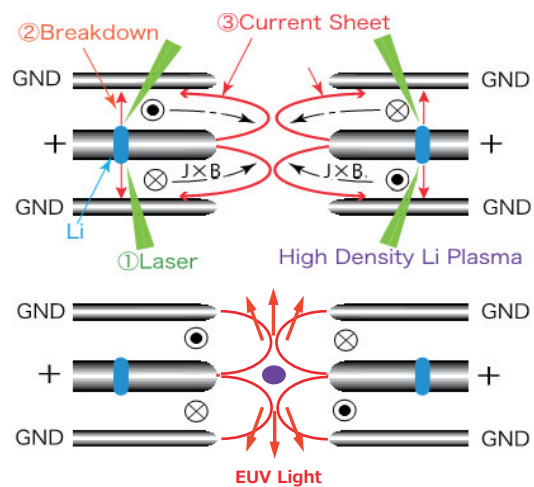


Fig. 2. Operational principle of counter-facing plasma focus device.

## 4. Results and Discussion

### 4.1 Characteristics of EUV Output

Fig. 3 shows typical waveforms of EUV emission and the discharge current. The EUV signal was obtained by a Zr-filtered EUV diode (AUXV 20HS1). As shown, the plasma discharge current had a quasi-sinusoidal waveform with its wavelength of about 2  $\mu\text{sec}$  and peak value of 2kA/channel. Note that the EUV light emission is observed during more than 1  $\mu\text{sec}$ .

The spectrum of the plasma radiation was measured with a grazing incidence spectrometer composed of a grating and a micro-channel plate (MCP). A typical (time-integrated) MCP image of the spectrum measurement is shown in the Fig. 4. As shown, a narrow peak was observed at 13.5nm. The spectrum line emission at 19.9nm is considered to be from He-like lithium ions and the lines at 15.5, 17.3 and 19.2nm were identified to be the light from contaminated oxygen ions [9].

The output energy was estimated by integrating the EUV waveform considering the transmission of the Zr-filter, the quantum efficiency and the effective solid angle of the diode. The results are shown in Fig.5, as a function of discharge voltage. As shown, the EUV energy per pulse increased almost proportionally to the voltage. As shown, the output energy reached more than 400 mJ/shot.

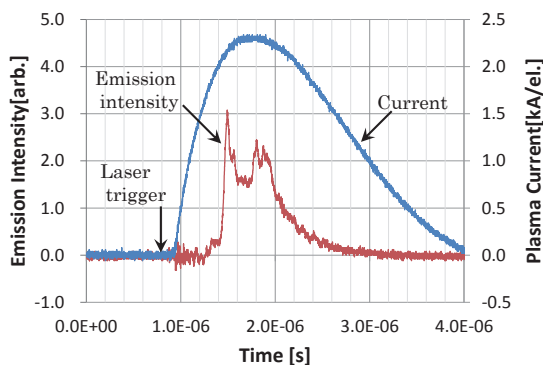


Fig. 3. Waveforms of EUV light emission by filtered photodiode and the discharge current.

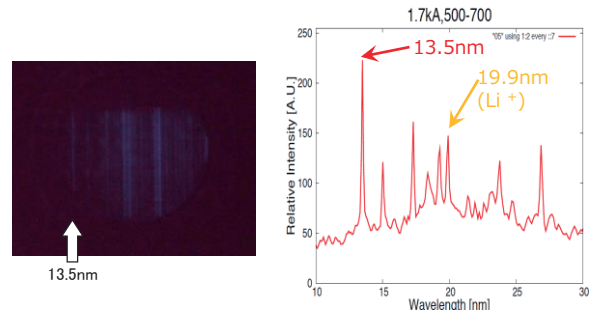


Fig. 4. MCP image (left) and its intensity profile during for 10-30nm in wavelength (right).

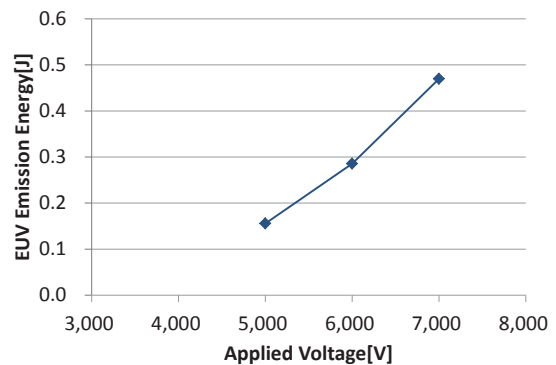


Fig. 5. EUV energy per shot as a function of applied voltage.

### 4.2 Characteristics of plasma dynamics

The size and the position of EUV light emitting area were observed by a pinhole camera, in which the radiation from the plasma was imaged on a CCD camera through a pinhole and reflections by two multi-layered Mo/Si mirrors. Then, only the region of in-band light emission was imaged on the CCD camera. The exposure time of CCD camera was about 1 msec, which is much longer than emission duration. Then the image was time-integrated during the discharge pulse.

Fig. 6 shows the photograph taken by the CCD camera around the gap between two inner electrodes. The estimated shapes of inner electrodes are shown in the dashed lines. The gap between the tips of inner electrodes was approximately 3 mm. As shown, the pinhole image revealed that the light emitting area located at the middle position of two inner electrodes.

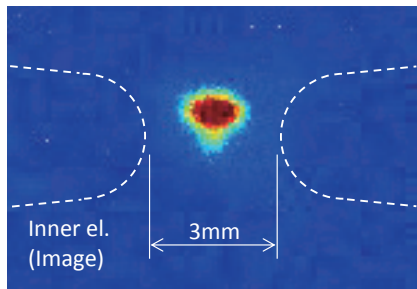


Fig. 6. Photograph taken by pinhole EUV-CCD camera around emission area between two inner electrodes.

By image analysis of this photograph, the half width of the EUV light emitting area was estimated to be about 1 mm.

In addition, plasma behavior was taken by high speed camera in the other experiments [10]. By this photography, laser irradiation to lithium, initial plasma generation, acceleration movement of the plasma, a collision between two plasma and plasma confinement are continually taken. Although the detail is left out, it is confirmed that the plasma behaves in the way as mentioned in the previous section.

## 5. Conclusions

An EUV light source using counter-facing plasma focus configuration was designed and tested.

Results of proof of principle experiments of the light source were as follows:

- The EUV emission duration prolonged more than  $\mu\text{sec}$ , which is, at least, ten times of conventional EUV sources.
- The energy output was more than 400 mJ/shot owing to the long emission time.
- Spectroscopic measurements revealed in-band line emissions from lithium ions and indicated also higher spectral purity than Sn-plasma based light sources.
- A time-integrated pinhole camera showed the size of EUV plasma is less than 1 mm.
- Images of plasma dynamics observed by the pinhole camera and a fast framing camera supported the operational principle discussed in

Sec.2.

Although a lot of works still remain including an improvement of laser triggering geometry, all of the experimental results indicated that the EUV device has potentiality as an efficient and high average power light source for the next generation lithography [10].

## Acknowledgements

The authors would like to express their sincere thanks to Drs. K. Uematsu, H. Nakai, and K. Shitara in IHI Corporation for their helpful advice and the encouragement on this study. They also thank M. Masuda, S. Liu, K. Kawaguchi, D. Nishii, K. Kanou, T. Kawasaki and S.Kittaka for their valuable supports during this study.

## References

- [1] M.W.McGeoch, "Pinch plasma EUV source with particle injection", *J. Phys. D: Appl. Phys.*, **Vol.37**, pp.3277-3284 (2004).
- [2] Banqiu Wu and Ajay Kumar: "Extreme ultraviolet lithography (A review)" *Journal of Vacuum Science & Technology B. Microelectronics and Nanometer Structures*, **Vol. 25**, No. 6, pp.1743-1761 (2007) .
- [3] V.M.Borisov, A.V.Eltsov, A.S.Ivanov, Y.B.Kiryukhin, O.B.Khristoforov, V.A.Mishchenko, A.V.Prokofoev, A.Yu.Vinokhodov, V.A.Vodchit, "EUV sources using Xe and Sn discharge plasmas", *J. Phys. D: Appl. Phys.* **Vol.37**, pp.3254-3265 (2004).
- [4] V.Y.Banine, K.N.Koshelev, G.H.P.M.Swinkels, "Physical processes in EUV sources for microlithography", *J. Phys. D: Appl. Phys.*, **Vol.44** (2011) 253001.
- [5] Y.Aoyama, M.Nakajima, K.Horioka, "Counter-facing plasma focus system as a repetitive and/or long-pulse high energy density plasma source", *Phys. Plasmas*, **Vol.16**, 110701 (2009).
- [6] M.Masnavi, M.Nakajima, A.Sasaki, E.Hotta, K.Horioka, "Potential of discharge-based lithium plasma as an extreme ultraviolet source", *Appl. Phys. Lett.*, **Vol.89**, No.3, pp.031503-1-031503-3 (2006).
- [7] H.Kuwabara, K.Hayashi, Y.Kuroda, H.Nose, K.Hotozuka, M.Nakajima, K.Horioka,

“Counter-facing plasma focus system as an efficient and long-pulse EUV light source”, *Proc. SPIE7969, Extreme Ultraviolet Lithography II*, **79692R** (2011).

- [8] T.Sodekoda, H.Kuwabara, M.Masuda, S.Liu, K.Kanou, K.Kawaguchi, K.Horioka, “Repetitive operation of counter-facing plasma focus device: toward a practical light source for EUV lithography”, *Proc. SPIE*, **9048**, Extreme Ultraviolet Lithography V, 9044824 (2014),
- [9] NIST (National Institute of Standard and Technology, US Department of Commerce) Atomic data base.
- [10] T.Sodekoda, S.Kurata, H.Kuwabara, T.Kawasaki, S.Kittaka, K.Horioka, “Laser assisted counter-facing plasma focus device as a light source for EUV lithography”, *IEEE Trans. Plasma Sci.*, (Submitted).

# Repetitive X-Ray Source by Triboluminescence

Seizo FURUYA

*Saitama Institute of Technology, Fukaya 369-0293 JAPAN*

## ABSTRACT

Triboluminescence is a luminous phenomenon resulted from friction; for example, peeling scotch tape, breaking rock sugar with a hammer, peeling mica and so on. Triboluminescence is well known over 50 years but in 2008 UCLA group reported the radiation of x-ray region by triboluminescence in vacuum for the first time. UCLA group made an automatic machine which peels scotch tape. With a view to practical application of triboluminescence to roentgen diagnosis we have attempted a new-type triboluminescence equipment.

## Keywords

triboluminescence, x-ray source, continuous operation

## 1. Introduction

Triboluminescence is a luminous phenomenon resulted from friction; for example, peeling scotch tape, breaking rock sugar with a hammer, peeling mica and so on. Triboluminescence is well known over 50 years but in 2008 UCLA group reported the radiation of x-ray region by triboluminescence in vacuum for the first time.<sup>1)</sup> UCLA group made an automatic machine which peels scotch tape. With a view to practical application of triboluminescence to roentgen diagnosis we made an automatic peeling machine similar to that of UCLA group. An x-ray tube for conventional roentgen diagnosis needs a high voltage power supply. In contrast, triboluminescence does not need it. So it is very useful for roentgen diagnosis to replace a conventional x-ray tube with triboluminescence.

So far, we have made an automatic peeling machine similar to that of UCLA group and have confirmed the visible light and x-ray emissions from the peeling tape. The visible light emission from peeling tape seems continuous by the naked eye but we have verified using a photomultiplier that the peeling tape emits light in pulses actually. At first, we have confirmed the x-ray generation from triboluminescence using a filtered phosphor screen when the parameters such as the followings are

changed; peeling speed, atmospheric pressure, variety of scotch tape, emission angle etc. Then in a similar way we have successfully measured the x-ray dose from triboluminescence using a portable dosimeter. It was found that the x-ray generation from triboluminescence has a directional property.

Because the method to peel scotch tapes does not enable to operate continuously, new method without scotch tapes has been proposed.<sup>2-3)</sup> The new method repeatedly contacts silicone with epoxy to produce x-ray. In this report, we have reported a novel method to generate x-ray radiation by triboluminescence. Two circular discs are contacted and rotated: One is made of silicone and another is made of epoxy.

## 2. Experimental Setup

We made an automatic peeling machine similar to that of UCLA group. Figure 1 shows a photograph of the machine. A geared motor of 200 RPM is used for a driving force.

Figure 2 shows the vacuum pump system. A turbo molecular pump (TMP) and a rotary pump (RP1) are a pair (PFEIFFER VACUUM, Turbomolecular Drag Pumping Station TSH261 with DUO2.5). The pumping speed of RP1 is 2.5 m<sup>3</sup>/h and total pumping speed is 210 L/s. To enhance the pumping capability RP2 (SHINKU KIKO, GVD-135A, 135 L/m) is

added.

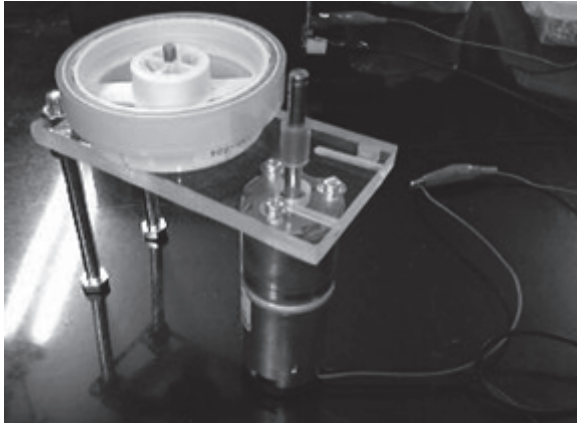


Figure 1 Photograph of automatic peeling machine

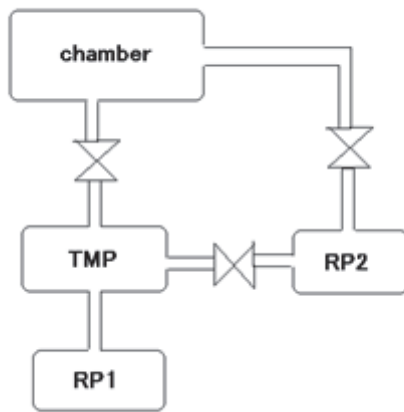


Figure 2 Vacuum pump system

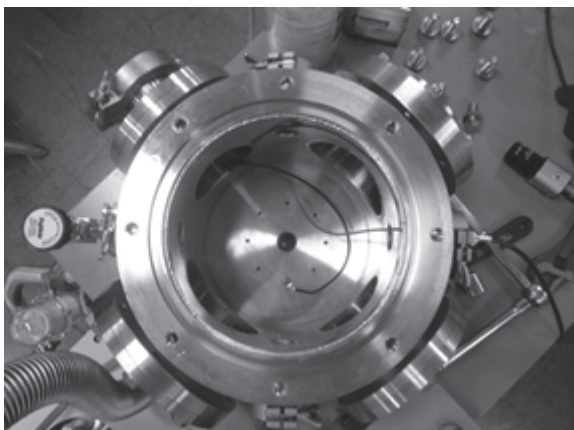


Figure 3 Photograph of vacuum chamber

Figure 3 shows a photograph of the vacuum chamber. The inner diameter is 210.7 mm and the inner height is 200 mm

### 3. Results and Discussion

#### 3.1 Confirmation of x-ray generation

A thin piece of plastic scintillator (OKEN, NE102A) was put near the peeling tape to confirm the generation of x-ray. In this report, a phosphor screen was used to detect the x-ray, as shown in Fig.4. The phosphor screen is PHOS-RP22SS-C5x5-R1000(Rugged) manufactured by Kimball Physics. Figure 5 shows an open-shutter photograph of emission of visible light from peeling tape and the phosphor screen in vacuum. The phosphor screen emits visible light when irradiated with x-ray, and it is found that the phosphor screen emits light in the photograph. The photograph was taken by turning off a room light and covering the vacuum chamber overall with a blackout curtain. Soon after peeling the tape, the pressure in the chamber started to increase. When the pressure was more than  $7 \times 10^{-3}$  torr, the plastic scintillator did not emit light. In this experiment, the pressure became  $1 \times 10^{-2}$  torr, balancing the outgas from peeling tape with the evacuation by vacuum pump. At that pressure, the phosphor screen still emits visible light.

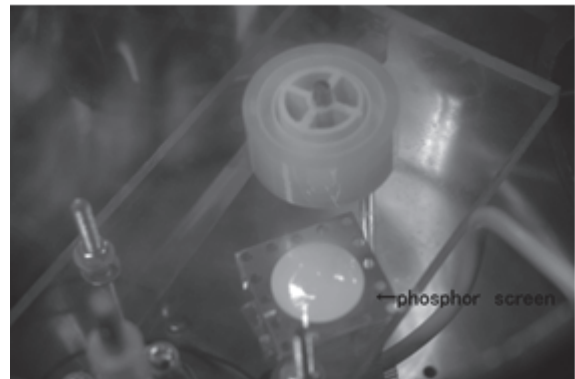


Figure 4 Experimental setup of phosphor screen

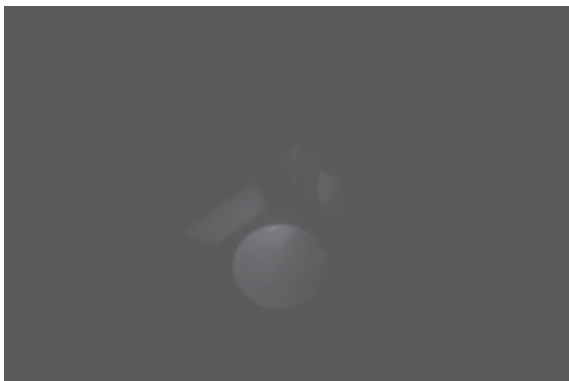


Figure 5 Photograph of light emission from peeling tape and phosphor screen

### 3.2 Measurement of x-ray dose

Figure 6 shows the experimental setup to measure the x-ray dose of upward direction. The x-ray dose was measured using a portable dosimeter (ALOKA, PDM-117). Figure 7 shows the time variation of pressure and accumulated x-ray dose. The dotted lines in the figure are the data in the case that the initial pressure was  $1.0 \times 10^{-3}$  torr and the peeling speed is 0.6-1.2 cm/s. The x-ray dose of  $1 \mu\text{Sv}$  was detected for 10-minute exposure. The broken lines are the experimental results in the case of  $7.8 \times 10^{-4}$  torr and 0.6-1.2 cm/s. When the initial pressure is low, the x-ray dose increases. When the peeling speed increases, the x-ray dose also increases? The continuous lines are the data in the case that the peeling speed is twice. The answer is no because the pressure rapidly increases.

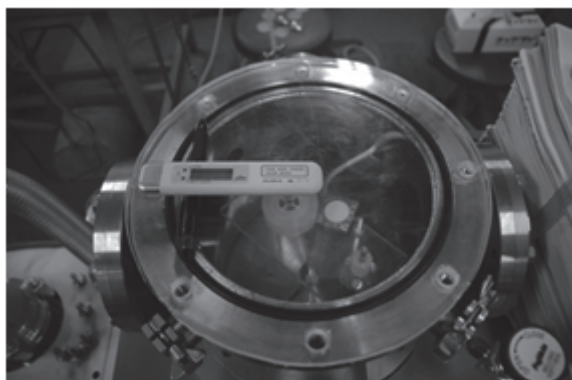


Figure 6 Experimental setup to measure x-ray dose of upward direction

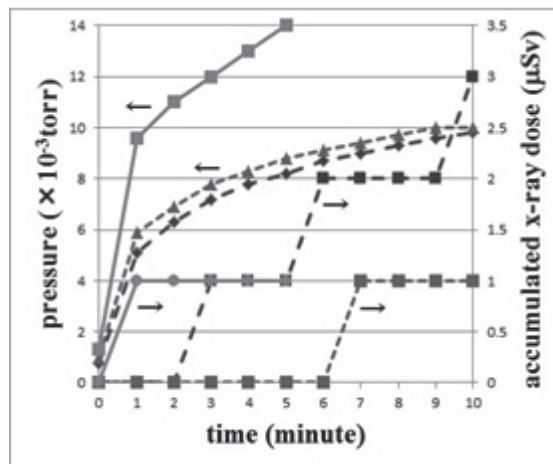


Figure 7 Time variation of pressure and accumulated x-ray dose

Figure 8 shows the experimental setup to measure the x-ray dose of traverse direction. The x-ray was not detected in this setup, so the x-ray was not radiated to the traverse direction.

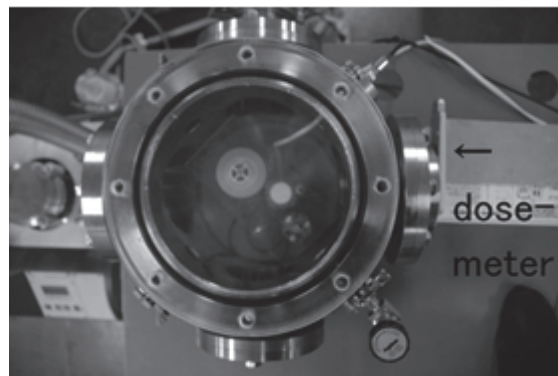


Figure 8 Experimental setup to measure x-ray dose of traverse direction

### 3.3 Continuous operation

As the method to peel scotch tapes does not enable to operate continuously, new method without scotch tapes has been proposed.<sup>2-3)</sup> The new method repeatedly contacts silicone with epoxy to produce x-ray. In this conference, we have reported a novel method to generate x-ray radiation by triboluminescence. Two circular discs are contacted and rotated: One is made of silicone and another is made of epoxy. We have made a new-type triboluminescence equipment, shown in figure 9.

From now on, we examine its characteristics when the following conditions are changed; combinations of contact materials, rotating velocity, radiation direction, pressure and so on.

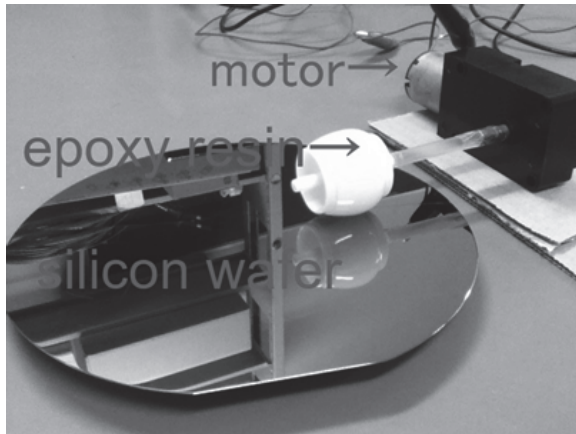


Figure 9 new equipment to generate x-ray continuously

#### 4. Conclusions

We have made a new-type triboluminescence equipment to generate x-ray continuously. From now on, we examine its characteristics in detail.

#### References

- [1] C. G. Camara et al., “Correlation between nanosecond X-ray flashes and stick-slip friction in peeling tape”, *nature* Vol.455 pp.1089-1092 (2008).
- [2] K. Stefan, “A stroke of X-ray”, *nature* Vol.473 pp.455-456 (2011).
- [3] J. R. Hird et al., “A triboelectric x-ray source”, *Appl.Phys.Lett.* 98, 133501 (2011).

# Development of Measurement Method for Warm Dense Matter toward Material Selection for Fast Ignition

Toru Sasaki, Takumi Ohuchi, Arata Watabe, Satoshi Sugimoto, Yuki Sugimoto,  
Kazumasa Takahashi, Takashi Kikuchi, Nob. Harada, Mayuko Koga\*,  
and Shinsuke Fujioka\*\*

*Nagaoka University of Technology*

*\*University of Hyogo*

*\*\*Osaka University*

## ABSTRACT

To survey the optimum materials for fast ignition, we have introduced approaches by using pulsed-power experiment. To evaluate the electrical properties of warm dense matter (WDM) for insulator as a diamond-like-carbon (DLC), we have developed exploding wire compression method by using pulsed-power discharge. The results show that the voltage and current waveforms with and without coating DLC are different after the wire ablation. From the absorption spectroscopic measurement, the DLC temperature is estimated to be 9000 K. We have developed a two-dimensional magnetohydrodynamics code for understanding process of the strong magnetic field. The results indicate that the electrical conductivity of wire affects the generated magnetic field distribution. From above experimental and numerical approaches, WDM properties are important to select material for fast ignition.

## Keywords

Warm Dense Matter, Alternative Fast Ignition, Diamond-like-carbon, Laser Capacitor Coil Target, Electrical Conductivity

## 1. Introduction

Critical to fast ignition [1] is the transport of the laser-generated fast electrons and their associated heating of compressed DT fuel. The coupling efficiency of laser energy to these fast electrons and the energy deposited in the fuel should be improved [2-5]. From the numerical results, the low-Z cone is expected to be the improvement of coupling efficiency, because the fast electrons are scattered by the large Coulomb potential of highly charged ions in high-Z cone wall [2]. The transport of fast electrons in the cone depends on the electrical conductivity of cone material, especially warm dense matter (WDM).

On the other hand, the fast electron is guided the

target by using strong magnetic field, which is order of several teslas, generated by a laser capacitor target [6]. The generated magnetic field using laser capacitor target depends on the coil materials [7,8]. To generate the strong magnetic field, we should consider the generation rate of fast electrons and the skin effect as an electrical conductivity for ablated plasma at the generation of the magnetic field. To understand its magnetohydrodynamic (MHD) behaviors, we proposed to evaluate the electrical properties using experimental observations and numerical simulation.

In this paper, to survey the optimum materials for fast ignition, we have introduced approaches by using

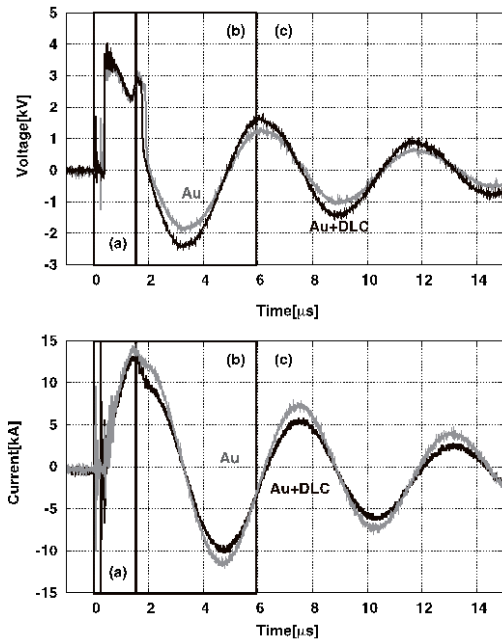


Fig. 1 Typical voltage and current waveforms for Au wire and Au wire +DLC pulsed-power experiment.

## 2. Exploding Wire Compression for Evaluating Electrical Conductivity in Warm-Dense Diamond-Like-Carbon

The diamond-like-carbon (DLC) [6] cone is promised to increase the coupling efficiency due to the reduction of stopping power in cone compared to the gold cone. However, materials in WDM state are in a complex area where the state is neither solid, conventional fluid nor ideal plasma. We propose a method to investigate the WDM properties of insulator by using pulsed-power discharges[9-14].

From above evaluations, the DLC cone [6], which is one of the low-Z cone, is promised to increase the coupling efficiency due to the reduction of stopping power in cone compared to the high-Z cone. The properties of DLC respects the diamond and the graphite, however, materials in WDM state are in a complex area.

To evaluate the electrical conductivity in DLC WDM, we propose a concept to investigate the WDM properties of insulator by using pulsed-power discharges. The concept of the evaluation of electrical conductivity for DLC WDM is a shock compression

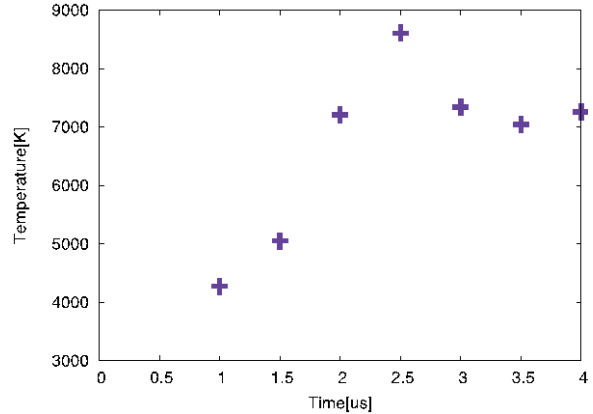


Fig. 2 Time-evolution of DLC temperature

driven by an exploding wire discharge with confined by a rigid capillary [9].

The WDM generation by using pulsed-power discharge is qualitative evaluation of the electrical conductivity and the other plasma parameters. However, the pulsed-power discharge is difficult to make the WDM for insulator. To evaluate the electrical conductivity for DLC WDM, the shock compression driven by an exploding wire discharge with confined by a rigid capillary is considered. The exploding wire has a huge ablation pressure approximately a few GPa. Thus, the pressure of exploding wire drives the shock heating for the insulator as the DLC membrane, which is coated on the wire. The heated DLC membrane state is observed by the emission spectrum for the temperature. The DLC membrane coated on the wire for gold was fabricated using RF plasma CVD.

Figure 1 shows a time-evolution of voltage and current. As shown in Fig. 1, observed voltage and current waveforms are same at the region (a). The region (a) means that the wire is heated up to vaporization. After the region (a), we can see that the voltage and current waveforms between Au wire and Au wire + DLC is difference because of the difference of the resistance. After the region (c), the capillary was broken by the expansion pressure and the wire/plasma behaves free expansion.

Figure 2 shows a time-evolution of DLC temperature, which is observed by the inversed line-pair method. As shown in Fig. 2, the DLC temperature estimated by the absorption spectrum is

up to 9000 K. It means that the warm dense DLC is generated by using proposed method. The electrical conductivity of DLC plasma is roughly estimated to be  $10^6$  S/m incorporating hydrodynamic simulation. To determine the correct electrical conductivity of DLC plasma, we should measure the DLC or the wire/plasma size.

### 3. Magnetohydrodynamic Behavior of Laser Capacitor Target

The fast electrons are transported with the strong magnetic field, which is order of several teslas, generated by a laser capacitor target [6]. The generated magnetic field using laser capacitor target depends on the coil materials [7,8]. The generated magnetic field should be considered the generation rate of fast electrons and the skin effect as an electrical conductivity for ablated plasma at the generation of the magnetic field. To understand its MHD behaviors and the electrical properties, we proposed to evaluate experimental observations and numerical simulation [15].

To understand its MHD behaviors and the electrical properties, we proposed to evaluate both

experimental observations and numerical simulation. Electrical conductivity for nickel in warm dense matter (WDM) state has been measured with an exploding wire in a quasi-isochoric vessel. To understand the MHD behavior in the laser capacitor target, a two-dimensional MHD simulation has been also demonstrated.

To understand the dependence of generated magnetic field on electrical conductivity distribution in matter, the MHD of single tune coil in the capacitor-coil target with two-dimensional cylindrical geometry has been calculated. The simulation is not incorporated the experimental results. The MHD behavior of capacitor-coil target is solved by conventional MHD equations. The magnetic pressure in the equation of motion was neglected because the kinetic pressure of the plasma was higher than the magnetic pressure.

The wire material, which is determined the equation of state and the transport properties, is aluminum. Coil and wire diameters of the capacitor-coil target at the initial condition were set to be  $550 \mu\text{m}$  and  $50 \mu\text{m}$ , respectively. The electrical conductivity in vacuum region is set to be  $10^{-5}$  S/m.

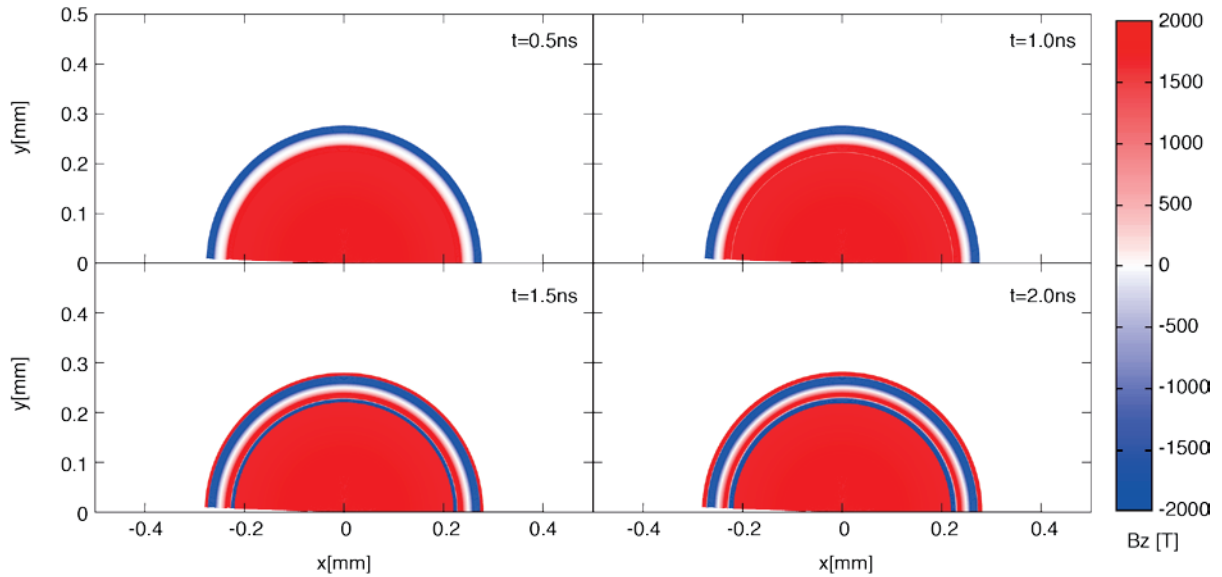


Fig. 3 Time-evolutions of  $B_z$ -field profile in x-y plane, which is calculated using constant electrical conductivity for the wire.

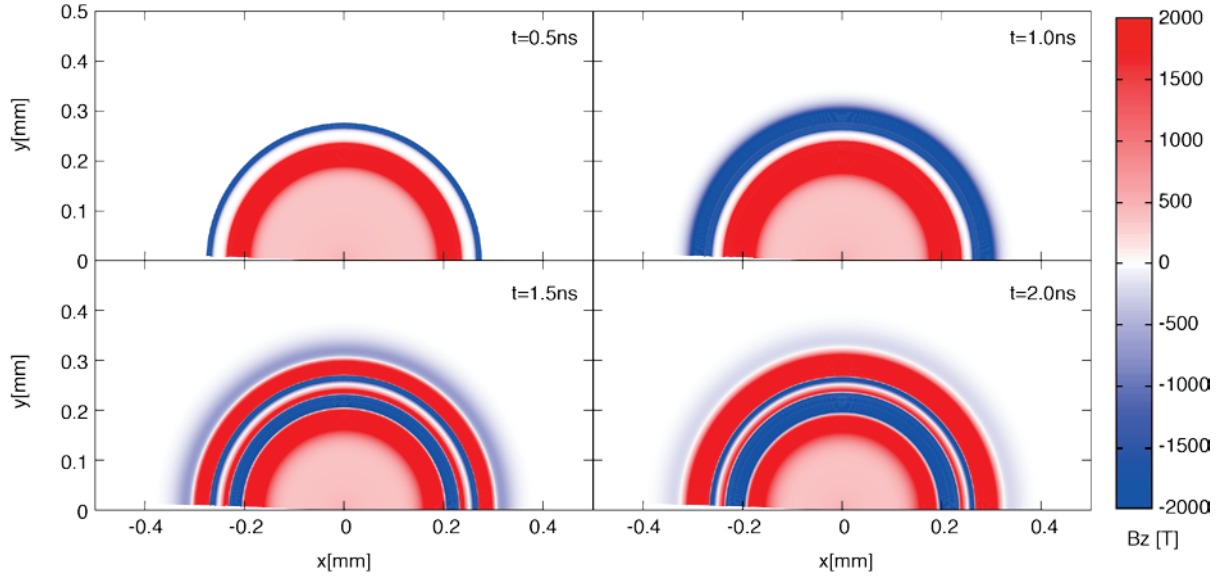


Fig. 4 Time-evolutions of  $B_z$ -field profile in x-y plane, which is calculated using Lee-More model [16] for the wire.

The capacitor-coil target during the irradiation of intense laser behaves like a current source. The maximum interior magnetic flux density of capacitor-coil coil is approximately 1.5 kT. From the results, to simplify the current evolution  $I(t)$ , we have set sinusoidal wave form with 4 MA of maximum current and 500 MHz of frequency. The displacement current was also neglected since the propagation time of the electromagnetic wave from the inner wire surface to the center of the coil was estimated to be 1 ps. The typical timescale of MHD motion is longer than that of the electromagnetic wave. The timescale in the MHD simulation is ensured.

Figure 3 shows the time-evolutions of  $B_z$ -field profile, which is calculated using constant electrical conductivity for the wire. The electrical conductivity of wire is set to be  $10^5$  S/m. The results shows that  $B_z$ -field in the coil is almost uniform until  $t=1$  ns. After  $t=1$  ns, the isolated reversal  $B_z$ -field is observed. However, the  $B_z$ -field at the center of coil is positive until  $t=2$  ns.

Figure 4 shows the time-evolutions of  $B_z$ -field profile, which is calculated using Lee-More model [16] for the wire. The results indicated that  $B_z$ -field in the coil using Lee-More model is rather small compared to that using constant conductivity model. Because the electrical conductivity of wire using

Lee-More model is  $10^6$  S/m, the B-field diffuses into the coil. However, it is noted that the spatial-temporal distribution of B-field depends on the total current in the coil. Thus, the equivalent circuit model for capacitor-coil target or the total current into the coil will be included the simulation model.

#### 4. Conclusions

To survey the optimum materials for fast ignition, we have introduced approaches by using pulsed-power experiment.

To evaluate the electrical conductivity in DLC WDM, we propose a concept to investigate the WDM properties of insulator by using pulsed-power discharges. The concept of the evaluation of electrical conductivity for DLC WDM is a shock compression driven by an exploding wire discharge with confined by a rigid capillary.

To understand the MHD behavior and electrical properties of the laser-capacitor target we have evaluated by experimental observations and numerical simulations. Electrical conductivity for nickel in WDM state has been measured with the exploding wire in the quasi-isochoric vessel. The result shows that the electrical conductivity for nickel in WDM is relatively high from the comparison of the electrical conductivities for several materials in

WDM state. However, the skin effect in the capacitor-coil target will be neglected from the estimation. A two-dimensional MHD simulation for capacitor-coil target has been demonstrated. The results show that the distribution of B-field in the capacitor-coil target depends on the electrical conductivity model.

From above experimental and numerical approaches, WDM properties are important to select material for fast ignition.

## References

- [1] R. Kodama, *et. al.*, Nature, **412**, 798 (2001).
- [2] T. Johzaki, *et. al.*, Nuclear Fusion, **51**, 073022 (2011).
- [3] P. McKenna, *et. al.*, Physical Review Letters, **106**, 185004 (2011)
- [4] A. J. Kemp, *et. al.*, Nuclear Fusion, **54**, 054002 (2014)
- [5] A. P. L. Robinson, *et. al.*, Nuclear Fusion, **54**, 054003 (2014)
- [6] S. Fujioka, *et. al.*, Plasma Physics and Controlled Fusion, **54**, 124042 (2012).
- [7] S. Fujioka, *et. al.*, Scientific Reports, **3**, 1170 (2013)
- [8] J. J. Santos, *et. al.*, New Journal of Physics, **17**, 083051 (2015)
- [9] T. Sasaki, *et. al.*, Journal of Physics; Conference Series, **688**, 012102 (2016)
- [10] Y. Amano, *et. al.*, Review of Scientific Instruments, **83**, 085107 (2012)
- [11] T. Sasaki, *et. al.*, Physics of Plasmas, **17**, 084501 (2010)
- [12] D. Sheftman and Y. E. Krasik, Physics of Plasmas, **17**, 112702 (2010)
- [13] T. Sasaki, *et. al.*, Laser and Particle Beams, **24**, 371 (2006)
- [14] I. Krisch and H. J. Kunze, Physical Review E, **58**, 6557 (1998)
- [15] T. Sasaki, *et. al.*, Journal of Physics; Conference Series, **717**, 012078 (2016)
- [16] Y. T. Lee and R. M. More, Physics of Fluids, **27**, 1273 (1984)

# Investigation of Basic Properties of a Fullerene Ion Source Using Sublimation and Electron Attachment

K. Nakamura, E. Baba, J. Hasegawa, T. Kawamura and K. Horioka  
*Department of Energy Science, Tokyo Institute of Technology*

## Abstract

This article reports basic properties of a prototype fullerene ion source that is being under development at Tokyo Tech. We adopt a sublimation electron irradiation method to ionize  $C_{60}$  and successfully obtain a 1.6-nA negative fullerene beam. The results suggest that irradiated electron energy has a key to improve the ionization efficiency of fullerene.

## 1 Introduction

The cluster, an aggregate of several to several million atoms or molecules, has been attracting much attention during the last two decades. There are various types of clusters depending on constituent atoms and bonding structures. In particular,  $C_{60}$  fullerene, which has a soccer-ball-like structure composed of sixty carbon atoms, is the most famous one. A lot of studies on the fullerene have been conducted since its discovery by Kroto in 1985 [1] and the establishment of the industrial mass production method in 1990.

One of the most successful applications of the cluster is time-of-flight secondary-ion mass spectrometry (TOF-SIMS) with a  $C_{60}$  primary ion beam [2]. The use of  $C_{60}$  drastically enhanced secondary-ion emission efficiency compared with the case using monoatomic ions. The kinetic energy of  $C_{60}$  ions in this application is typically 10 keV, so they interact only with the sample surface. On the other hand, the induction microtron was recently proposed to accelerate large cluster ions having low specific charges to much higher energies than ever achieved [3]. This new type accelerator will enable us to investigate the interaction of energetic clusters with bulk solid materials.

To supply a large amount of fullerene ions to the accelerator, the ion source need to adopt an efficient ionization scheme. The ionization of fullerene has been investigated by electron impact ionization for generation of relatively low charge-state fullerene ions [4, 5] and multi-photon ionization for higher charge-state ions [6]. However, the ionization of fullerene has not been investigated in terms of efficient ion supply to the accelerators.

The purpose of this study is to develop a fullerene ion source that can supply a high-current fullerene ion beam and examine its basic properties. The ion source uses a sublimation and elec-

tron irradiation method for ionization of fullerene. This method allows us to produce both positive and negative ions by controlling the kinetic energy of irradiated electrons. When the electron energy is lower than approximately 10 eV, negative fullerene ions are formed by electron attachment [4]. With electron energy more than 10 eV, positive fullerene ions are formed by electron impact [5]. This article reports experimental results on basic properties of the fullerene ion source that we originally developed at Tokyo Tech.

## 2 Experimental Setup

Figure 1 shows a schematic of the test bench of the fullerene ion source. The ion source components are installed in a vacuum chamber evacuated down to  $10^{-5}$  Pa. Commercially available fullerene powder is contained in an oven and heated up to  $500^\circ\text{C}$  to obtain fullerene gas through a nozzle. Elec-

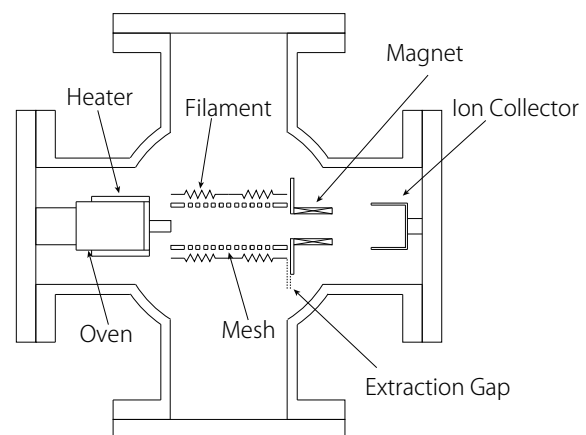


Figure 1: A schematic of the test bench of the fullerene ion source.

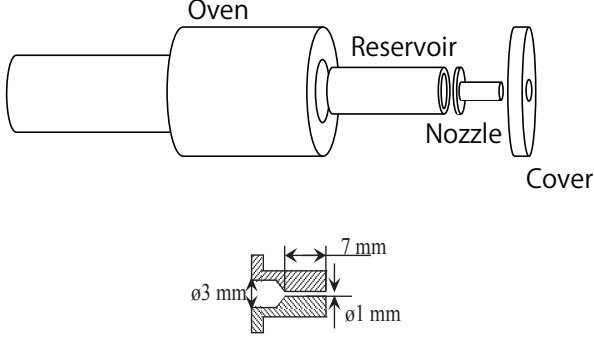


Figure 2: Inner structure of the sublimation component (upper) and cross-sectional view of the nozzle (lower).

trons emitted from tungsten filaments are accelerated by biased mesh electrodes and introduced to the space where the evaporated fullerene gas flows downstream. Fullerene molecules are irradiated by the incoming electrons and negatively ionized by electron capture reactions. The fullerene ions are extracted by an extraction voltage of typically 1 kV and detected by a Faraday cup. Electrons are also extracted at the same time, but they are suppressed by a transverse magnetic field applied just after the gap.

The sublimation component consists of an oven, a reservoir, and a nozzle. Figure 2 shows the inner structure of the sublimation component and the cross section of the nozzle. To heat the oven, we used a commercially available band-heater. The maximum operation temperature of the heater is 760 °C. All parts except for the heater are made of brass. Fullerene powder in the reservoir is heated up to a temperature of  $\sim 450$  °C typically. Fullerene molecules evaporates and flows into the ionization section through the nozzle. The flow rate of the fullerene vapor is regulated by the oven temperature and the nozzle conductance. The flow rate  $Q$  of fullerene vapor is given by

$$Q = C \times P, \quad (1)$$

where  $C$  is the nozzle conductance and  $P$  the vapor pressure of fullerene. Assuming the molecular flow, the conductance  $C_m$  is given by

$$C_m = \frac{2\pi a^3 v}{3L}, \quad (2)$$

where  $a$  is the nozzle diameter,  $L$  the nozzle length, and  $v$  the averaged thermal velocity of fullerene molecules. On the other hand, the conductance of viscous flow  $C_v$  is given by

$$C_v = \frac{\pi a^4 P}{16\eta L}, \quad (3)$$

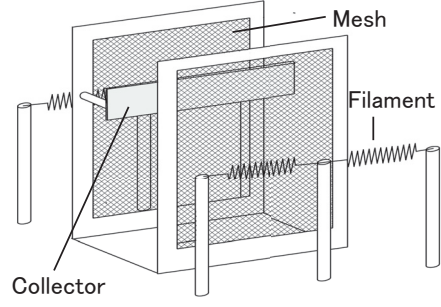


Figure 3: An illustration of the ionization component.

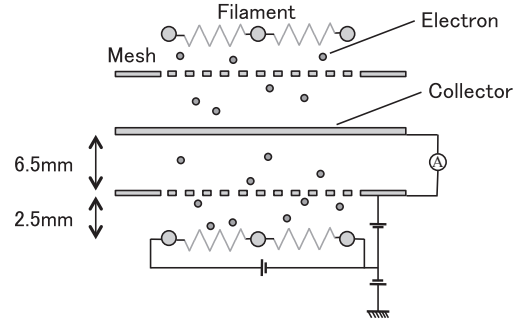


Figure 4: Circuit diagram of the ionization component.

where  $\eta$  is the coefficient of viscosity. We estimate the amount of consumption of fullerene from the difference of the reservoir weight before and after the operation.

Figure 3 illustrates the ionization component. The ionization component consists of four tungsten filaments and two counter-facing mesh electrodes made of stainless steel. The electron current density emitted from the filament is described by the Richardson-Dashman's equation,

$$J_{RD} = \frac{4\pi m e k^2 T^2}{h^3} \exp\left(-\frac{\phi}{kT}\right), \quad (4)$$

where  $m$  is the mass of electron,  $e$  the elementary charge,  $k$  the Boltzmann constant,  $h$  the Planck constant,  $T$  the temperature of filament, and  $\phi$  the working function. As shown in Eq. (4), the electron current is proportional to the square of the filament temperature. Thermal electrons from the filaments are accelerated up to 18 eV by the biased mesh electrodes and introduced to the space between the electrodes, where the fullerene vapor flows. In evaluating the electron flux usable for the ionization of fullerene, a charge collector (10 mm  $\times$  40 mm) was mounted on the fullerene beam axis.

The circuit diagram of the ionization component

is shown in Fig. 4. The distance between the filament and the mesh electrode is 2.5 mm, and the distance between the mesh electrodes is 13 mm. Because both the filaments and the mesh electrodes are biased with respect to the ground potential, fullerene ions generated between the electrodes are accelerated downstream.

### 3 Results and Discussion

Figure 5 plots the flow rate of fullerene vapor as function of the oven temperature. The flow rate increases with increasing oven temperature. In particular, it increases remarkably when the oven temperature exceeds approximately 400 °C. Solid lines in the figure show the calculated flow rates assuming molecular flow conductance  $C_m$  and viscous flow conductance  $C_v$ . The measured flow rates above 400 °C almost coincide with the calculated ones, indicating that the fullerene vapor behaves as viscous flow in the nozzle in this temperature regime.

Figure 6 shows electron current densities measured as a function of mesh electrode voltage for filament voltages of 25, 30, and 35 V. The electron current density increases both with increasing mesh electrode voltage and with increasing filament input power. Since no saturation is observed in the electron current density even with the highest filament voltage (35 V), there is a room for increasing electron current density by increasing filament input power.

In the present study, we performed an experiment on the production of fullerene negative ions. Time evolutions of the oven temperature and the negative ion current measured by the Faraday cup are shown in Fig. 7. An ion current drastically increases when the oven temperature exceeds approximately 300 °C, which indicates that the sublimation of fullerene begins around this temperature. Thus, the observed negative current is ob-

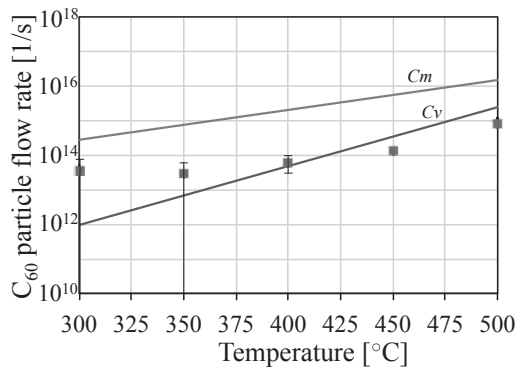


Figure 5: Fullerene vapor flow rate as a function of oven temperature.

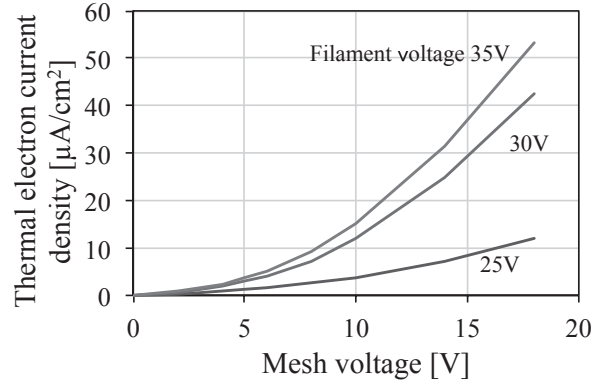


Figure 6: Dependencies of electron current density on mesh electrode voltage and filament voltage.

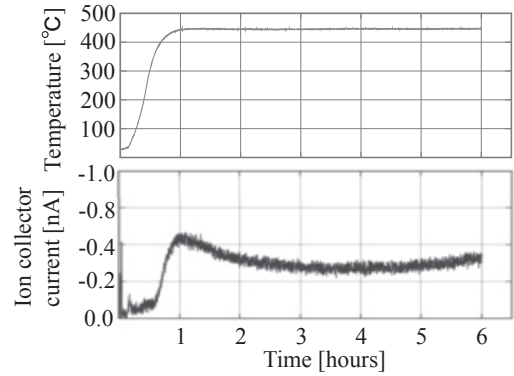


Figure 7: Time evolutions of oven temperature and negative ion current in a typical operation.

viously attributed to fullerene vapor. However, there still remains the possibility that we observed the negative ions originating from fragments of fullerene molecules.

The negative ion current flowing into the ion collector was measured as a function of the mesh voltage for different filament voltages from 25 to 35 V as shown in Fig. 8.

We obtained a maximum negative ion current of 1.6 nA at a filament voltage of 35 V and a mesh voltage of 18 V. The irradiated electron energy is determined by the mesh voltage. It is quite curious that negative ion current continues to increase when the electron energy increases beyond 10 eV. Since the cross section of electron attachment to a fullerene drops sharply for electron energies above 10 eV, there is almost no chance for primary electrons to attach fullerene molecules. To explain this result, we need to additional processes such as secondary electron attachment.

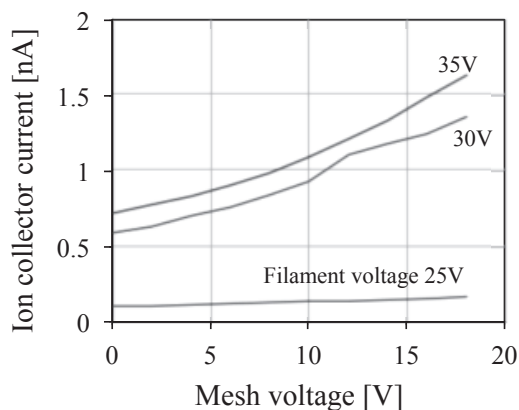


Figure 8: Dependencies of negative ion current on mesh electrode voltage and filament voltage.

#### 4 Concluding remarks

This article reported basic properties of a prototype fullerene ion source using sublimation and electron irradiation. We successfully obtained 1.6-nA negative ion beam current from the fullerene ion source. The ion beam current was found to depend not only on the fullerene vapor flow rate but on the energy of irradiated electrons. In particular, electrons having an energy higher than 10 eV obviously contribute to the enhancement of the negative ion current, which implies that the secondary electrons generated by electron impact ionization of fullerene causes negative ion production.

#### References

- [1] H. W. Kroto, J. R. Heath, S. C. O'Brien, R. F. Curl, and R. E. Smalley, "C60 Buckminsterfullerene", *Nature*, **318**, 162 (1985).
- [2] D. Weibel, *et al.*, "A C60 Primary Ion Beam System for Time of Flight Secondary Ion Mass Spectrometry: Its Development and Secondary Ion Yield Characteristics", *Analytical Chemistry*, **75** (7), 1754-1764 (2003).
- [3] K. Takayama, *et al.*, "Racetrack-shape fixed field induction accelerator for giant cluster ions", *Phys. Rev. STAB*. **18**. 050101 (2015).
- [4] S. Matt, *et al.*, "Absolute partial and total cross-section function for the electron impact ionization of C60 and C70", *Journal of Chemical Physics* **105**, 1880 (1996).
- [5] T. Jaffke, "Formation of C60<sup>-</sup> and C70<sup>-</sup> by free electron capture. Activation energy and effect of internal energy on lifetime", *Chemical Physics Letters* **226**, 213-218 (1994).

- [6] V. R. Bhardwaj *et al.*, "Internal Laser-Induced Dipole Force at Work in C60 Molecule", *Physical Review Letters* **91**, 203004 (2003).

# Study of laser ablation induced shock waves in a low-pressure gas using a probe-beam-deflection technique

Rimpei Chiba<sup>1</sup>, Yuta Ishikawa<sup>2</sup>, Jun Hasegawa<sup>2</sup>, and Kazuhiko Horioka<sup>2</sup>

<sup>1</sup>Department of Mechano-Aerospace Engineering, Tokyo Institute of Technology,

<sup>2</sup>Department of Energy Sciences, Tokyo Institute of Technology.

## ABSTRACT

We investigated the temporal evolution of shock wave generated by pulsed laser ablation of an aluminium target as a function of background gas pressure using a probe beam deflection technique. By using this technique, we succeeded in detecting shock waves even in a thin gas with a pressure down to 200 Pa. The result showed that, at early times, the laser ablation induced shock wave propagates faster as the ambient gas pressure decreases, but it attenuate with time and gradually approaches to a wave propagating at sound speed which is independent of gas pressure. The correlation between the shock waves' transit time and the distance from the target surface was in good agreement with the ideal spherical blast wave model when the background gas pressure was relatively low. The theoretical model predicted that the kinetic and thermal energy of the blast wave was an order smaller than the incident laser energy, which indicate that most of the laser energy was reflected at the target surface and/or used to vaporize, excite, and ionize the target material atoms.

## Keywords

Key Words: Puled laser ablation, Shock wave, Low-pressure gas, Probe beam deflection

## 1 Introduction

Studies of pulsed laser ablation in tenuous gas has received considerable attention due to its importance in numerous fileds such as cluster production, pulsed laser deposition, micro-machining, and laser propulsion. In the case of cluster production, background gas surrounding the target is used to confine and cool the ablated species [1] [2], while in pulsed laser deposition, the ambient gas is introduced as a moderator [3].

When a high power pulsed laser irradiates a target material, the target material evaporates and forms a hot dense plasma so-called laser ablation plume. The created plume expands and drifts in the direction perpendicular to the target's surface with a supersonic speed. The plume receives drag forces from the surrounding gas and therefore the expansion attenuates and finally ceases when the plume pressure becomes equal to the background pressure. On the other hand, the ambient gas receives driving force from the expanding plume and forms a shock wave. The time evolution of the laser induced shock wave at early stages can be predicted analytically using the ideal point explosion blast wave model [4]. The behavior of the laser ablation plume and the shock wave propagating ahead

strongly depends on the surrounding gas pressure, the laser energy density, the laser beam spot size, and the properties of the background gas and the target material.

A number of scientists have already investigated the propagation of shock waves using various optical measurement methods such as shadowgraphy [5] [6], schlieren imaging [7] [8], interferometry [9], and probe beam deflection methods [10] [11] [12] [13]. As for low density background gas, it is difficult to distinguish the shock front with photographing techniques since the sensitivity of these flow visualization techniques is determined by the contrast of the images [14]. Accordingly, we adopted the probe beam deflection technique. Unlike photography, the probe beam deflection method cannot measure the spatial density distribution at once, but instead, it enables us to determine the transit time of the shock wave even at low background pressure [13].

The purpose of this research is to quantitatively clarify the background pressure effect on the laser induced shock wave. By utilizing the probe beam deflection technique, we succeeded in measuring the transit time of the propagation of shock wave generated by laser ablation of an aluminium target at different gas pressures ranging from 200 to  $10^5$

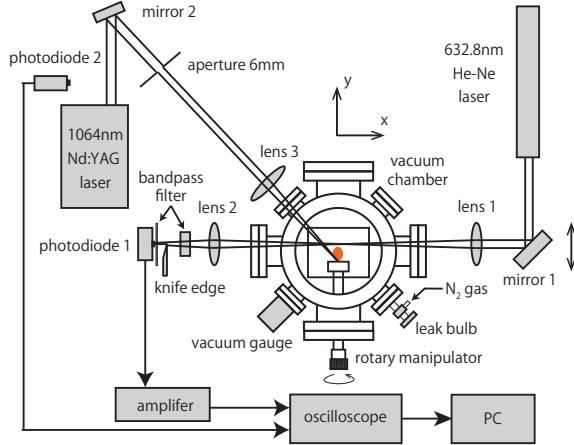


Figure 1: Schematic diagram of the experimental setup.

Pa. The ideal point explosion blast wave model was used to describe the propagation of the shock wave in the early expansion stages, and to estimate the energy conversion rate from the laser to the hydrodynamic energy. The result presented in this paper would give us valuable information for applications, which make use of pulsed laser ablation in rare ambient gas.

## 2 Experimental setup

A diagram of the experimental setup is shown in figure 1. A Q-switched Nd:YAG laser (wave length 1064 nm, pulse duration FWHM 6 ns, laser energy  $151.8 \pm 1.8$  mJ (means  $\pm$ s.d.)) was used to create an aluminium plasma plume. The laser energy was measured ten times using an energy meter (OPHIR, 10A-P) before starting each series of experiment. A disk-shaped aluminium target was placed in a stainless-steel vacuum chamber, which was filled with inert nitrogen gas at room temperature. The laser was focused onto the target by a planoconvex lens ( $f=300$  mm) at an incident angle of 35 degree. The measured diameter of the laser beam spot on the target surface was 1.7 mm (power density  $1.1 \times 10^9$  W/cm<sup>2</sup>). For every 20 shots, the target was rotated and the contamination of the aluminium surface was removed by laser ablation in order to keep reproducibility. A probe laser beam (He-Ne laser; wave length 632.8 nm, power 10 mW) was introduced to the vacuum chamber in the direction parallel to the sample surface and focused onto a point on the plume expansion axis by lens1 ( $f=250$  mm). The focal spot has a finite size (0.5 mm FWHM) because of the emittance of the laser beam. The measured intensity distribution at the focal spot was well represented by Gaussian. Subsequently the probe beam

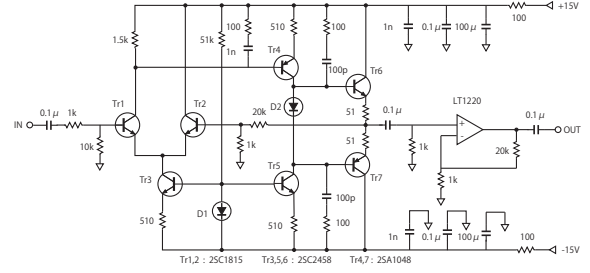


Figure 2: Circuit diagram of the amplifier.

is refocused on a Si PIN photodiode1 (Hamamatsu, S5972) by another planoconvex lens2 ( $f=40$  mm) after passing through two narrowband bandpass filters ( $632.8 \pm 10$  nm). These bandpass filters largely attenuate the stray light from the ablation laser and plasma-plume. A knife edge was located between the photodiode1 and lens2 in order to block a half of the probe beam. The position of the knife edge in the direction perpendicular to the beam was adjusted finely by a micrometer.

When the shock wave pass through the probe beam, the probe light deflects due to the density gradient of the wave. The deflection angle  $\theta$  is expressed as [14]

$$\theta = \int_{path} \left( \frac{K(\lambda)}{n} \frac{\partial \rho}{\partial y} \right) dx, \quad (1)$$

where  $K(\lambda)$  is the Gladstone-Dale constant, which depends on the probe-beam wavelength,  $n$  is the refraction index of the ambient gas, and  $\rho$  is the gas density. As for our experimental setup, negative values of density gradient in the  $y$  direction cause beam deflection toward the target surface, resulting in a decrease in the intensity measured by the photodiode, while positive density gradient account for an increase in the signal intensity of the photodiode. If the displacement of the light spot at the knife edge is very small compared to the spot diameter, we can assume that the change of the probe beam intensity at the photodiode is proportional to the deflection angle (thus proportional to the density gradient in the  $y$  direction). Based on this assumption, we can roughly consider the alternative component of the obtained voltage signal  $\tilde{V}(t)$  as

$$\tilde{V}(t) \propto \int_0^L I(y) \frac{\partial \rho(y,t)}{\partial y} dy, \quad (2)$$

where  $I(y)$  is the intensity distribution of the probe beam at the focal spot above the target (Gaussian), and  $L$  is the length of the test section.

The scattered light from the laser pulse was monitored with photodiode2 (Hamamatsu, S5972) and

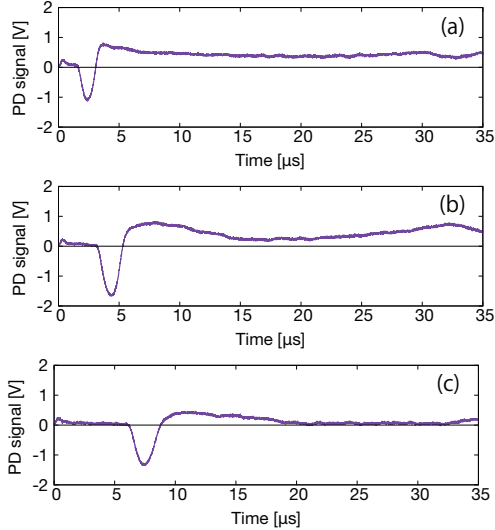


Figure 3: Typical probe light deflection signals measured at a background pressure of 100 kPa. The distances from the target surface are (a) 2.4 mm, (b) 3.5 mm, (c) 5.0 mm.

used as a trigger. The transit time of the shock front was estimated by comparing the signals obtained from the two photodiodes. The entire optical system (mirror1, lens1, lens2, bandpass filters, knife edge, photodiode1) can be moved in the  $y$  axis direction with a spatial resolution of  $50 \mu\text{m}$ , which allows us to measure the shock wave transit time at various distances from the target.

It is very important to enhance the sensitivity of the detection device in order to measure shock waves propagating through tenuous gas, since the density gradient of the flow is proportional to the background pressure. We therefore developed an optimum high-gain amplifier based on discrete op-amps to sensitively detect small signals from the photodiode. The circuit diagram of the amplifier is shown in figure 2. This circuit amplifies weak voltage signals approximately 750 times in a frequency range of  $10 \text{ kHz} \sim 1 \text{ MHz}$ . The output from the amplifier was coupled to a 300 MHz digital oscilloscope (Tektronix, TDS3034B). We acquired 16 waveforms under each experimental condition and averaged them to reduce random noises as well as occasional errors.

### 3 Results and discussion

A series of typical deflection signals of laser induced shock wave monitored at different distances away from the target surface are shown in figure 3. As is described in the preceding section, the amount of signal change, which is proportional to the convolution integration of the probe beam energy distribution and the density gradient distribu-

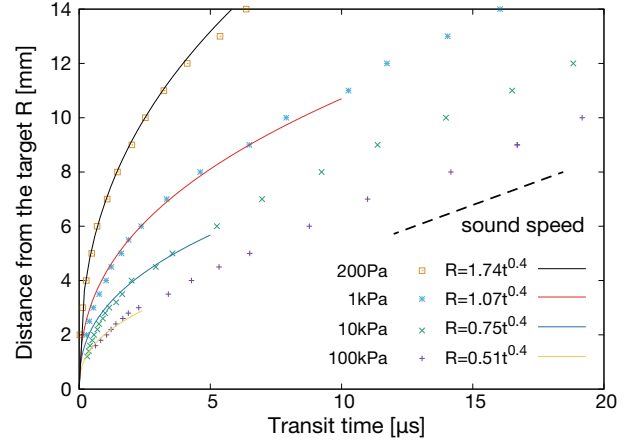


Figure 4: Temporal evolution ( $R - t$ ) of the shock front positions at different background gas pressures,  $P=100 \text{ kPa}$ ,  $10 \text{ kPa}$ ,  $1 \text{ kPa}$ ,  $200 \text{ Pa}$ . The symbols represent experimental data points and the solid curves represent the predictions by the spherical blast wave model. The slope of the dashed line represent the sound of speed (353 m/s of nitrogen gas at room temperature).

tion, will occur during the passage of a shock wave. The first negative peak results from the negative density gradient of the shockfront and the following positive peak owes to the gradual density slope at the back of the shockfront. From these signals, we estimated the transit time of the shock wave.

Figure 4 shows the time evolutions of the laser-generated shock waves observed at different surrounding gas pressures. In our present experimental set-up, background gas pressure at 200 Pa was the lowest pressure that we could clearly detect the passage of a shock wave. In this case, the mean free path of the gas particles is estimated to be  $\sim 10 \mu\text{m}$ , in which the gas can be still regarded as a continuum fluid. In the early stage of shock wave propagation ( $\leq 5 \mu\text{s}$ ), the shock speed depends on the background pressure and increases with decreasing gas pressure. Then it decreases with time and gradually approaches to the speed of sound (353 m/s for nitrogen gas at room temperature), which is represented as the slope of the dashed line in figure 4.

The experimental results were compared with the ideal spherical blast wave model expressed as [4]

$$R(t) = \varepsilon \left( \frac{E_0}{\rho_b} \right)^{\frac{1}{5}} t^{\frac{2}{5}}, \quad (3)$$

where  $E_0$  is the amount of energy released during the explosion,  $\rho_b$  is the background gas density, and  $\varepsilon$  is a dimensionless quantity that depends on the

specific heat ratio (in our case,  $\varepsilon=1.015$ ). This theory is based on an assumption that the mass of the energy source is negligible and the speed of shock front is much higher than the speed of sound (or the pressure behind the shock front is much higher than the external gas pressure). Thus we fitted Eq. (1) only to the data points in the early expansion stages where the shock speed is larger than the speed of sound. As shown in figure 4, the theoretical curves agree well with the experimental data especially for lower background gas pressure cases. This result shows that strong shock waves were driven by laser ablations in relatively rare gases as assumed in the blast wave theory, where the ambient gas pressures are lower and thus negligible compared to the pressures behind the shock waves.

By using the fitting parameter obtained from the data for background pressure at 200 Pa, we calculated the energy deposited into the blast wave. In the case of a laser ablation induced shock wave, the effective energy  $E$ , contained in the hemispherical blast wave is considered to be half of the energy predicted by Eq.(3), *i.e.*  $E = E_0/2$ . The estimated deposited energy was  $E = 16.5$  mJ, which is an order smaller than the incident Nd:YAG laser energy ( $\sim 150$  mJ). This result indicates that approximately 11% of the incident laser energy was converted to the kinetic and thermal energy of the blast wave. The rest of the laser energy is considered to be consumed by the vaporization and ionization of the target atoms, and some of the laser light may be reflected by the plasma as well as the surface of the aluminum target. Thus, it is reasonable that the estimated blast wave energy is much smaller than the incident laser energy.

#### 4 Summary

The time evolutions of shock waves induced by pulsed laser ablation at different surrounding gas pressures have been studied using a probe beam deflection technique. This technique allowed us to sensitively detect the transit time of shock front at a fixed point in space even in a tenuous gas. In the early stage of shock expansion, the shock speed was faster in lower background pressure. We observed that the shock wave rapidly attenuate with time and finally become a sound wave. The correlation between the transit time and the distance from the target surface was in good agreement with the ideal spherical blast wave model when the background gas pressure was relatively low. The theoretical model estimated that approximately one ninth of the incident laser energy converted to the blast wave energy, which indicates that most of the laser energy was used to vaporize, excite, and ionize the target atoms.

#### References

- [1] Y. Iwata, M. Kishida, M. Muto, S. Yu, T. Sawada, A. Fukuda, T. Takiya, A. Komura, and K. Nakajima. *Chemical Physics Letters* **358**, 1 (2002).
- [2] S. Vučković, M. Svanqvist, and V. Popok. *Review of Scientific Instruments* **79**, 7 (2008).
- [3] A. V. Bulgakov and N. M. Bulgakova. *Journal of Physics D: Applied Physics* **28**, 8 (1995).
- [4] G. Taylor. *Proceedings of the Royal Society of London. Series A, Mathematical and Physical Sciences* **201**, 1065 (1950).
- [5] S.-B. Wen, X. Mao, R. Greif, and R. E. Russo. *Journal of Applied Physics* **101**, 2 (2007).
- [6] S. Harilal, G. Miloshevsky, P. Diwakar, N. LaHaye, and A. Hassanein. *Physics of Plasmas* **19**, 8 (2012).
- [7] P. L. Ventzek, R. M. Gilgenbach, J. A. Sell, and D. M. Heffelfinger. *Journal of Applied Physics* **68**, 3 (1990).
- [8] G. Callies, P. Berger, and H. Hugel. *Journal of Physics D: Applied Physics* **28**, 4 (1995).
- [9] E. Amer, P. Gren, and M. Sjö Dahl. *Journal of physics D: Applied physics* **41**, 21 (2008).
- [10] S. Jeong, R. Greif, and R. Russo. *Journal of Physics D: Applied Physics* **32**, 19 (1999).
- [11] J. Diaci and J. Možina. *Ultrasonics* **34**, 2 (1996).
- [12] R. Pini, R. Salimbeni, M. Vannini, and G. Toci. *Applied Physics B* **61**, 5 (1995).
- [13] C. S. Aké, H. Sobral, M. V. Muniz, L. Escobar-Alarcón, and E. Camps. *Optics and Lasers in Engineering* **39**, 5 (2003).
- [14] H. Liepmann and A. Roshko. *Elements of Gasdynamics*. Dover Books on Aeronautical Engineering Series (Dover Publications, 1957).

# Giant Cluster Ion Inertial Fusion Driver and Its Possible R&D using the KEK 12 GeV PS Facility

Ken Takayama<sup>1\*</sup> and Kazuhiko Horioka<sup>2</sup>

<sup>1</sup>*High Energy Accelerator Research Organization, Accelerator Laboratory*

<sup>2</sup>*Tokyo Institute of Technology*

## ABSTRACT

Several heavy ion drivers for heavy ion inertial fusion have been proposed in US and Europe, based on linear induction accelerator technology [1] and existing RF technology [2], respectively, although they have not been realized on a large scale. Developing accelerator technology may provide an alternative compact, robust, and relatively cheap quantum beam driver for future particle beam inertial fusion. Here, we propose an accelerator complex for accelerating giant cluster ions, instead of lead or bismuth ions, toward 120 GeV by using induction acceleration over the entire energy region. The proposed two-way multiplex induction synchrotron that is the main accelerator for the giant cluster ion beam would be equivalent to 10 synchrotrons of the same size for a single beam.

Key Words: Cluster Ion, Inertial Fusion, Induction Acceleration, Microtron, Synchrotron

## 1. Introduction

The development of heavy ion fusion began 40 years ago [3]; however, it is still unclear when a prototype will be realized. This may be attributed to the following technical reasons. Proof of principle experiments are financially and technically difficult to conduct. Meeting the exceptionally strict requirements for absolute deposited beam power, density, and beam profile parameters in 3D space is both expensive and technically demanding. The beam driver largely depends on target design, and because target design has not been established, it is not possible to design a universal driver. Recent result for laser inertial fusion by the National Ignition Facility never seems to enhance further activities of the

particle beam fusion [4]. There has also been a big delay in the ITER project, the results of which will inform the decision whether to take the next step in fusion technology development. Budgets are insufficient for cases that are not intended for defense programs.

There are also political reasons for the delay in creating a prototype. Most developed countries officially support the ITER project as a priority. However, governments do not appear to be backing inertial fusion development with strong policies, although academics have consistently highlighted the importance and necessity of inertial fusion. Consequently, it is unlikely that top-down projects will be initiated.

The High Energy Physics Society and the major accelerator laboratories, which have developed accelerator technology and have extensive experience with huge accelerator complexes, are not interested in fusion itself, because they recognize that heavy ion inertial fusion is an engineering problem rather than a basic science problem. Lawrence Berkeley National Laboratory is exceptional among them. Accelerator scientists also tend to avoid risky accelerators because they are responsible for constructing the accelerator and making it operate as expected. Some physicists may dream to control dark matter or dark energy artificially in the future, although this is currently a science fiction. The energy generation industry is focused on keeping their businesses running, and they continue to use their current fission reactor technology. The electric power companies that supply end users are busy managing their existing fission reactors and their main concern is decommissioning old reactors in the near future. The market is going to shift its investment from fossil fuel or nuclear energy to renewable energy [5], and fusion energy is completely out of its scope.

We expect that there will be no major changes in our field during the coming decade, except for activities in China [6]. We may have plenty of time to explore further possibilities that arise from existing heavy ion beam fusion scenarios. In this short note, we provide an overview of one such research avenue that is based on recently developed accelerator technology.

The induction synchrotron has been developed over the last decade [7-9]. This technology can remove the limitations of the RF frequency bandwidth inherent in

all RF accelerators and greatly increase the freedom of beam handling through the functional separation of beam acceleration and confinement in the moving direction. In addition, a feasibility study for induction microtrons [10] has suggested that giant cluster ions, such as Si-100 or C-60, with a large mass to charge ratio can be accelerated from their extremely low energy. It has been predicted that the Pb ablator material has an extremely large stopping power when these cluster ions hit the target [11]. It may be time to focus on these cluster ions as driver ions for inertial fusion. The induction microtron can be used as an injector for the downstream main driver. Here, we propose a driver system that consists of a two-way multiplex induction synchrotron as the main accelerator, a permanent magnet stacking ring, and an induction microtron as an injector.

Prototypes are expensive and require extensive infrastructure. The KEK 12 GeV Proton Synchrotron and the Fermilab Tevatron have already been shut down. Other high energy accelerators around the world will finish their roles around 2030. SuperKEKB, Relativistic Heavy Ion Collider of Brookhaven National Laboratory, and Hadron-Electron Ring Accelerator of DESY may be among them. Their infrastructure, such as accelerator tunnels with perfect radiation shielding, cooling water systems, and power supply yards are valuable. In some cases, accelerator components, such as magnets or evacuation systems, may become available. Using these resources again for future fundamental energy science should be supported by tax payers, although there may be resistance from

existing stakeholders. In the intermediate stage of proof of principle experiments, the infrastructure could be very useful. We would like to propose the creation of an international consortium to develop a unified prototype model to involve accelerator experts in these institutes.

## 2. Choice of a projectile ion beam and beam parameters

The key features of a driver beam are the range of a projectile ion in the target ablator surface, the absolute beam power, and the 3D beam profile parameters. Once an ion species and target material have been determined, the range needed in the target material determines the kinetic energy required for the ion. The required absolute power determined by the target gain governs the total number of ion particles. The logic is simple. An ion beam with a large mass number and low charge-state is used because of the reduced space-charge effects. A previous study suggests that  $\text{Pb}^+$  has an energy of 8 GeV in the spherical target configuration [12] and 90 GeV in the X-target configuration [13]. The required 3D beam profile parameters depend strongly on the target configuration. We consider that giant cluster ions, such as Si-100 or C-60, with an energy of more than 100 GeV are suitable candidates as driver ions. These cluster ions have an extremely large mass number of 1000–3000. The advantages of using the giant cluster ions are as follows. They increase the stopping power in a target by an order of magnitude (cluster effects). They reduce space-charge effects, such as the Laslett tune shift  $\Delta\nu \sim N(Q/A)^2/\beta^2\gamma^3$ , where  $N$  is the number of ions,  $Q$  is the charge state

of the ion,  $\beta$  and  $\gamma$  are relativistic parameters, and the initial transverse emittance is assumed to be proportional to ion mass number  $A$ .  $A \gg 207$  and  $Q > 1$ , but still  $A/Q > 207$  (that of  $^{207}\text{Pb}^{1+}$ ). Giant cluster ions also exhibit efficient acceleration  $E = QeV$ , where  $E$  is the energy gain per turn and  $V$  is the acceleration voltage per turn. Furthermore, the cluster effects themselves are of fundamental scientific interest.

## 3. Driver

Currently, electrostatic accelerators are used as the accelerator driver for cluster ions, and have provided cluster ions for material science so far. The energy of this type driver is limited by its intrinsic nature. There is a gap between the low-energy region of electrostatic accelerators and the high-energy region of conventional RF accelerators. Cluster ions can be accelerated through the entire energy region by using induction accelerators, such as induction linacs, induction synchrotrons, and induction microtrons. Linacs are more expensive than circular accelerators. This was the motivation for proposing recirculating linacs based on induction acceleration in the US [14].

Here, we propose an accelerator complex to accelerate giant cluster ions toward 120 GeV. It has an induction microtron as an injector and its main accelerator is a two-way multiplex induction synchrotron. A permanent stacking ring is placed between the injector and main accelerator, where the giant cluster ions are stacked to increase the beam intensity. The two-way multiplex induction synchrotron is an advanced accelerator that makes maximum use of the guiding magnetic flux density

and induction accelerating fields. Fig. 1 shows a schematic of the accelerator complex, where a giant cluster ion beam of 1 MJ is produced in the main accelerator with an orbit circumference of 3 km.

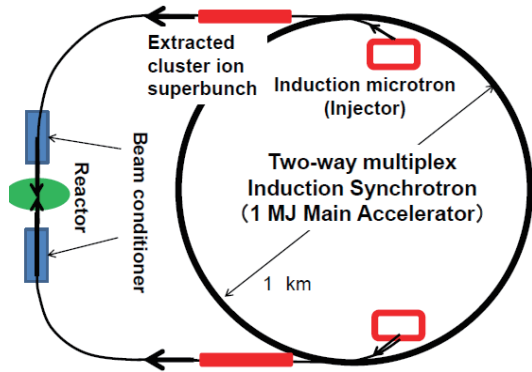


Figure 1 Schematic of the quantum beam driver for future inertial fusion

### 3.1 Giant cluster ion source

Recently, an efficient Si cluster production technique has been developed, where Si clusters are produced in a temporal and spatial confinement volume assisted by a shock wave in the background helium gas [15]. The production of covalent Si crystals with a good mass spectrum has been demonstrated. Several type of cluster ion sources, including a laser stripping source and an electrostatic nozzle source, are under development [16].

### 3.2 Racetrack-shape fixed field induction accelerator (Induction Microtron) as an injector

A racetrack-shape fixed field induction accelerator (RAFFIA) is an induction accelerator capable of repeatedly accelerating charged particles (Fig. 2). The RAFFIA has two straight sections, in which the beam orbit does not change from injection to extraction. The region can accommodate induction acceleration

cells, which are similar to toroidal compact cells for the induction synchrotron [9]. This setup does not require any technological advances. The geometrical shape of the RAFFIA is similar to that of a recirculating electron microtron, although the microwave linac in the recirculating electron microtron is replaced with a stack of induction acceleration cells in the RAFFIA. The energy gained during induction acceleration in the RAFFIA may be limited to 50 kV per turn in practical cases. In electron microtrons, it is a vital to maintain synchronization between the bunch revolution and accelerating microwaves because of the discrete jump in orbit length. In the RAFFIA, the synchronization is maintained by the intrinsic nature of the pulse voltage triggers at the arbitrary timing and monitoring of the circulating ion bunch. Changes in the path length with acceleration do not affect the synchronization, and so it is not necessary to dwell on this point.

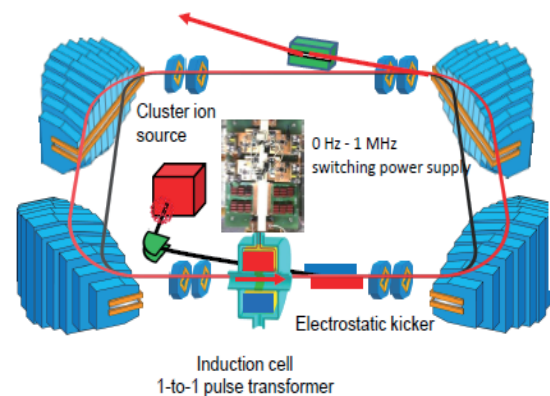


Figure 2 Schematic view of the RAFFIA

### 3.3 Permanent magnet stacking ring

Beam current delivered from the injector is limited by the space-charge effects of the low-energy beam. The beam stacking technique produces a higher

current beam. Thus, a multiplex permanent magnet stacking ring is inexpensive and efficient. A large permanent magnet storage ring has been demonstrated in Fermilab as an antiproton recycler ring [17]. The injected ion beam maintains its injection energy, and the bending magnet does not require a large flux density; a ferrite permanent magnet [18] is sufficient to guide the giant cluster ion. Twenty giant cluster ion bunches that are accelerated in the induction microtron are injected into the stacking ring every 50 ms. Twenty bunches are combined by the barrier bucket manipulation technique to form a single superbunch. The single superbunch is transferred to the corresponding beam line in the multiplex main ring every 1-2 s. The operational timetable for the induction microtron and stacking ring and the ramping cycle of the main ring bending magnet are shown in Fig. 3.

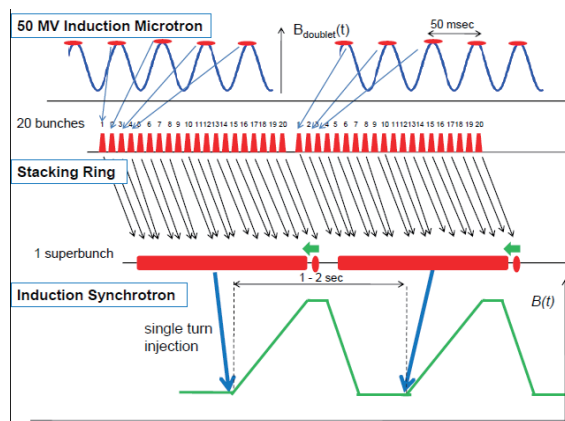


Figure 3 Beam transfer timetable

### 3.4 Two-way multiplex induction synchrotron

The magnet configuration in Fig. 4 partially mimics the CERN booster, where five beam lines are placed in the vertical direction. The return flux is characterized in the present multiplex ring, which can

accommodate the backward superbunches. This feature is similar to the proposed pipetron, which has been considered as a cheap proton-proton collider at Fermilab [19]. The two-way multiplex configuration is crucial for reducing the machine cost; 10 accelerator rings are accommodated in a single accelerator ring. Flux leakage should depend on an individual gap due to the asymmetric geometry of the multiplex magnet. The winding of an individual magnet pole should be fixed after careful full-scale field calculations and tests of the prototype magnet. The five forward and five backward superbunches share the induction cells for acceleration and confinement, in which the forward superbunches are accelerated with the set voltage and the backward superbunches with the reset voltage as shown in Fig. 5. The magnet lattice of the ring has four-fold symmetry and four long straight dispersion-free sections for injection/extraction and acceleration devices. At the last stage of acceleration, the phase-space profile of the superbunches in the longitudinal direction is manipulated by barrier bucket gymnastics to match the condition for drift compression or further beam handling beyond extraction [20].

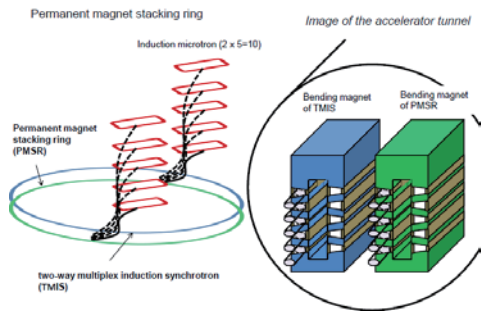


Figure 4 Schematic views of the beam transfer from the induction microtron to the stacking ring and the main ring tunnel

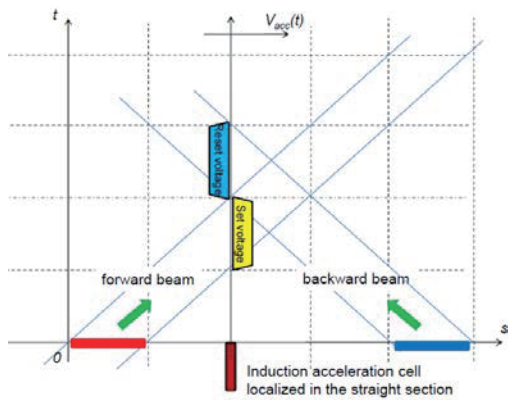


Figure 5 Schematic of two-way acceleration

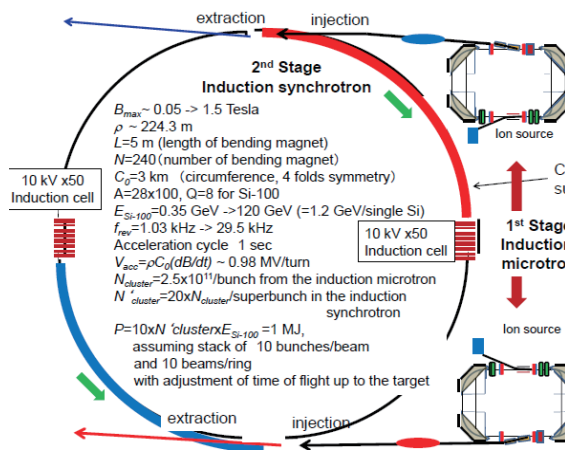


Figure 6: Example of the giant cluster ion beam driver of 1 MJ

An example of a 1 MJ driver is given in Fig. 6 with

numerical parameters.

#### 4. Possible R&D Scenario using the KEK 12 GeV PS Facility

It is not easy to perform necessary R&D works in order to confirm any scenario of inertial fusion driver in a meaningful scale. However several high accelerator facilities for high energy physics, which had carried out their duties, become available. The KEK 12 GeV PS with an orbit circumference of 340 m is among them. Its last stage was operated as an induction synchrotron to accelerate protons. All magnets exist as they have been. It can work for giant cluster ions if the sufficient enough evacuation system to realize the vacuum level of  $10^{-7}$  Pa is employed. The upstream KEK digital accelerator mentioned earlier [9] is ready to run for giant cluster ions with crucial improvements of the evacuation system and some renovation of the induction acceleration system such as a varying DC voltage source. Meanwhile, the 12 GeV PS main ring tunnel can accommodate a permanent storage ring as illustrated in Fig. 7a and 7b, which giant cluster ions transferred from the KEK-DA are injected into, accumulated in, and delivered to the main ring from.

This accelerator facility shall enable us to learn a whole story how to obtain high energy giant cluster ions that have never been realized in the world.

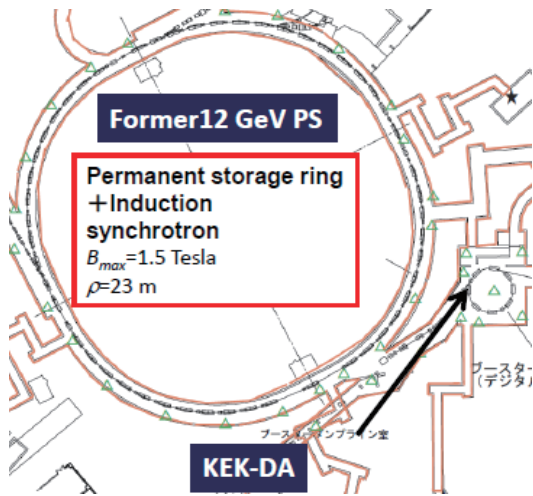


Figure 7a: Former KEK 12 GeV PS

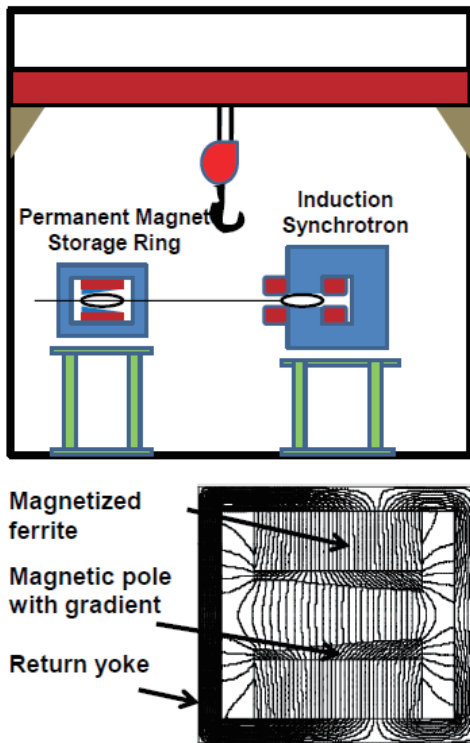


Figure 7b: Schematic view of the 12 GeV PS tunnel and the cross-section of the prototype permanent magnet [18]

#### 4. Remaining problems

There are still crucial problems that must be overcome to realize our proposed system. The beam loss of giant cluster ions is caused by in-beam charge

exchange, and by electron capture and stripping caused by interactions with residual atoms and molecules. Electron capture and stripping depend on the vacuum and the velocity of the ion, respectively. The loss originating from electron capture and stripping can be reduced by improving the vacuum, although the cross section data are not available. Meanwhile, existing studies on ion-ion charge exchange cross sections for single heavy ions [21, 22] may not be extrapolated simply to the present case. The size of the actual cluster effects of a relativistic giant cluster ion in the target material are difficult to estimate quantitatively because there are no experimental data. The integration of the beam manipulating procedure for beam extraction and the target, including the drift compression, must also be addressed.

#### 5. Summary

We have proposed a giant cluster ion driver for future inertial fusion. The driver size has not been optimized here because we assumed that the existing accelerator tunnel would be used. Induction acceleration over the entire energy region is used and the projectile ions are giant cluster ions instead of heavy ions. The advantages of our proposed system can be summarized as follows: it mitigates space-charge effects; it has higher acceleration efficiency than that of the lowest charge state ion; the stopping power in the target material is large; and it uses two-way multiplex acceleration. Although many crucial issues remain unsolved, we believe our proposed system is worthy of further development. It is emphasized that the existing accelerator facility

becomes a quite good infrastructure to carry out extensive R&D works aiming to realize an original inertial fusion scenario.

## References

- [1] R.O.Bangerter, "The Induction Approach to Heavy-Ion Inertial Fusion: Accelerator and Target Considerations", *IL NUOVO CIMENTO* **106 A**, 1445 (1993).
- [2] I.Hofmann, "Heavy ion inertial fusion in Europe", *Nucl.Instrum. Methods A* **464**, 24 (2001)..
- [3] ERDA Summer Study of Heavy Ions for Inertial Fusion, Oakland/Berkeley, California, Jul 19-30, 1976: Final Report Dec 1976 - 110 pages, LBL-5543
- [4] "2015 Review of the Inertial Confinement Fusion and High Energy Density Science Portfolio", DOE/NA-0040 (2016).
- [5] L. Brown and E. Adams, *The Great Transition: Shifting from Fossil Fuels to Solar and Wind Energy* ( W.W.Norton & Company, New York London, 2015).
- [6] G. Xiao, R. Cheng, Y. Wang, X. Zhou, Y. Lei, Y. Sun, G. Xu, J. Ren, X. Ma, and Y. Zhao, "High Energy Density Research at the future project HIAF in China", *the 21 st International Symposium on heavy Ion Inertial Fusion*, in Astana Kazakhstan, July 18-22, 2016
- [7] K.Takayama *et al.*, "Experimental Demonstration of the Induction Synchrotron", *Phys. Rev. Lett.* **98**, 054801 (2007).
- [8] *Induction Accelerators* (Springer-Verlag, Berlin Heidelberg, 2011) edited by K. Takayama and R.J. Briggs, Chapter 11.
- [9] K.Takayama *et al.*, "Induction Acceleration of Heavy Ions in the KEK Digital Accelerator: Demonstration of a Fast Cycling Induction Synchrotron", *Phys. Rev. ST-AB* **17**, 010101 (2014).
- [10] K.Takayama, T.Adachi, M.Wake, and K.Okamura, "A Racetrack-shape Fixed Field Induction Accelerator for Giant Cluster Ions", *Phys. Rev. ST-AB* **18**, 050101 (2015).
- [11] Y. Iwata (AIST), *Symposium on the Induction Microtron for Quasi-relativistic Giant Cluster Ions at KEK*, March 29-30, 2016.
- [12] P.A.Seidl, J.J. Barnard, A Faltens, and A. Friedman, "Research and development toward heavy ion driven inertial fusion energy", *Phys. Rev. ST-AB* **16**, 024701 (2013).
- [13] E. Honestroza and B.G. Logan, "Progress towards a high-gain and robust target design for heavy ion fusion", *Phys. of Plasmas* **10**, 072706 (2012).
- [14] J.J.Barnard *et al.*, "Study of Recirculating Induction Accelerators as Drivers for Heavy Ion Fusion", UCRL-LR-108095 (1991).
- [15] Y. Iwata, K. Tomita, T. Uchida, and H. Matsuhata, "Crystallographic Coalescence of Crystalline Silicon Clusters into Superlattice Structures", *Crystal Growth & Design* **15**, 2119 (2015).
- [16] J.Hasegawa (TIT), *Symposium on the Induction Microtron for Quasi-relativistic Giant Cluster Ions at KEK*, March 29-30, 2016.
- [17] G. Jackson *et al.*, "Fermilab Recycler Ring", FERMILAB-TM-1981 (1996).

- [18] E. Nakamura, K. Egawa, S. Igarashi, K. Takayama, and K. Ogata, “Permanent Magnets for the 500 MeV Accumulator Ring of the Intensity Doubler Project in KEK-PS”, *Proceedings of 7<sup>th</sup> EPAC*, Vienna, June 2000, Vol. 1, p382 (2000).
- [19] G.W. Foster and E. Malalud, “Low-Cost Hadron Colliders at Fermilab: A Discussion Paper”, FERMILAB-TM-1976 (1996).
- [20] T. Yoshimoto, Thesis (TokyoTech, 2016), submitted to *Phys. Rev. ST-AB*.
- [21] R. Trassl, H. Brauning, K.V. Diemar, F. Melchert, E. Salzborn, and I. Hofmann, “Ion-ion exchange cross-sections for heavy ion fusion”, *Nucl. Instrum. Meth. A* **464**, 80 (2001).
- [22] J.J. Barnard *et al.*, “Recirculating induction accelerators as drivers for heavy ion fusion”, *Phys. Fluids B* **5**, 2698 (1993).

# Study on Cost Evaluation and Social Cost in Heavy-Ion Inertial Fusion System

Akie Inoue, Kazumasa Takahashi, Toru Sasaki, Takashi Kikuchi, Nob. Harada,  
John J. Barnard

*Nagaoka University of Technology*

*\*Lawrence Livermore National Laboratory*

## ABSTRACT

System and social costs were considered for a power plant system of inertial confinement fusion driven by heavy-ion beams. The cost for the power plant system consists of the initial cost and the other cost. For the initial cost, a relation between each components of accelerator complex was considered with a network visualization. The other cost was considered as market failure and social cost. In the market failure, market externality was studied for the nuclear fusion power plant system. The strong connection between peripheral people and the nuclear power plant side should be established via technical communications.

## Keywords

Heavy-ion Inertial Fusion, Social Cost, Nuclear Fusion Power Plant, System Analysis

## 1 Introduction

An inertial confinement fusion scheme driven by intense heavy-ion-beam irradiation is called as heavy-ion inertial fusion (HIF) [1]. In the HIF system, the heavy-ion accelerator complex is key issue, and physics of space-charge-dominated beams is one of main research topics. Also, the generation and the control of the high-current heavy-ion beam are a special technical topic in the HIF system. In the nuclear fusion power plant, not only the technical and the physical issues but also the cost is critical from the viewpoint of the social acceptability.

In this study, the system and the social cost are considered for the HIF power plant. The cost of the HIF power plant system consists of the initial cost and the other cost. For the initial cost, the linkages between the components are considered with the network visualization. The other costs are considered from the viewpoint of the market failure and the social cost.

## 2 System Analysis and Component Linkage

The HIF system has many components such as ion source, accelerator complex, beam transport line, final focus system, reaction chamber, electrical power generator, and so on [2]. The total cost and the cost at each component were estimated for the HIF system as the initial cost [2].

However, the relation between the cost and the component linkage is unclear. If a low cost component has the strong linkage with a high cost component, the specification change of the low cost component may affect the specification change of the high cost component. In the case, not only the high cost component but also the low cost component has possibility to impact on the total cost of the HIF power plant system.

For this reason, the relation between the component linkage and the component cost was investigated by using the network visualization [3]. The result indicated that the component “Final Transport” is low cost, and has strong linkage with

the high cost component “Total Accelerating System” [3]. As a result, it was found that the component “Final Transport” may affect on the total cost of the HIF system.

### 3 Social Cost and Market Failure

As the social cost, the market failure consists of market externality, public goods, economies of scale, and information asymmetry. In this study, we focus on the market externality for the HIF power plant system.

In the case of the HIF system, the market externality is considered as follows.

- site area size
- radio activation
- biogeocenosis effect
- peripheral people support

The site area for the hydroelectric power plant is 3.49 km<sup>2</sup> (water surface area) for Kurobe Dam (335 MW) [4]. The site area for the nuclear power plant is 4.2 km<sup>2</sup> for Kashiwazaki Kariwa Nuclear Power Station (total capacity of 8,212 MW) [5]. On the other hand, the accelerator size of the HIF system (design output of 1 GW) was estimated as 600 m for the diameter of the recirculator [2]. In the case of the HIF system, the facility size is dominated by the accelerator. In the comparison with the conventional power plants, the site area for the HIF power plant is not considered as a main problem.

In the case of the nuclear fission power plant, the treatment for the used fuel is most important problem because the used fuel for the nuclear fission power plant is radioactive. On the other hand, the nuclear fusion products are not radioactive. For this reason, it is not serious problem. However, the first wall of the reaction chamber is radioactivated because is irradiated by the fast neutron with high flux produced by the DT fusion reaction. Consequently, the radioactivated materials for the chamber wall should be properly treated inside the site of the nuclear fusion power plant.

In the case of the nuclear fission power plant, the cooling water is one of the problems because

the warm water discharge induces the ecosystemic abnormality in the aqueous environment. It is also expected that the nuclear fusion power plant has same problem.

The peripheral people support is considered as most important issue for the social cost. The “nuclear”, “radioisotope”, “radioactivity”, and so on, are uneasy keywords for the peripheral people around the plant. The consanguinity between the peripheral people and the nuclear power plant side should be established via technical communications, well.

### 4 Conclusion

The system and the social costs were considered for the HIF power plant system. The cost for the power plant system consists of the initial cost and the other cost. For the initial cost, the relation between the components of the HIF accelerator complex was considered with the network visualization. The other cost was considered as the market failure and the social cost. In the market failure, the market externality was studied for the nuclear fusion power plant system. The tight connection between the peripheral people and the nuclear power plant side should be established via technical communications.

### References

- [1] S. ATZENI and J. MEYER-TER-VEHN, *The Physics of Inertial Fusion: Beam Plasma Interaction, Hydrodynamics, Hot Dense Matter* (Oxford Univ., N.Y., 2004).
- [2] J.J. BARNARD et al., *Phys. Fluids* **B5**, 2698 (1993).
- [3] A. INOUE et al., *Journal of Physics: Conference Series* **717**, 012097 (2016).
- [4] Kurobe Dam Official Site, <http://www.kurobedam.com/>
- [5] TEPCO: Power Supply Facilities, <http://www.tepco.co.jp/en/challenge/energy/nuclear/plants-e.html>

# Characterization of High-Energy Ions in the Divergent Gas-Puff Z-Pinch

Takashi Shikone, Shun Hakamatsuka, Keiichi Takasugi\*

*College of Science and Technology, Nihon University*

*\*Institute of Quantum Science, Nihon University*

## ABSTRACT

Characterization of high energy ions was conducted to understand the acceleration mechanism of ions in the divergent gas-puff z-pinch. It was reconfirmed that there was also ion acceleration in the negative discharge. Comparison of ion acceleration in Ar and Kr discharges was carried out, and the maximum acceleration energy was almost the same.

## Keywords

Divergent Gas-Puff Z-Pinch, High-Energy Ion, Ion Acceleration, Thomson Parabola Analyzer

## 1. Introduction

Divergent gas-puff z-pinch has been devised for the realization of efficient soft x-ray point source. In the divergent gas-puff z-pinch experiments, hard x-ray which has never been observed in the conventional gas-puff z-pinch was observed, and the generation of high-energy electrons was revealed [1]. In addition, the generation of high-energy ions was revealed from the ion measurement. By changing the direction of the discharge current, high-energy ions were observed as well. The presence of ion acceleration which does not depend on the direction of current was revealed [2].

Divergent gas-puff z-pinch is similar to the plasma focus in that it is non-uniform pinch in the axial direction. Generation of high-energy ions has also been observed in the plasma focus. The acceleration mechanism has been understood to be due to electromagnetic induction [3]. Ion acceleration which does not depend on the direction of the current could not be explained by electromagnetic induction, and the statistical acceleration model by the shrinking magnetic wall was proposed [4].

In order to investigate the origin of ion acceleration, the pinhole measurement of ions were made. Ion distribution in the double coaxial structure was observed, and the structure was found to be dependent on the direction of the current. In addition, it was also clear that the high-energy ions were generated from the spot-like ion source [5].

In this research the past measurements of high-energy ions was reexamined, and the dependences of discharge current and ion species on the ion acceleration were investigated.

## 2. Experimental Setup

Figure 1 shows a schematic diagram of the SHOTGUN III z-pinch device used in the experiment. The device consists of 12  $\mu\text{F}$  capacitor bank. It uses a  $\pm 40$  kV power supply, and it is possible to perform both positive and negative discharges. An annular divergent gas nozzle is mounted on the inner electrode. The ejection angle is 10 degrees outward. The diameter of the nozzle and the distance between the electrodes are both 30 mm. Ar or Kr gas is used in the experiment. The plenum pressure is set to 5 atm. The material of the inner electrode is stainless steel, and that of the outer electrode is aluminum.

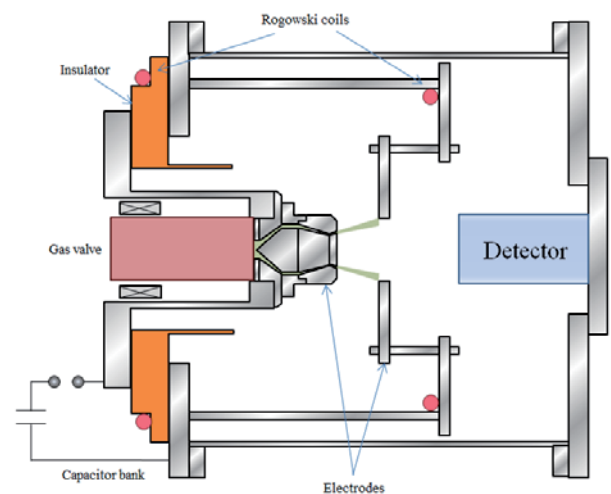


Fig. 1 Schematic diagram of the SHOTGUN III z-pinch device

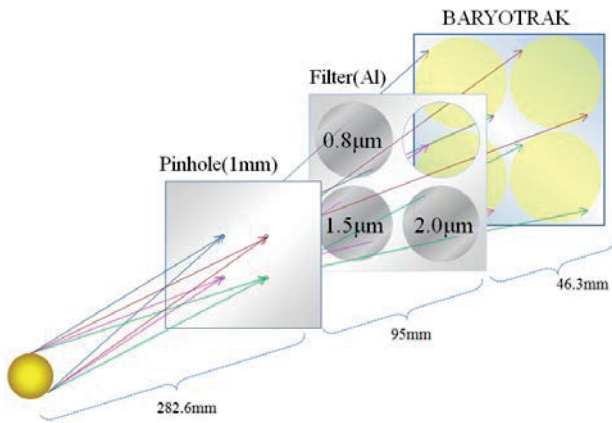


Fig. 2 Schematic drawing of the filtered 4-hole ion pinhole camera

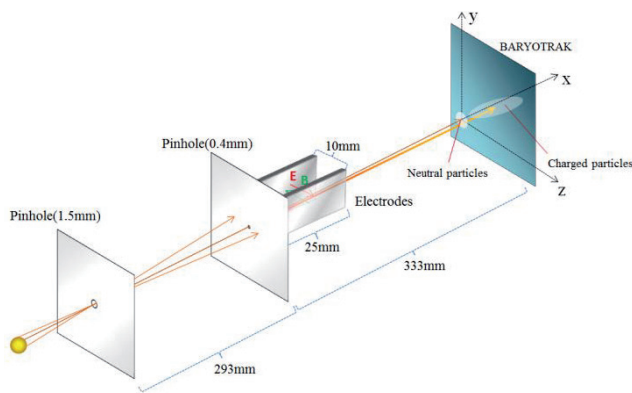


Fig. 3 Schematic drawing of the Thomson-parabola analyzer

Figure 2 shows the 4-hole ion pinhole camera with filters to evaluate approximate energy and the spatial distribution of the accelerated ions. The filters are made of Al, and the energy of the transmitted ions is calculated from maximum range of Ar ion in Al. Three kinds of Al filters ( $0.8\ \mu\text{m}$ ,  $1.5\ \mu\text{m}$ , and  $2.0\ \mu\text{m}$ ) are used in the measurement. The corresponding energies are 0.7 MeV, 1.7 MeV and 2.5 MeV, respectively.

Figure 3 shows a schematic drawing of the Thomson parabola analyzer. Electrodes and the magnetic poles are arranged in parallel behind two pinholes. Each ion is changed in the direction perpendicular to each other by the electric and magnetic fields. By the magnitude of the deflection the energy and ion species can be measured precisely.

BARYOTRAK ( $67 \times 67 \times 0.9\ \text{mm}$ ) is used for the detection of accelerated ions. This is an improvement over the general ADC (allyl diglycol carbonate) plastic plate which is known as CR-39. It is a solid track detector used for detection and dosimetry of neutron, proton, alpha particle and cosmic rays, whose energy exceeding 100 keV.

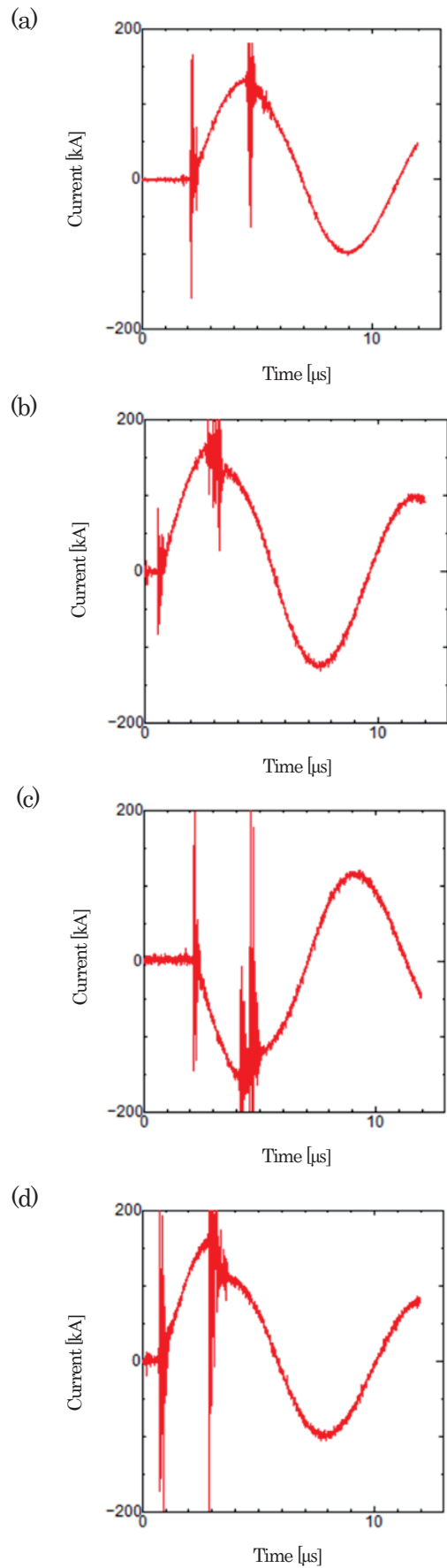


Fig. 4 Current waveforms of typical discharge in (a) Ar +20 kV, (b) Ar +25 kV, (c) Ar -25 kV and (d) Kr +25 kV.

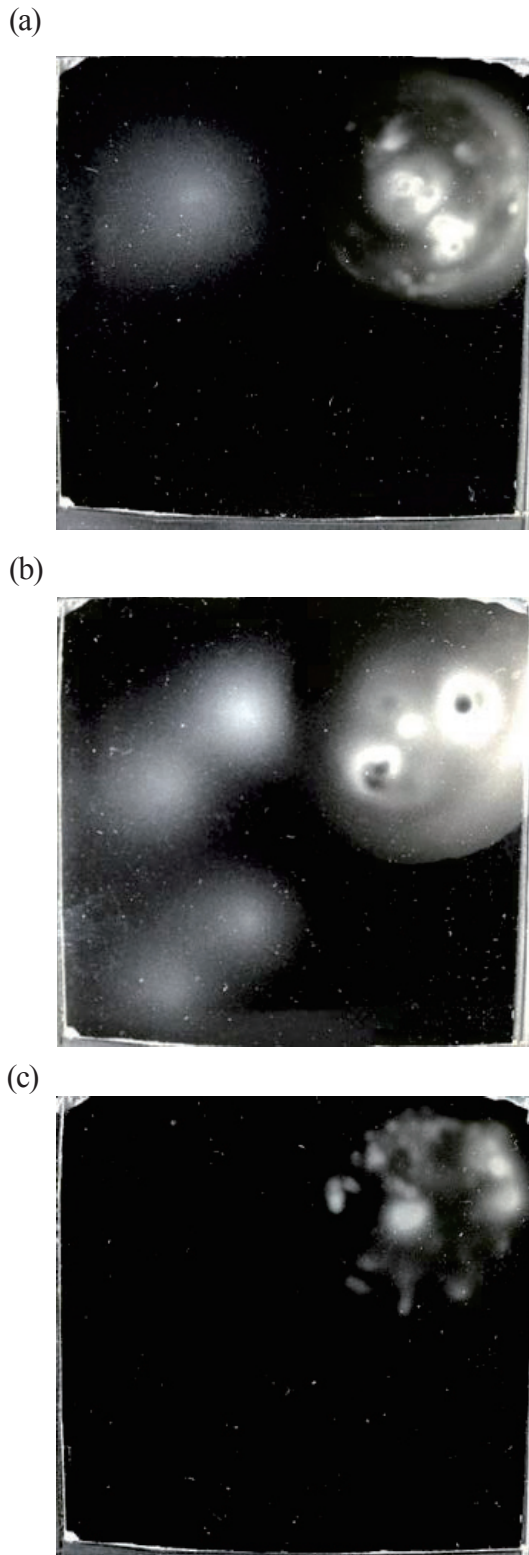


Fig. 5 4-hole ion pinhole measurements of Ar discharge at (a) +20 kV, (b) +25 kV and (c) -25 kV.

### 3. Discharge Characteristics

Figure 4 shows typical current waveforms of (a) +20 kV Ar discharge, (b) +25 kV Ar discharge, (c) -25 kV Ar discharge and (d) +25 kV Kr discharge. Pinch occurred near the peak of each sine wave. The current dropped rapidly at the pinch due to the

increment of plasma inductance. The currents were (a) 131.5 kA, (b) 161.8 kA, (c) -159.9 kA and (d) 158.3 kA. By comparing (a) and (b), the current was roughly proportional to the charging voltage. The decrement of current at the pinch was also large at high charging voltage. By changing the discharge polarity no big difference was observed. By comparing Ar and Kr discharges the decrement at the pinch was large at Kr discharge. The reason is that the temperature of the plasma by the adiabatic compression in the course of the plasma contraction increases, the temperature rise is suppressed due to the large radiation loss in Kr compared to Ar, resulting in reaching a smaller radius. Therefore, the induced electromotive force due to radial contraction is considered to be large in Kr.

### 4. Ion Pinhole Measurements

Ar discharge was performed by changing the charging voltage, and ion pinhole measurements were made. Figure 5 shows the results of (a) +20 kV, (b) +25 kV and (c) -25-kV. Each data shows no filter (upper right), 0.8  $\mu\text{m}$  Al (upper left), 1.5  $\mu\text{m}$  Al (lower left) and 2.0  $\mu\text{m}$  Al (lower right) filters as shown in Fig. 2.

At +20 kV ion tracks were observed at no filter and 0.8  $\mu\text{m}$  filter. At +25 kV ion source was separated in two parts. Ion tracks were observed at no filter, 0.8  $\mu\text{m}$  and 1.5  $\mu\text{m}$  filters. In the positive discharge, an increase in the energy of the ions was confirmed with increasing charge voltage. However, in the negative discharge at -25 kV ion tracks were observed only at no filter, and no ion passing through the filters was observed. Distribution of ion track appears to be spread throughout the field of view as well as the center.

### 4. Thomson Parabola Measurements

Measurements using the Thomson parabola analyzer were made by changing the discharge gas. The charging voltage was fixed to +25 kV. Figure 6 (a) shows the Thomson parabola measurement in Ar discharge. Horizontal and vertical axes represent deflections by electric and magnetic fields, respectively. Singly to triply ionized Ar ions were observed. The ions of maximum velocity are aligned in a straight line, which shows a constant velocity. Figure 6 (b) shows the Thomson parabola measurement in Kr discharge. Singly to triply ionized Kr ions were observed. The ions of maximum velocity are also aligned in a straight line, which shows a constant velocity.

The results of the analysis are summarized in Table 1. The results show that the maximum energy rather than the maximum velocity were equal in Ar and Kr discharges. From this result we cannot

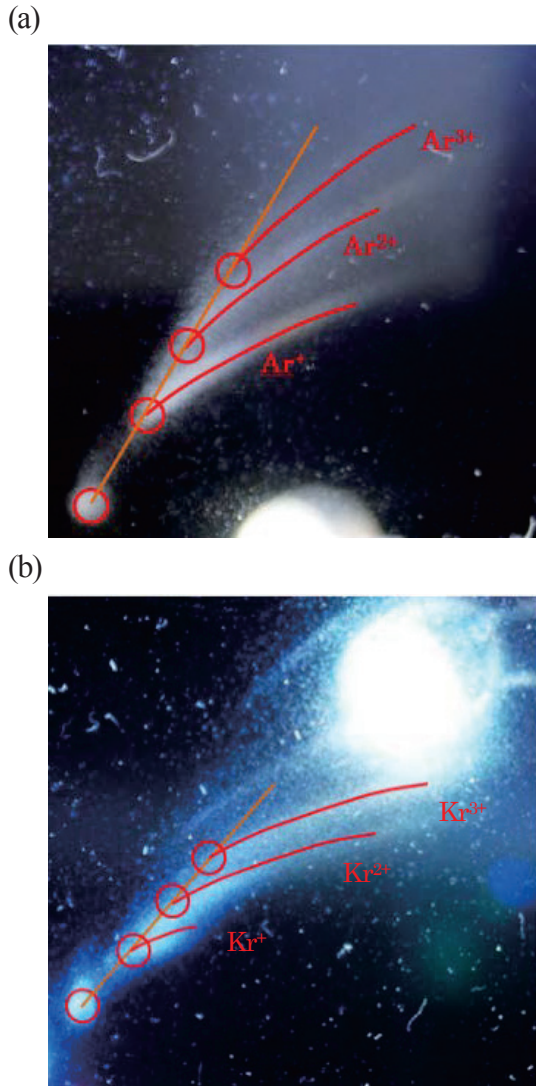


Fig. 6 Thomson parabola measurement of (a) Ar discharge and (b) Kr discharge.

Table 1 Summary of most accelerated ions in (a) Ar and (b) Kr discharges.

	Ar <sup>+</sup>	Ar <sup>2+</sup>	Ar <sup>3+</sup>
v [m/s]	2.3	2.3	2.3
E [MeV]	1.1	1.1	1.1

	Kr <sup>+</sup>	Kr <sup>2+</sup>	Kr <sup>3+</sup>
v [m/s]	1.6	1.6	1.6
E [MeV]	1.1	1.1	1.1

conclude anything simply for ion acceleration. Because it remains a possibility of difference such as in the current waveform or the shrinking velocity of the magnetic wall, although the experimental condition was fixed for two types of gas discharges. It is necessary

to make experiment in the same discharge such as to do it with mixed gas.

## 5. Summary and Discussion

First it is with respect to the pinhole measurement with Al filter, the increase of acceleration energy was confirmed with increase of charging voltage, even accelerated ions in the negative discharge was confirmed. The presence of accelerated ions in the negative discharge means the presence of the acceleration mechanism that does not depend on the current direction. However, the acceleration energy in the negative discharge was smaller than the positive discharge, it is conceivable that the acceleration effect of the induced electromagnetic force was applied.

In the Thomson parabola measurement, constant velocity of ions in the different charged states were observed in the same experiment. This is a result that supports the statistical acceleration model due to the shrinking magnetic wall. In the comparison of Ar and Kr discharges, the resulting acceleration energy was almost the same, although the induction voltage estimated from the change in the current is larger in Kr discharge. It is necessary to confirm the reproducibility by fixing the experimental conditions. It is also important to do the experiment with a mixed gas.

Although it was not shown in the experimental results that the reproducibility of pinch was changed by changing the nozzle width of the gas puff. In other words, the shape of the gas is no longer sharp by expanding the nozzle width, the plasma becomes unstable, and the pinch often occurs off the axis. As a result, no significant change was observed in the energy of the ions, but significant errors can be caused in the Thomson parabola measurement. It is necessary to carry out the experiment to examine well for the nozzle width.

## References

- [1] K. Takasugi and E. Kiuchi, Plasma Fusion Res. **2**, 036 (2007).
- [2] M. Nishio, H. Sakuma and K. Takasugi, Plasma Fusion Res. **6**, 1201009 (2011).
- [3] A. Moser, M. Sadowski, H. Herold, and H. Schmidt, J. Appl. Phys. **53**, 2959 (1982).
- [4] M. Nishio and K. Takasugi, "Characteristics of The Magnetic Wall Reflection Model on Ion Acceleration in Gas-Puff Z Pinch", NIFS-PROC-93, 28 (2013).
- [5] K. Takasugi, M. Iwata and M. Nishio, "Generation of High Energy Ions in the Divergent Gas-Puff Z Pinch", NIFS-PROC-94, 91 (2013)

# Numerical Analysis of Electron Behavior in Beam Diode Driven by Intense Pulsed Power Device

Md. Shahed-Uz-Zaman, Kazumasa Takahashi, Toru Sasaki, Takashi Kikuchi, Nob. Harada

*Nagaoka University of Technology, Nagaoka, 940-2188, Japan*

## ABSTRACT

Electron beam behavior in beam diode gap was investigated numerically using electrostatic particle-in-cell model based on the normalized value and experimental results of intense pulsed power discharge device ETIGO-II. Numerical results of the space charge limited electron emission expose the electron beam behavior in diode gap alone with the electrostatic field. Compilation of numerical result shows that due to the space charge limited current, virtual cathode is formed near the cathode surface, which is liable for the low output beam current. Numerically it is also observed that the beam current is significantly change with the change of diode gap distance and the change of emission radius at the cathode surface. Comparison of experimental results with the numerical results revealed the approximate electron emission radius at the cathode surface. Numerical results also qualitatively satisfy the experimental results of pulsed power discharge device ETIGO-II.

## Keywords

Electron beam behavior, Space-Charge limited emission, Pulsed-power generator

## 1. Introduction

The next-generation energy source to solve the energy problem is nuclear fusion by inertial confinement scheme. In inertial confinement fusion (ICF), materials of a fuel pellet pass through a warm dense matter (WDM) regime during the implosion process [1, 2]. Properties in the temperature-density region known as WDM are so important and have a great impact in implosion dynamics [3, 4]. For this reason, a generation method of WDM using an intense pulsed power generator with an electron beam diode was proposed to research the WDM property at comparable pulse duration to the ICF implosion [5, 6, 7]. Conversely the intense pulsed power generator can produce high electron beam current which is necessary for high power devices within the desired short time for high energy research applications [8, 9, 10, 11]. Clarified physical properties and behavior of electron beam is needed to utilize this technology properly and understand the WDM research data significantly.

The electron beam diode behaves as impedance, which regulates the input power and energy into the sample load. Though, the input power control with the electron beam diode was investigated experimentally, however the beam electrons behavior in the diode gap are not understood [6, 7]. Therefore, the clear understanding of the electron beam characteristics in electron beam diode gap with relativistic effect, a numerical analysis is done based on an electrostatic particle-in-cell (PIC) method, corresponding to the experimental results and experimental conditions of intense pulsed power device ETIGO-II.

## 2. Numerical model

The beam dynamics of an electron in gap are relatively complex, for the case of a gap with uniform electric field. Eventually the beam dynamics become more complicated, if the gap has a changing electric and magnetic field. Figure 1 show the typical numerical model of electron beam diode and it is

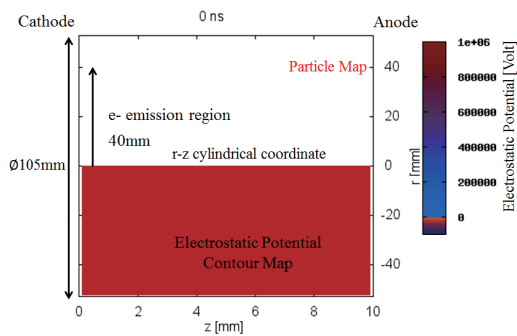


Fig. 1. Schematic diagram of numerical results: electron beam is emitted from the cathode surface and travel through the vacuum and reach to anode. Cathode radius is 55 mm. Gap distance  $d = 10$  mm. Beam radius  $r_{\text{emit}} = 40$  mm.

considered that the phenomena involved in cylindrically axisymmetric. The numerical simulation is done based on the 2 dimensional electrostatic PIC model. In this numerical study electron beam emission feature is based on space charge limited emission. So, satisfying the space charge limited conditions, the numerical simulation is done with the deliberation of time dependent relativistic particle motion. The electric field components are  $E_r$ ,  $E_z$  and velocities  $v_r$ ,  $v_z$  and position  $(r, z)$ . Those are solved using the Poisson equation, which is solved by successive over relaxation (SOR) method and weighting for the calculation of electron charge

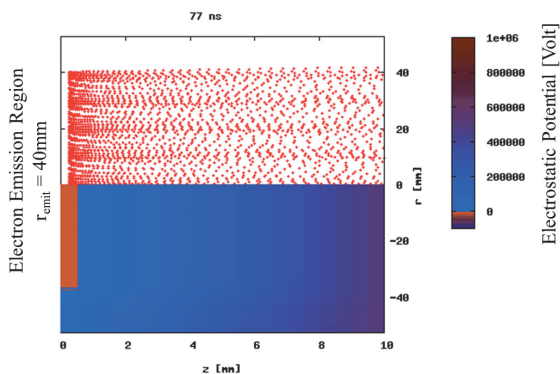


Fig. 2. Particle map with the electrostatic potential contour map at  $t = 77$  ns for electron emission radius of 40 mm. Dots show the electrons, and contour shows the electrostatic potential, respectively.

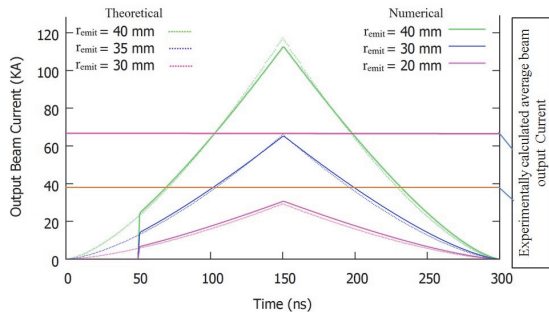
density is done by the cloud-in-cell (CIC) method, and relativistic equation of motion (Leaf-frog method is used for the calculation of velocity and position) [12, 13, 14]. In the calculation condition, the external applied voltage is 1 MV at maximum, and is the experimental value in the intense pulsed power device ETIGO-II [15]. The pulse width is 300 ns, and the rise and fall times are 150 ns, respectively. The peak voltage is 1 MV at 150 ns, and the output beam current is 50 ns lack by the applied voltage [7, 15]. Initially, the self-magnetic force is zero due to the zero electron beam velocity ( $v_z = 0$ ), and the self-magnetic force with the increase of velocity is not increased considerably. The electron motions are dominated by the Lorentz force ( $\mathbf{F} = q\mathbf{E} + q\mathbf{v} \times \mathbf{B}$ ), and are determined by the ratio of the force induced by the electric field ( $\mathbf{F}_E = q\mathbf{E}$ ) to the force induced due to the magnetic field ( $\mathbf{F}_M = q\mathbf{v} \times \mathbf{B}$ ). From the preparatory consideration for  $F_E / F_M$ , it is expected that the force induce by the magnetic field is smaller enough than the force induced by the electric field in this study. For this reason, the self-magnetic force is assumed as negligible.

The initial beam radius is 40 mm, which is framed as well as 30 mm and 20 mm according to numerical condition. The electrons are emitted from the cathode surface and travel through vacuum due to electrostatic potential. The diode gap is 10 mm and is set as 15 mm and 20 mm according to experimental condition. Computational area is  $0 \leq z \leq d$  and  $0 \leq r \leq 55$  mm, where centerline is the cylindrical axis.

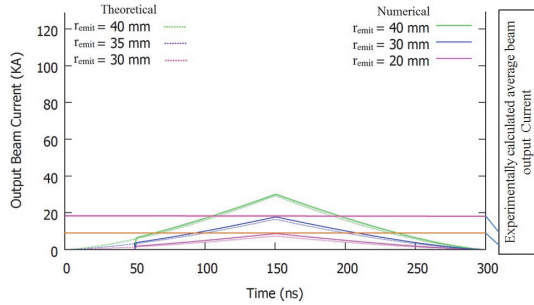
In the intense pulsed power generator "ETIGO-II", the maximum beam output current is calculated theoretically. The classified theoretical equation of space-charge-limited current is commonly known as "Child-Langmuir Law" [16].

### 3. Results and Discussions

Figure 2 shows the numerical results of particle map with the electrostatic potential at 77 ns. Here upper part shows the electron map, and lower part shows the contour map of the combined external and internal potential. Figure 4 shows the particle map for the beam electrons and the beam envelope line,



(a) Diode gap distance  $d = 10$  mm

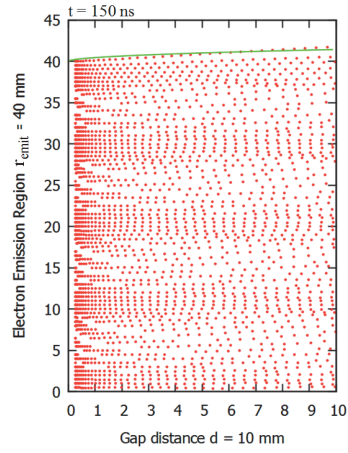


(b) Diode gap distance  $d = 20$  mm

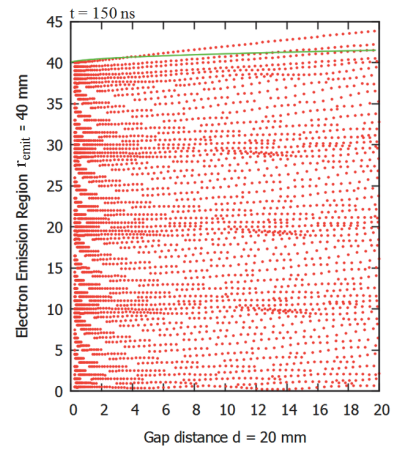
Fig. 3. Comparison in theoretical and numerical results for electron beam current; (a) diode gap  $d = 10$  mm and beam output current measured at  $z = 9$  mm (b) diode gap  $d = 20$  mm and  $z = 19$  mm. Here for the case of (a) and (b) only electron emission radius is changed to 40 mm, 30 mm and 20 mm.

which is obtained from the envelop equation [17, 18]. As shown in Fig.4, the beam radius expands gradually by the space charge effect.

In the parallel-plate vacuum diode gap once free electron enter, they produce the local electric field potential [18]. The emitted free electrons affected by both the external and the internal mutual electric forces. Negatively the electrons are emitted from the cathode surface, and move to the right (anode) side, and create a steady electric current density to the left (cathode) side [18]. The steady conventional electric current flow forms from the anode to the cathode. According to the numerical calculation result for the particle map, it is indicated in Fig. 2 that the virtual cathode is created near the cathode. Because of the space-charge limited condition, the virtual cathode is created. At the point of virtual cathode, the beam electrons come to a stop, and start to move backward



(a) Diode gap distance  $d = 10$  mm



(b) Diode gap distance  $d = 20$  mm

Fig. 4. Charged particle map of beam electrons: (a) at  $t = 150$  ns for diode gap  $d = 10$  m (b) at  $t = 150$  ns for diode gap  $d = 20$  mm. The beam envelope line is drawn using envelope equation and the beam radius is expanded gradually by the self-space charge effect

(left), which limits the output beam current.

Figure 3, comparison of the numerical and theoretical results, shows that the emission area is around 30 mm. Experimental result shows that the average output beam current is 50 ~ 60 kA [7], which qualitatively satisfies the above numerical results and confirm the electron emission radius in the experimental case. Though the real cathode is really big and diameter is 105 mm but electron is not emitting from the entire cathode surface. Eventually the electron emission region is really small in real

condition and from the experiment emission radius is also not clear. From Fig. 3, it is seen that especially for the  $r_{\text{emit}} = 30$  mm, the output beam current is limited by the space charge limited current and it qualitatively satisfies the experimental results. However, in the cases of  $r_{\text{emit}} = 40$  mm and  $r_{\text{emit}} = 20$  mm, the discrepancy between the numerical and theoretical results becomes large, because it is due to the localized emission area of electrons at the cathode in case of numerical simulation. As a result, the beam current does not increase along with the space charge limited current; even in the cathode area is large enough. From the overall evaluation of theoretical and numerical results, electron emission radius of cathode surface is estimated around 30 mm in the case of experiment with the standardized condition of intense pulsed power generator ETIGO-II.

According to the numerical result, when the current density in the electron beam diode gap exceeds a certain critical value, the beam indicates a unique behavior. Normally, all the electrons emitted from the cathode are accelerated in the cathode layer by the discharge potential difference, move along the electrical field and reach the beam collector to anode. However, when the electron beam current reached the critical value of space-charge limited current, the electron beam becomes unstable. At this point the current of the electron beam from the cathode layer remains practically constant, but the anode current decrease sharply. From Fig. 2 shows that because of the space charge limited current virtual cathode is created near the cathode surface, which is responsible for the low electron beam output current.

Figure 3 shows that the theoretically calculated maximum space charge limited current with the function of gap distance and electron emission radius. The space charge limited current is decreasing so sharply with the increase of gap distance. Those numerical results also show that the space charge limited current for 10 mm gap distance, with the decrease of electron emission radius, the current is also decreased. Fig. 3(b) shows the current for 20 mm gap distance and the phenomena is analogous to the case of 10 mm gap distance. However, the maximum

space charge limited current is decrease considerable for the case of 20 mm gap distance compare to the result of 10 mm gap distance, which is deliberated to be the cause of low beam output current in experiment as well as in numerical calculation also.

#### 4. Conclusions

The numerical simulation was carried out using 2D electrostatic PIC model to investigate the relativistic electron behavior, space charge limited emission of electrons, lower beam output current, and electron emission radius from the cathode surface and partially confirm the experimental results. In comparison with the numerical and theoretical results, the electron emission radius from the cathode surface was expected as around 30 mm. Numerically as well as theoretically, the electron beam output current varied with the change of diode gap distance, which qualitatively satisfies the experimental results. With the increase of diode gap distance, the beam output current decreases in both the numerical and experimental cases. Numerically it is seen that the space charge limited current decreases with the increase of gap distance and oppositely with the decrease of electron emission radius.

The analyses of numerical, theoretical and experimental results explain the physical phenomena of electrons in the diode gap with the varied electric field, and partially satisfies the experimental results with the experimental setup and normalized value of ETIGO-II.

#### References

- [1] Atzeni, Stefano, and Jürgen Meyer-ter-Vehn. *The Physics of Inertial Fusion: BeamPlasma Interaction, Hydrodynamics, Hot Dense Matter: BeamPlasma Interaction, Hydrodynamics, Hot Dense Matter*. Vol. 125. *Clarendon Press*, 2004.
- [2] Pfalzner, Susanne. *An introduction to inertial confinement fusion*. *CRC Press*, 2006.
- [3] Komatsu, Yu, et al. "Changes of implosion dynamics derived by difference of equation of state." *EPJ Web of Conferences*. Vol. 59. *EDP Sciences*, 2013.

- [4] Drake, R. Paul. High-energy-density physics: fundamentals, inertial fusion, and experimental astrophysics. *Springer Science & Business Media*, 2006.
- [5] Amano, Yusuke, et al. "Isochoric heating of foamed metal using pulsed power discharge as a making technique of warm dense matter." *Review of Scientific Instruments* 83.8 (2012): 085107.
- [6] Hayashi, Ryohei, et al. "Numerical analysis of temperature distribution for isochoric heating with intense pulsed power discharge using electron beam diode based impedance controller." *Plasma Sciences (ICOPS) held with 2014 IEEE International Conference on High-Power Particle Beams (BEAMS), 2014 IEEE 41st International Conference on. IEEE*, 2014.
- [7] Hayashi, Ryota, et al. "Impedance control using electron beam diode in intense pulsed-power generator." *Laser and Particle Beams* 33.02 (2015): 163-167.
- [8] Yatsui, K., et al. "Geometric focusing of intense pulsed ion beams from racetrack type magnetically insulated diodes." *Laser and Particle Beams* 3.02 (1985): 119-155.
- [9] Niu, Keishiro. "Nuclear Fusion." *Cambridge University Press*. (1989): chapter-4.
- [10] Devyatkov, V. N., et al. "Generation and propagation of high-current low-energy electron beams." *Laser and Particle Beams* 21.02 (2003): 243-248.
- [11] Tarasenko, V. F., et al. "Supershort electron beam from air filled diode at atmospheric pressure." *Laser and particle beams* 23.04 (2005): 545-551.
- [12] Hockney, Roger W., and James W. Eastwood. Computer simulation using particles. *CRC Press*, 1988.
- [13] Birdsall, Charles K., and A. Bruce Langdon. Plasma physics via computer simulation. *CRC Press*, 2004.
- [14] Blaum, K, and Herfurth, F, Trapped Charged Particles and Fundamental Interactions. *Berlin Heidelberg: Springer*, 2008.
- [15] Jiang, Weihua, et al. "Tight focusing of intense pulsed light-ion beam by spherical "plasma focus diode"." *Japanese journal of applied physics* 32.5B (1993): L752.
- [16] Child, C. D. "Discharge from hot CaO." *Physical Review (Series I)* 32.5 (1911): 492.
- [17] Kikuchi, Takashi, et al. "Intense-heavy-ion-beam transport through an insulator beam guide." *Japanese journal of applied physics* 38.3A (1999): L270.
- [18] Miller, R. An introduction to the physics of intense charged particle beams. *Springer Science & Business Media*, 2012.

# Evaluation of Bipolar Pulse Generator for 2nd stage acceleration in Bipolar Pulse Accelerator

Keito Okajima, Tarou Honoki, Hiroaki Ito

*Department of Electrical and Electronic Engineering,  
University of Toyama, 3190 Gofuku, Toyama 930-8555, Japan*

## ABSTRACT

We have developed a new type of a pulsed ion beam accelerator named “bipolar pulse accelerator (BPA)” for improvement of the purity of the intense pulsed ion beam. The basic BPA system has two magnetically insulated acceleration gaps and is operated with the bipolar pulse. A prototype of the BPA system was developed and we have evaluated the pulsed ion beam accelerated in the 1st stage of the accelerator. The performance of the bipolar pulse generator was evaluated for the experiment on the 2nd stage acceleration of the pulsed ion beam.

## Keywords

Pulsed ion beam, Bipolar pulse accelerator, Gas puff plasma gun, Pulse power technology

## 1. Introduction

The intense pulsed heavy ion beam (PHIB) technology has been developed over the last two decades primarily for nuclear fusion and high energy density physics research [1]. Advances in PHIB technology have led us to a number of potential applications of PHIB to surface modification of materials and a crystallization process of thin films [2-4]. The PHIB technique has also received extensive attention as a new ion implantation technology named “pulsed ion beam implantation” to semiconductor materials for the next generation, since the doping process and the surface annealing process can be completed in the same time.

The PHIB can easily be generated in a conventional pulsed power ion diode using a flashboard ion source. The purity of the PHIB, however, is usually deteriorated by absorbed matter on the anode (flashboard) surface and residual gas molecules in the diode chamber. Thus, the conventional pulsed ion diode is not suitable for the application to the ion implantation. To improve the purity of the intense pulsed ion beam, a new type of pulsed ion beam accelerator named “bipolar pulse accelerator (BPA)” has been proposed and a prototype of the BPA system

has been developed [5-7]. The BPA is an electrostatic two-stage accelerator and has two magnetically insulated acceleration gaps. When the bipolar pulse of -114kV, 70 ns (1st pulse) and 85 kV, 62 ns (2nd pulse) was applied to the drift tube, the ions were successfully accelerated from the grounded anode to the drift tube in the 1st gap by the negative pulse of the bipolar pulse. The pulsed ion beam with current density of 60 A/cm<sup>2</sup> and pulse duration of  $\approx 50$  ns was obtained at 48 mm downstream from the anode surface [8]. In addition, it was found from the evaluation of ion beam energy by a magnetic energy spectrometer that singly and doubly ionized nitrogen ions with 120~130 keV/Z energy were accelerated with proton impurities.

It is important for the 2nd stage acceleration experiment to generate the bipolar pulse with faster rise time and sharper reversing time. The performance of the bipolar pulse generator was evaluated. In this paper, these experimental results are described.

## 2. Basic concept of BPA

Figure 1 shows the concept diagram of the bipolar pulse accelerator. As shown in Fig. 1, proposed ion accelerator consists of a grounded ion source, a drift tube and a grounded cathode and is an electrostatic

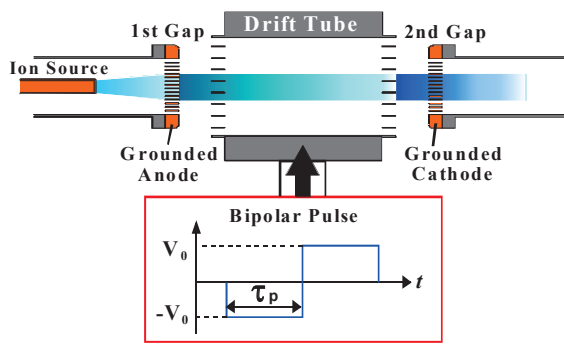


Fig. 1 Conceptual drawing of BPA

two-stage accelerator. In the system, a bipolar pulse of voltage  $\pm V_0$ , duration  $\tau_p$  each is applied to the drift tube. At first the negative voltage pulse of duration  $\tau_p$  is applied to the drift tube and ions on the grounded ion source are accelerated toward the drift tube. If  $\tau_p$  is adjusted to the time of flight delay of the ions to pass the drift tube, the pulse is reversed and the positive voltage of duration  $\tau_p$  is applied to the drift tube when top of the ion beam reaches the 2nd gap. As a result, the ions are again accelerated in the 2nd gap toward the grounded cathode. In the conventional PHIB diode, the ion source is placed on the anode where high voltage pulse is applied, while in the proposed ion diode, the ion source is on the grounded anode, which extremely enhances the accessibility to the anode.

Figure 2 illustrates the principle of the improvement of the purity of the ion beam. Let us now consider the acceleration of ions in the case that the ion beam produced in the ion source consists of  $N^+$  ion and impurity of  $H^+$  ion. In the case, ions of  $N^+$  and  $H^+$  are

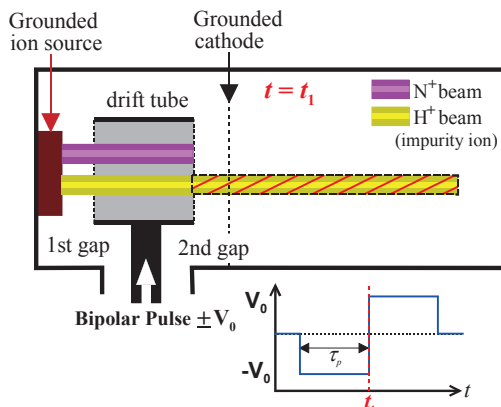


Fig.2 Principle of improvement of the purity of ion beam

accelerated in the 1st gap toward the drift tube when the negative voltage is applied, where  $N^+$  and  $H^+$  ion beams are schematically described in Fig.2.

As seen in Fig.2, the length of  $H^+$  beam is much longer than that of  $N^+$  beam due to the difference of the velocity. We assume that the length of the drift tube is designed to be same as the beam length of  $N^+$  beam with a beam pulse duration  $\tau_p$  at an acceleration voltage  $V_0$ . It is, for example, calculated to be 11.6 cm when  $V_0=200$  kV and  $\tau_p=70$  ns. On the other hand, the length of  $H^+$  beam at  $V_0=200$  kV and  $\tau_p=70$  ns is 43.3 cm. When the voltage is reversed and the positive voltage is applied to the drift tube at  $t = t_1$ ,  $N^+$  beam of length 11.6 cm in the drift tube is accelerated in the 2nd gap. In contrast, 73 % of the  $H^+$  beam is out of the drift tube and decelerated in the 2nd gap by the first pulse. Hence, 73 % of  $H^+$  beam is not accelerated in the 2nd gap by the positive voltage pulse of the bipolar pulse and is removed in the BPA. As a result, the purity of the ion beam is improved.

### 3. Experimental Setup

Figure 3 illustrates the cross-sectional view of the bipolar pulse accelerator in the present experiment, which consists of basically a Marx generator, a PFL, a transmission line and a load (accelerator). The designed output of the bipolar pulse generator is the negative and positive pulses of voltage  $\pm 200$  kV with pulse duration of 70 ns each. In the present system, to generate the bipolar pulse the double coaxial type is employed and has the following features, (i) the length of the line is short, that is, half of the single coaxial type and (ii) the power loss in the switch is reduced, since single switch is used. The PFL consists of three

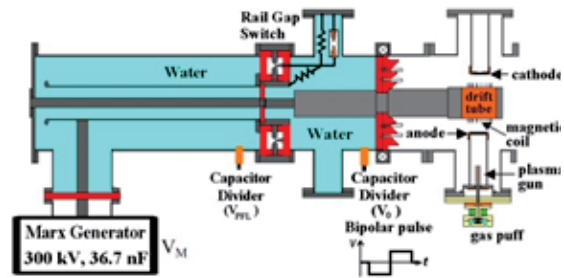


Fig.3 Schematic configuration of bipolar pulse accelerator.

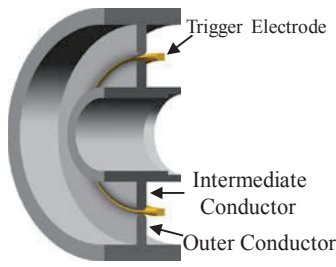


Fig.4 Detail structure of rail gap switch.

coaxial cylinders with a rail gap switch on the end of the line, which is connected between the intermediate and outer conductors and is filled with the deionized water as a dielectric. The characteristic impedance between the inner and intermediate conductors and one between the intermediate and outer conductors are  $6.7 \Omega$  and  $7.6 \Omega$ , respectively. The line is charged positively by the low inductance Marx generator with maximum output voltage of 300 kV and the stored energy of 1.65 kJ through the intermediate conductor.

The waveform of the bipolar pulse is very sensitive to the performance of the rail gap switch, that is, the rise time and the time to reverse the polarity are dependent on the system's inductance including the inductance of the output switch. In order to realize the bipolar pulse with the fast rising and reversing time, the multichannel rail gap switch is utilized as the output switch of low inductance. The detailed structure of the rail gap switch is shown in Fig.4. It consists of essentially a trigger electrode and a pair of main electrodes (an inner and an outer electrode of  $239 \text{ mm}^\phi$  and  $261 \text{ mm}^\phi$ , respectively) separated by a spacing of 11 mm. The main electrodes are made of iron of 20 mm in thickness and have semicircular cross-section of 20 mm in diameter in the end of the electrodes. The knife edged trigger electrode made of copper is placed between the main electrodes and has diameter of 250 mm at top of the edge. These electrodes are carefully aligned and installed in the acrylic vessel. The rail-gap switch is filled with pure  $\text{SF}_6$  gas and the pressure is adjusted to control the optimum trigger timing for each experimental condition.

#### 4. Results and Discussion

In order to evaluate the performance of the bipolar

pulse generator, the  $\text{CuSO}_4$  water solution is used as a dummy load instead of the accelerator. Figure 5 shows the typical waveforms of the charging voltage of the PFL ( $V_{\text{PFL}}$ ) and bipolar pulse output ( $V_{\text{OUT}}$ ) at the charging voltage of 30 kV for the Marx generator. The bipolar pulse voltage ( $V_{\text{OUT}}$ ) and charging voltage of the PFL ( $V_{\text{PFL}}$ ) are measured by the resistive voltage divider and capacitive voltage divider placed near the rail gap switch, respectively. Here the filling pressure of the rail gap switch is 0.26 MPa and the impedance of the dummy load is set at  $Z_L=7.3 \Omega$ , which is almost same as the characteristic impedance of the line between the inner and intermediate conductors. As seen in Fig. 5, the bipolar pulse with voltage of about  $-110 \text{ kV}$  and  $+74 \text{ kV}$  and pulse duration of about 70 ns (FWHM) each is successfully obtained after the charging voltage of the PFL reaches the peak of 240 kV and the rail gap switch is self-broken at  $t \approx 225 \text{ ns}$ . The peak voltage of the first pulse is almost equal to the half of the maximum charging voltage of the PFL. In contrast, the voltage of the second pulse is smaller. The reduction of the voltage in the second pulse seems to be due to the resistance of the rail gap switch.

It turns out from Fig. 5 that the rise time (10-90 % rise time) and reversing time (90-90 % reverse time) of the bipolar pulse are 26 ns and 38 ns, respectively. The performance of the rail gap switch has an influence on the waveform of the bipolar pulse. Especially, the rise time and reversing time is dependent on the switching inductance. The switching inductance can be estimated from the falling time (90-10 % fall time) of the PFL's charging voltage ( $V_{\text{PFL}}$ ). It is found from Fig. 5 that the falling time of  $V_{\text{PFL}}$  is 29

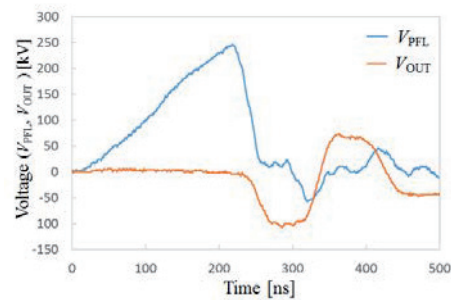


Fig.5 Typical waveforms of the charging voltage of the PFL ( $V_{\text{PFL}}$ ) and bipolar pulse output ( $V_{\text{OUT}}$ ).

ns. Considering that the characteristic impedance of the line between the outer and intermediate conductors is  $6.7 \Omega$ , the switching inductance is estimated to be 62 nH. Figure 6 shows the charging voltage ( $V_{PFL}$ ) of the PFL and the switching inductance as a function of the SF<sub>6</sub> gas pressure in the rail gap switch, where the charging voltage of the Marx generator is 30 kV. The charging voltage increases proportionally with the gas pressure and has the peak at P=0.3 MPa because the switch cannot break down at more than 0.3 MPa. The switching inductance decreases with the increase of the gas pressure and has the minimum value of 62 nH. We need the bipolar pulse with faster rise time and sharper reversing time in order to carry out the 2-stage acceleration experiment. According to Ref.[9], it is reported that the switching inductance of the multichannel rail gap switch can be reduced to less than 10 nH when using the mixture of SF<sub>6</sub> with N<sub>2</sub>. There is a need for making improvements in the performance of the rail gap switch. Thus, there seems to be some room for making improvements in the performance of the rail gap switch such as switch inductance.

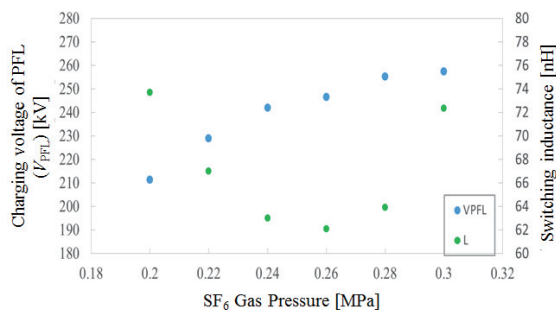


Fig.6 Charging voltage ( $V_{PFL}$ ) of PFL and switching inductance as a function of SF<sub>6</sub> gas pressure.

## 5. Conclusions

The performance of the bipolar pulse generator was evaluated for the experiment on the 2nd stage acceleration of the pulsed ion beam. When the charging voltage of the Marx generator was set to 30 kV, the bipolar pulse with the rise time of 26 ns and reversing time of 38 ns was obtained at the filling SF<sub>6</sub> pressure of the rail gap switch of 0.26 MPa. The switching inductance of the rail gap switch was

evaluated to 62 nH. There is need for making improvements including the performance of the rail gap switch to produce the bipolar pulse with faster rise time and sharper reversing time.

## Acknowledgement

This work was partially supported by JSPS KAKENHI Grant Number JP 15H03961.

## References

- [1] S. Humphries, Jr , "Intense pulsed ion beams for fusion applications", Nucl. Fusion, Vol. 20, pp.1549-1612 (1980).
- [2] D. J. Rej et al., "Materials processing with intense pulsed ion beams", J. Vac. Sci. Technol. A, Vol.15, No.3, pp.1089-1097 (1997).
- [3] H. Akamatsu et al., "Structural Analysis of a High-Speed Tool Steel Irradiated by an Intense Pulsed-Ion Beam", IEEE Trans. Plasma Sci., Vol.30, No.5, pp.1800-1805 (2002).
- [4] J. Khamsuwan et al., "High-energy heavy ion beam annealing effect on ion beam synthesis of silicon carbide", Surface & Coatings Technology, Vol.206, pp.770-774 (2011).
- [5] K. Masugata, "A high current pulsed ion beam accelerator using bi-directional pulses", Nucl. Instrum. & Methods in Phys. Res. A, Vol.411, pp.205-209 (1998).
- [6] K. Masugata et al., "Development of bipolar-pulse accelerator for intense pulsed ion beam acceleration", Nucl. Instrum. & Methods in Phys. Res. A, Vol.535, pp.614-621 (2004).
- [7] H. Ito et al., "Bipolar pulse generator for intense pulsed ion beam accelerator", Rev. Sci. Instrum., Vol.78, 013502 (2007).
- [8] H. Ito et al., "Characteristics of Pulsed Heavy Ion Beam Generated in Bipolar Pulse Accelerator", IEEJ Trans. on Fundamentals and Materials, Vol.135, pp.136-141 (2015).
- [9] K. Masugata et al., "Studies and performance of decreased rail gap switch inductance by enhancing multichanneling via gas mixture", IEEE Trans. on Plasma Science Vol.25, pp.97-99 (1997).